UNIVERSITÀ
DEGLI STUDI
DI PADOVA

Sede Amministrativa: Università degli Studi di Padova

Dipartimento di Architettura, Urbanistica e Rilevamento

SCUOLA DI DOTTORATO DI RICERCA IN: INGEGNERIA INDUSTRIALE
INDIRIZZO: PROGETTAZIONE MECCANICA E INGEGNERIA MOTOCICLISTICA
CICLO XXIII

A VIRTUAL ENVIRONMENT FOR MODELING AND ANALYSIS OF HUMAN EYE

Direttore della Scuola: Ch.mo Prof. Paolo Bariani
Coordinatore d'indirizzo: Ch.mo Prof. Vittore Cossalter
Supervisore: Ch.mo Prof. Gianmaria Concheri
Correlatori: Ing. Roberto Meneghello, Ing. Gianpaolo Savio

Dottorando: Stefano Giovanzana

Abstract

The aim of this work is to develop a virtual environment for modelling and analyse individual virtual eyes which are able to integrate the modern imaging techniques input data. This environment is realized in 3D CAD software by means of specific plug-ins. The tools for analysing the virtual eye are based on ray-tracing and curvature analysis, while the shape of the eye is represented by NURBS or mesh surfaces. This thesis develops, and validates the use of, the plug-ins for the modelization of virtual eyes inside a 3D CAD environment; in particular a novel lens model whose shape is linked to geometrical and optical constraints was created. Shape was also tested on real crystalline images obtained with shadow photogrammetry. Moreover real eye topography was used for modelization of anterior cornea and preliminary results from ray tracing are shown. This model and the ray-tracing tools may be used in future works for design of ophthalmic, contact or intraocular lenses, specifically customised of a single ametropy.

Keywords: geometric modeling, curvature analysis, ray tracing, eye model, human lens, refraction errror

Lo scopo di questo lavoro è stato quello di sviluappare un ambiente virtuale per la modellazione e l'analisi di un occhio virtuale personalizzato, che fosse in grado di integrare le moderne tecniche di analisi ottica come dati di ingresso. Questo ambiente è stato sviluppato all'interno di un software CAD tramite l'ultilizzo di plug-in specifici. Gli strumenti utilizzati per analizzare l'occhio virtuale sono basati sul ray-tracing e sull'analisi di curvatura, mentre la geometria dell'occhio è stata modellizzata tramite l'utilizzo di superfici NURBS o mesh. La presente tesi sviluppa, e valida l'utilizzo, di codesti plug-in per la modellizzazione di un occhio virtuale in un ambiente CAD 3D; in particolare è stato creato un modello innovativo di lente, la cui forma è legata a vincoli geometrici ed ottici. La forma di tale lente è stata confrontata con cristallini reali le cui immagini sono state ottenute tramite fotografia ad ombra. Inoltre la topografia di un occho reale è state utilizzata per modellare la superficie anteriore della cornea e sono quindi riportati i risultati preliminari del ray-tracing. Questo modello e gli strumenti di ray-tracing utilizzati potranno essere utilizzati in futuro per la progettazione di lenti oftalmiche, a contatto o intraoculari specificatamente costumizzate sulle esigenze dell'ametrope.

Parole chiave: modellazione geometrica, analisi di curvature, ray tracing, modelli di occhio, modelli di lente, errori di rifrazione

Acknowledgements

I would like to thank all those who help me make this dissertation possible. I would like to thank my supervisors, Prof. G. Concheri,R. Meneghello, Ph.D. and G. Savio, Ph.D.

I would like to thank R. Urs, Ph.D., and Prof. F. Manns, Dr. A. Ho, Dr. J. Parel, of the the Ophthalmic Biophysics Center, Bascom Palmer Eye Institute, University of Miami Miller School of Medicine, Miami, USA, for the lens photogrammetry image that they provide to our group. They play a fundamental role for the development of the lens model.

I would like to thank G. Guerra of Naturalens s.a.s., Padova, Italy for the topography data provided.

I am grateful to Prof. D.A. Atchison, Prof. B.K. Pierscionek, and E. Hermans, Ph.D., for the inspiring e-mail responses that helped me so much.

Contents

List of figures

List of tables

Chapter 1. Aims

As a result of Gullstrand's work of 1909, many eye models have been developed. These models are based upon average measures from a large number of subjects. Both the geometry of the surface and the optics of the elements that compose schematic eyes have been improved to better fit real eyes.

The geometry of these first eye models used only circular curves; more complex models have been developed with the introduction of aspherical or parametric curves. Regarding the optics of the elements, and in particular of the crystalline lens, from a homogeneous index of refraction, gradient index models have been developed to better achieve the performance of real lenses

On the other hand techniques used to measure the different surfaces of the eye have been improved with the introduction of computer aided imaging. Modern topographers are able to create images of the anterior cornea surface and provide as output a collection of points that map the surface itself, other imaging tools also provide high quality digitalised photographs.

This imaging data normally uses simple aspheric curves for fitting and so only average data is used for the modeling of schematic eyes.

In the last few years there has been a growing interest in geometric modelling of a free form based virtual eye, which can be used to simulate the behaviour of a real eye.

The aim of this work is to develop a virtual environment for modelling and analyse individual virtual eyes which are able to integrate the modern imaging techniques input data. This environment is realized in 3D CAD software by means of specific plug-ins.

The tools for analysing the virtual eye are based on ray-tracing and curvature analysis, while the shape of the eye is represented by NURBS or mesh.

This work is part of the DAUR-Lin group project "Identification of strategies for geometric modelling of free form complex surfaces of ophthalmic lenses for refractive defects correction, by tools and methods integration based on analysis of wavefront aberration; curvature calculating and ray-tracing". The topics developed in this thesis are geometric modelling, shape and optical analysis of a virtual eye based on real eye data.

In the future 3D modelling could be really important in ophthalmology and optometry. Modern imaging tools such as; shadow photogrammetry, OCT, MRI, and Sheimpflug lamps, can be interfaced with a CAD environment to model virtual eyes closer to real eye shape. CAD may also become a useful instrument in analysing ametropy and designing customised ophthalmic or contact lenses, and with the well known CAD-CAM system also the production of medical devices may be improved.

This thesis develops and validates the use of plug-ins for the modelization of virtual eyes inside a 3D CAD environment; in particular a novel lens model whose shape was linked to geometrical and optical constraints was created. Shape was also tested on real crystalline images obtained with shadow photogrammetry.

Moreover real eye topography was used for modelization of anterior cornea and preliminary results from ray tracing are shown.

This model and the ray-tracing tools may be used in future works for design of ophthalmic, contact or intraocular lenses, specifically customised of a single ametropy.

The thesis is structured as following: chapter 2 introduces the state of art about surface analysis in particular techniques to evaluate the curvature; geometrical optics of curves in the plane; physiology of the human eye; and it will introduce the schematic eyes developed in the last century.

In chapter 3 the tools developed for curvature analysis of freeform curve and surfaces defined as continuous function or discrete model and optical analysis into the CAD environment are described in details.

In chapter 4 it is proposed a lens model based on geometrical and optical constraints. It is developed; analysed using the tools described in chapter 3 and compares the results against five models well known in the literature. The proposed lens model is also applied to a real lens models which contour was taken by shadow photogrammetry image technique.

In chapter 5 the shape modeling of a schematic eye into a 3D CAD environment is proposed. Moreover the tools developed in chapter 3 together the lens model proposed in chapter 4 are adopted in the shape and optical analysis of an eye. Also the anterior cornea surface is replaced with real eye topographer data.

Chapter 2. Background

This chapter describes the state of art of the three main topics of this thesis. In the first section curvature analysis formulae and different types of curvature estimation methods for discrete surface in a 3D space are shown. In the second section are given the basis of geomtetric optics for aspheric surfaces and an example of a thick lens ray tracing in the plane is given. At the end is shown the optical structure of the human eye and the common models used as schematic eyes.

2.1. Curvature analysis

Curvature assessment is the basis for the evaluation of functional properties of complex optical surfaces, as e.g. in progressive ophthalmic lenses. Many methods have been developed to directly calculate or estimate the curvature of 2D curves or 3D surfaces.

In this part we would like to give an overview of the state of art for curvature calculation for curves and surfaces described by analytic functions (Mortenson, 2006). In the following chapter we present the tools developed by DAUR-LIN group for the estimation of curvature of curves and surfaces which profile is defined by discrete points acquired by contact methods, e.g. profilometry.

2.1.1. Curve curvature

Let ds be an infinitesimal piece of curve from point A to point B (figure A1). And let the first derivative of the curve in the point A be $f'(x_A) = \tan(\alpha)$ and in the point B $f'(x_B) = \tan(\alpha+d\alpha)$ be the first derivative of the curve in point A and B.

We will call (tangential) curvature k the ratio:

$$k = \frac{1}{r} = \frac{d\alpha}{ds} \qquad (2.1)$$

where R is the radius of curvature and it is equal to the inverse of the curvature k.

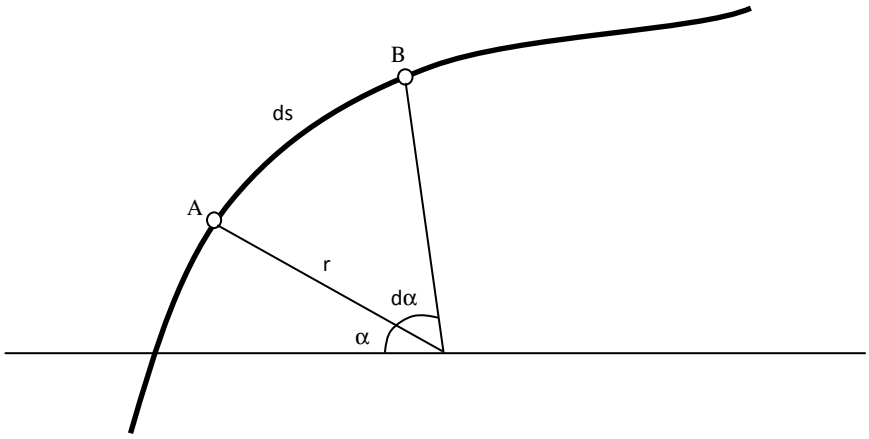

Figure 2.1 Curvature Radius of a 2D curve

Let dy/dx = tan(α) and differentiate this equality we obtain:

$$\frac{d^2ydx - dyd^2x}{dx^2} = \frac{1}{\cos^2\alpha}d\alpha \qquad (2.2)$$

but ds/dx = 1/cos(α), so substituting this equalities and dividing for ds^3:

$$\frac{d^2ydx - dyd^2x}{ds^3} = \frac{d\alpha}{ds} = \frac{1}{r} \qquad (2.3)$$

From Pitagora's theorem we know that ds = $\sqrt{dx^2 + dy^2}$ so that ds/dx = $\sqrt{1 + y'^2}$ and we finally obtain the (tangential) curvature for a curve in a 2D plane, or the tangential radius of curvature:

$$r = \frac{1}{k} = \frac{\left(1 + \left(\frac{dy}{dx}\right)^2\right)^{3/2}}{\frac{d^2y}{dx^2}} \qquad (2.4)$$

where the first and second derivative of the function respect to x denoted in the text may become also as $\partial y/\partial x$ and $\partial^2 y/\partial x^2$ if we consider partial derivative as it will be seen in the following part of the thesis.

If the curve is defined in a parametric form, which is a method widely use especially in computer aided graphic and design:

$$x = x(u) \qquad y = y(u) \qquad (2.5)$$

where u is a parameter that usually goes from 0 to 1 for Cartesian curves, or from 0 to π for polar curves; following the same passages as above the curvature may be found as:

$$k = \frac{1}{r} = \frac{x_u y_{uu} - x_{uu} y_u}{\left((x_u)^2 + (y_u)^2\right)^{3/2}} \qquad (2.6)$$

where x_u and x_{uu} stands for the first and second derivative of x respect to u; similarly for y_u and y_{uu}.

2.1.2. Surface curvature and principal directions

Let S(u,v) be a parametric twice differentiable surface in a R^3 space, and let S_u and S_v the partial derivates of S on u and v. The normal vector ⊥ is given by:

$$\perp(u,v) = \frac{S_u \times S_v}{|S_u \times S_v|}. \qquad (2.7)$$

The curvature parameters for a parametric surface are usually derived by the fundamental forms given by the following matrix (Stoker, 1969):

- first fundamental form

$$I = \begin{bmatrix} S_u \cdot S_u & S_u \cdot S_v \\ S_v \cdot S_u & S_v \cdot S_v \end{bmatrix} = \begin{bmatrix} E & F \\ F & G \end{bmatrix}; \qquad (2.8)$$

- second fundamental form

$$II = \begin{bmatrix} S_{uu} \cdot \perp & S_{uv} \cdot \perp \\ S_{vu} \cdot \perp & S_{vv} \cdot \perp \end{bmatrix} = \begin{bmatrix} L & M \\ M & N \end{bmatrix}. \qquad (2.9)$$

The principal curvatures k_1 and k_2 are the roots of the following equation (Mortenson, 2006):

$$(EG - F^2)\cdot k^2 - (EN + GL - 2FM)\cdot k + (LN - M^2) = 0, \qquad (2.10)$$

while the Gaussian k_G and the mean k_M curvature are given by

$$k_G = k_1 \cdot k_2 = \frac{LN - M^2}{EG - F^2} \quad (2.11)$$

$$k_M = \frac{k_1 + k_2}{2} = \frac{EN - GL - 2FM}{2\left(EG - F^2\right)}. \quad (2.12)$$

Beside principal curvatures k_1 and k_2, also their directions can be derived, finding the roots of the following equation:

$$(FN - GM)\cdot\tau^2 + (EN - GL)\cdot\tau + EM - FL = 0 \quad (2.13)$$

where τ=dv/du are the principal directions. Them can be also derived by computing the arctangent of the dv/du ratio and noted as $\varphi 1$ and φ_2.

Analogously the Gaussian k_G and mean k_M curvature can be derived by the fundamental forms (Goldman, 2005):

$$k_G = \frac{Det(II)}{Det(I)} = \frac{(S_u \times S_v)\cdot(\perp_u \times \perp_v)}{|S_u \times S_v|^2} \quad (2.14)$$

$$k_M = \frac{Tr(I \cdot II^*)}{2Det(I)} = \frac{(S_u \times S_v)\cdot((S_v \times \perp_u) - (S_u \times \perp_v))}{2|S_u \times S_v|^2} \quad (2.15)$$

where II* denotes the adjoint of II. In this case, from k_G and k_M the principal curvatures can be derived by:

$$k_1, k_2 = k_M \pm \sqrt{k_M^2 - k_G}. \quad (2.16)$$

The parameter k_D, indicating the difference between the principal curvatures, can be introduced:

$$k_D = k_1 - k_2 = 2\sqrt{k_M^2 - k_G}. \quad (2.17)$$

2.1.3. Surface curvature estimation methods

In the previous paragraph are described methods to find curvature of curves and surfaces once they are defined by analytical functions y = f(x) for curves and S = S(x,y) for surfaces or their parametric forms.

Not always is possible to define a curve or a surface in an analytic form, but sometimes they may be defined point by point. On the other hand when a surface is acquired by optical techniques, e.g. laser scanner, or contact techniques, e.g. profilometry, many programs give as an output a cloud of points, which is of course a collection of points in the plane or in the space.

In the literature many works described methods to estimate curvature parameters of discrete surfaces. These methods can be classified into three categories: (a) fitting methods, (b) discrete estimation of curvature and (c) tensor methods. (Gatzke and Grimm, 2006)

2.1.3.1. Fitting methods

Fitting methods compute the curvature of a substitute surface used to fit locally the discrete points set. A discriminator between fitting methods is the function chosen for the approximation of local surface. Usually a local coordinate frame is used to simplify parameterization and may also simplify the estimation. The function fits vertices using a least-squares minimization method, and the coefficients of the function are calculated. At that stage the main problem is linked to distortions induced by the local parameterization itself and the projection onto the normal plane of the given vertex; several algorithms have been developed to preserve relationships and avoid folding (Floater, 1997; Sheffer, 2002; Desbrun et al., 2002). Through the function's coefficients, curvatures and their principal directions are directly calculated. The most used functions are quadratic forms and their variations (Stokely, 1992; Hamman, 1993; Krsek et al., 1998; Douros,

2002). These forms are deeply analysed to find the best local approximation. In McIvor et al. (1997) the problems of quadratic fitting of surfaces with large curvature magnitude or for approximation of spherical and cylindrical patches are shown.

A variation of the quadratic method is proposed by Gatzke and Grimm (2003). They substitute the projection on the tangent plane with a parameterization using a flattering algorithm of Desbrun et al. (2002) e Sheffer (2001). On the other hand Goldfeather et al. (2004) substitute the entire quadratic function with a cubic fit of a system of equations formed by the coordinates and normal vectors at vertices on the one-ring neighbourhood. Other methods use spline (Naik, 1998) or biquadratic Bézier patches (Razdan, 2005) for local approximation.

2.1.3.2. Discrete methods

To avoid the computational costs associated with fitting algorithms, many discrete methods that significantly increase the computational efficiency have been introduced. However a great limitation of these methods is that they provide only a subset of Gaussian, mean and principal curvature directions. Some authors (Krsek et al., 1998; Meek, 2000; Kim et al., 2001) describe algorithms based on Gauss-Bonnet theorem (Struik, 1961; Do Carmo, 1976), also known as angle deficit method. This method provides an elegant and compact method for calculating Gaussian and mean curvatures based on turning the angles of the first-ring neighbours. Meek (2000) give a quantitative error analysis for that kind of method; Dyn et al. (2001) apply this method to calculate the mean curvature integral over the edge path. Another method involving angles is the angle exceed method (Stokely, 1992) used also for computing minimum surfaces and geodesic (Polthier, 2006). In other works the curvature estimation is based on circular fits on a vertex and its neighbours (Chen, 1992; Martin, 1998). Then, using the Euler-Mesnier theorem (Struik, 1961; Do Carmo, 1976) the curvature itself is calculated. Focused on meshes decimation is the Watanabe method (Watanabe, 2001), quantitatively used and compared by Magid et al. (2007).

2.1.3.3. Tensor method

In curvature tensor estimation, instead of estimating the curvature directly, it is calculated through the computation of the curvature tensor. This method has a computational complexity lower then the fitting methods, but higher than discrete methods. The most common estimating curvature tensor method is the one proposed by Taubin (1995), then extended by Hameiri (2003) expanding the original method to first-neighbour vertices and changing weight from triangle areas to distance between vertices. Surazhsky et al. (2003) proposed other weight coefficients based on angles. Beside these modifications of the original Taubin's method other algorithms have been developed to make the tensor method less sensitive to noise. A robust method is proposed by Tang (2002) further on developed by Tong (2005) and Page et al. (2002). The last method is also able to detect crease values over large meshes.

2.1.3.4. Method comparison

Other relevant works compared different methods to calculate curvature. Gatzke and Grimm (2006) analyse curvature estimation methods' sensitivity to noise, mesh resolution and mesh regularity showing the dependence form valence, triangles' shape and curvature's sign. Magid et al. (2007) analyse four different algorithms and test them on triangular meshes that represent tessellation of synthetic geometric models. The result is compared with the analytically computed values of curvatures for the non-uniform rational B-spline (NURBs) surfaces from which these meshes originated. They also apply these methods to a real object scanned image.

2.2. Geometrical Optics

The description of geometrical optics is provided according to Jalie (2003), and Atcison and Smith (2000).

In geometrical optics, the light propagation is described in terms of rays. These rays are assumed to travel in straight lines as long as the refractive index of a medium is homogeneous. In this part we will not use multiple rays to calculate the refraction as used in the finite ray-trace but we use Coddington's equations to calculate the image distances.

This method allows us to fast calculate sagittal and tangential optical properties of simple lenses, starting from one single refraction surface and arrive to a thick aspherical optical system in two dimensions.

2.2.1. Single surface refraction

For the refraction by a thick dioptre with a spherical surface Snell's law is:

$$n \cdot \sin i = n' \cdot \sin i' \qquad (2.18)$$

in paraxial approximation it becomes:

$$n \cdot \sin i = n' \cdot \sin i' \qquad (2.19)$$

where n is the index of refraction of the media and i is the angle between the ray and the normal of the surface, symbols without apex are referred to object space and the symbols with apex are referred to image space refracting surface.

The height of incidence y_e (figure 1) of the ray on the surface in object space is:

$$y_e = l \cdot \sin\gamma \qquad (2.20)$$

where l is the distance between the object and the incidence point of the principal ray on the surface, and γ is the angle between the ray and the optical axis.

We want to remark that quantities that lie on the left of the surfaces are taken with a minus sign and quantities that lie on the right of the surface are taken positive. Angles that round anti-clockwise are positive angles, on the other hand angles that round clockwise are negative angles.

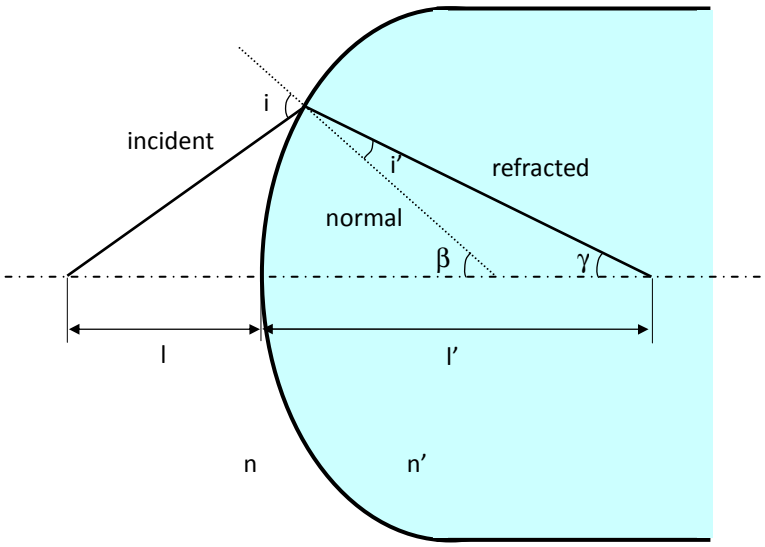

Figure 2.2 Thick dioptre with incident and refracted ray

Referring to the normal of the surface we can instead write:

$$y_e = r \cdot \sin\beta \qquad (2.21)$$

where r is the radius of the spherical surface and β is the angle between the normal at the incident point and the optical axis. In paraxial approximation the previous formulas become:

$$y_e = l \cdot \gamma = l' \cdot \gamma' = r \cdot \beta \qquad (2.22)$$

According to figure 1 we can then write the trigonometric equalities:

$$i = \gamma - \beta \qquad (2.23)$$

$$i' = \gamma' - \beta \qquad (2.24)$$

and then we can rewrite the Snell's law in paraxial approximation as the well know Gauss single surface refraction formula:

$$\frac{n'}{l'} - \frac{n}{l} = \frac{n'-n}{r}. \qquad (2.25)$$

If we now consider

$$L' = \frac{n'}{l'} \quad \text{and} \quad F = \frac{n'-n}{r} \qquad (2.26)$$

the previous equation can also be written as:

$$L' = L + F \qquad (2.27)$$

known as the fundamental equation of optics, where L' is the vergence in the image space, L is the vergence in object space and F is the power of the surface, all the quantities are in dioptres D [m^{-1}].

2.2.2. Coddington's equations

If we consider an off-axis object to be refracted by a spherical surface we have to take into account the oblique astigmatism aberration. The effect of this aberration is to cause the pencil of light to pass through two focal lines at right angles to one another, that is, the pencil becomes astigmatic.

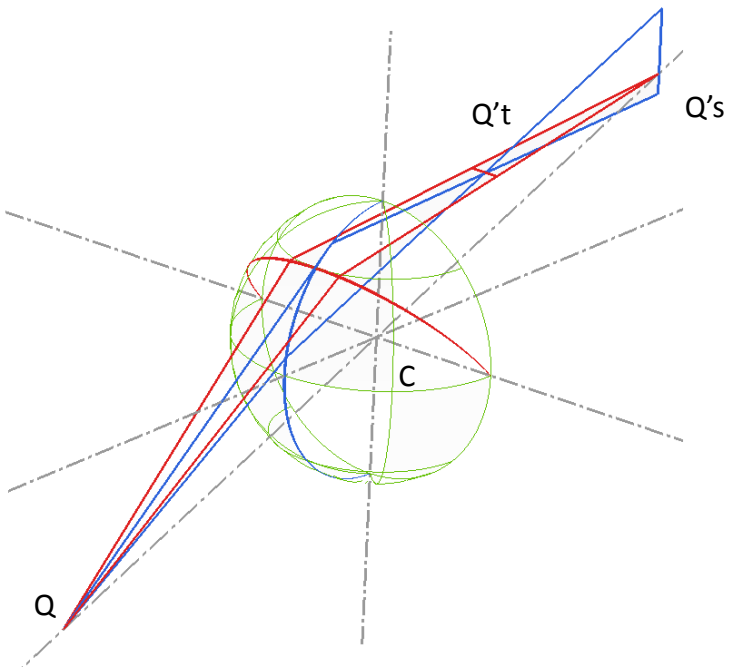

Figure 2.3 Oblique astigmatism

The aberration for a single spherical surface is illustrated in Figure 2.3. A is the intersection point between the principal oblique ray line of the pencil of light and the spherical surface whose centre of curvature lies at C. The vertical meridian of the refracting surface is represented by the trace T and the horizontal meridian of the surface is represented by the trace S.

The plane of the paper (which contains T) is the tangential plane. The plane at right angles to the paper plane (in which S lies) is the sagittal plane. Both the axis AC and the auxiliary axis through Q, QC, lie in the tangential plane.

A narrow pencil of light (which is exaggerated in the figure) incident upon the surface in the tangential plane is refracted to form a tangential image of Q, the image being labelled Q't in the figure. A narrow pencil of light incident upon the surface in the sagittal plane is retracted to form a sagittal image Q's. It will be noted that Q't lies in the sagittal plane whereas Q's lies in the tangential plane.

Approximately midway between the two line foci the pencil has its least cross-section, named point of least confusion. The distance between Q't and Q's expressed in dioptres is called oblique astigmatic error.

2.2.2.1. Position of the sagittal focus

Figure 2.4 represents a single refracting surface of radius r separating a medium on the left whose refractive index is n, from a medium on the right whose refractive index is n' (n' > n).

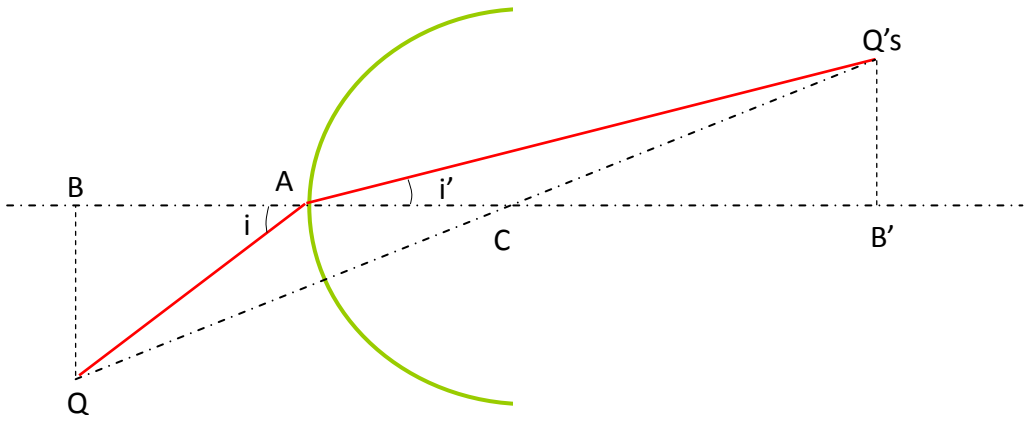

Figure 2.4 Sagittal focus

We are given the position of the extra-axial object point Q by its distance, QA = s, and the angle i, which the ray QA makes with the normal of surface. We wish to find the distance AQ's = s', of the conjugate sagittal image point.

From the similar triangles QBC and Q'sB'C we have:

$$\frac{Q'sB'}{QB}=\frac{CB'}{CB}=\frac{AB'-r}{AB-r}=\frac{s'\cdot\cos i'-r}{s\cdot\cos i-r}. \qquad (2.28)$$

From triangles QBA and Q'sB'A and Snell's law we can write:

$$\frac{Q'sB'}{QB}=\frac{s'\cdot\sin i'}{s\cdot\sin i}=\frac{ns'}{n's}. \qquad (2.29)$$

Equating the previous formulas we obtain

$$\frac{n'}{s'}-\frac{n}{s}=\frac{n'\cdot\cos i'-n\cdot\cos i}{r} \qquad (2.30)$$

that is the Coddington's equation formula for the sagittal image point Q's. We can notice the similarity of this expression with the paraxial equation.

2.2.2.2. Position of the tangential focus

Figure 2.5 represents the refraction of two close tangential rays at a curved surface. QB is the principal oblique ray of the fan. The point T represents a virtual object point and given QT = t we wish to find the position of the conjugate tangential image point QT' = t'.

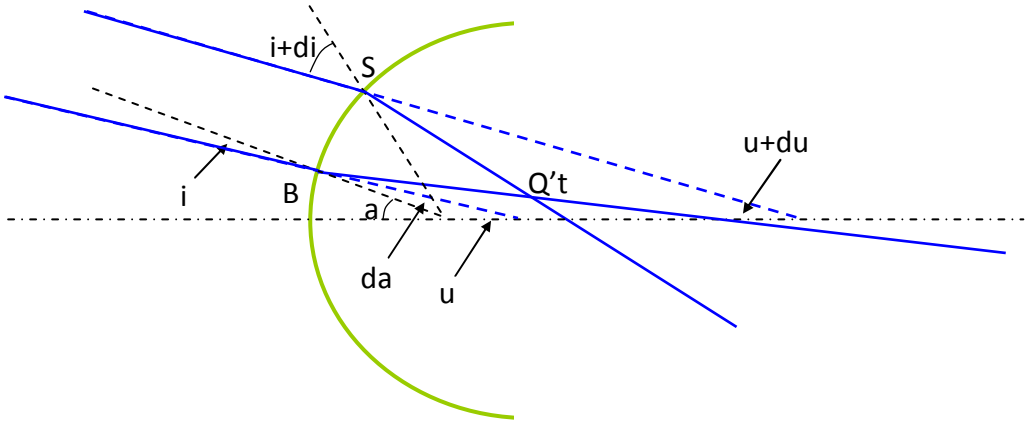

Figure 2.5 Tangential focus

The principal oblique ray, QB, is incident upon the surface at the angle i and after refraction makes the angle i' with the normal of the surface. The angles formed by this ray with the axis of symmetry of the surface are u before refraction and u' after the refraction.

The outer ray of the fan passing through S, is incident upon the surface at a slightly greater angle of incidence which we will call i + di. The angle of refraction is then i' + di'.

Referring to triangles QBC and QB'C we find a = i + u = i' + u' and referring to the outer ray we find

$$a + da = (i + di) + (u + du) = (i' + di') + (u' + du') \qquad (2.31)$$

subtracting the first equations from the second we have

$$di = da - du \quad \text{and} \quad di' = da - du' \qquad (2.32)$$

from which we can write

$$\frac{di}{di'} = \frac{da - du}{da - du'}. \qquad (2.33)$$

Dropping a perpendicular from Q to P (i.e. PQB= 90°) we can see that PQS = i and if we assume that the fan is so narrow that the arc QS is indistinguishable from a straight line, we find that $PQ = QS \cdot \cos i$. Dropping a perpendicular from S to R we find in the same way that RSQ = i' and $RS = QS \cdot \cos i'$. Referring to triangles SQC; PQT and SRT' and remembering the assumption that the angles are little so that the tangent can be substituted by the angles themselves we can find:

$$da = \frac{Qs}{r} \qquad du = \frac{PQ}{t} \qquad du' = \frac{RS}{t'}. \qquad (2.34)$$

Substituting the values for PQ and RS we have:

$$du = \frac{QS \cdot \cos i}{t'} \quad \text{and} \quad du' = \frac{QS \cdot \cos i'}{t'} \qquad (2.35)$$

and we can substitute in the above equation

$$\frac{di}{di'} = \frac{\frac{1}{r} - \frac{\cos i}{t}}{\frac{1}{r} - \frac{\cos i'}{t'}}. \qquad (2.36)$$

On differentiating Snell's ration we obtain:

$$\frac{di}{di'} = \frac{n' \cdot \cos i'}{n \cdot \cos i} \tag{2.37}$$

and equating the last two relationships we finally obtain:

$$\frac{n' \cdot \cos^2 i'}{t'} - \frac{n \cdot \cos^2 i}{t} = \frac{n' \cdot \cos i' - n \cdot \cos i}{r} \tag{2.38}$$

that is the Coddington's equation formula for the tangential image point Q't. We can notice the similarity of this expression with the paraxial equation, in particular the quantity:

$$\frac{n' \cdot \cos i' - n \cdot \cos i}{r} \tag{2.39}$$

appears in the right hand side of both the tangential and the sagittal Coddington's equations and is sometimes referred to as the astigmatic constant of the surface.

2.2.3. Aspherical surfaces

In the meridian section, a conicoid aspheric surface can be described by the explicit equation:

$$y = \pm\sqrt{2rz - (1+q)z^2} \tag{2.40}$$

or can also be defined as:

$$z = \frac{r - \sqrt{r^2 - (1+q)y^2}}{1+q} \tag{2.41}$$

where r is the vertex radius of the surface and q is the asphericity of the conicoid:

- if $q < -1$ the conicoid represent a hyperboloid,
- if $q = -1$ it represent a paraboloid,
- if $-1 < q < 0$ it represent an oblate ellipse,
- if $q = 0$ it represent a circle,
- if $q > 0$ it represent a prolate ellipse.

The above expression can be transform in a more robust form as:

$$z = \frac{y^2}{r + \sqrt{r^2 - (1+q)y^2}} \tag{2.42}$$

this expression instead the previous one is valid for every value of q and r. This equation of the conicoid surface can be expanded into Taylor's series:

$$z = \frac{y^2}{2 \cdot r^2} + \frac{(1+q) \cdot y^4}{8 \cdot r^3} + \frac{(1+q)^2 \cdot y^6}{16 \cdot r^5} + \ldots \tag{2.43}$$

The radial (tangential) radius r_t for a rotational surface is (Durell and Robson, 1968) (see Appendix B for more details):

$$r_t = \frac{\left[1 + \left(\frac{\partial z}{\partial y}\right)^2\right]^{3/2}}{\frac{\partial^2 z}{\partial y^2}} \tag{2.44}$$

where the first derivate of the conicoid surface is:

$$\frac{\partial z}{\partial y} = \frac{y}{\sqrt{r^2 - (1+q)y^2}} \tag{2.45}$$

and the second derivate is:

$$\frac{\partial^2 z}{\partial y^2} = \frac{r^2}{\left[r^2 - (1+q)y^2\right]^{3/2}} \qquad (2.46)$$

from which it can be shown that:

$$r_t = \frac{\left[r^2 - q \cdot y^2\right]^{3/2}}{r^2}. \qquad (2.47)$$

Now, from Martin (1961), $r_s = \left(r_t \cdot r^2\right)^{1/3}$ so that we can find the sagittal vertex radius r_s:

$$r_s = \sqrt{r^2 - q \cdot y^2}\ . \qquad (2.48)$$

For aspherical surfaces we can then write the Coddington's equations in that form:

$$\frac{n'}{s'} - \frac{n}{s} = \frac{n' \cdot \cos i' - n \cdot \cos i}{r_s} \qquad (2.49)$$

$$\frac{n' \cdot \cos^2 i'}{t'} - \frac{n \cdot \cos^2 i}{t} = \frac{n' \cdot \cos i' - n \cdot \cos i}{r_t} \qquad (2.50)$$

2.2.4. Third-order theory

Before apply the Coddington's equations to find the oblique astigmatism of a single thin aspherical lens in air and show strategies to minimize it, we have to consider approximate equations of the sagittal and tangential radii and of the angles included in the previous equations.

This is the well known third-order theory, used by Jalie (1977) for sine formulae and by Whitwell (1921) to derive the cosine formulae of intercept and refraction angles for spherical surfaces and subsequently expanded by Atchison (1984) for aspherical surfaces.

We show immediately the third-order approximation of Taylor series for sagittal and tangential vertex radii founded by previous formulae:

$$r_s = \frac{1}{k_s} = r - \frac{q \cdot y^2}{2 \cdot r} \quad \text{and} \quad r_t = \frac{1}{k_t} = r - \frac{3 \cdot q \cdot y^2}{2 \cdot r} \qquad (2.51)$$

where k = 1 / r is the curvature of the surface.

About the angle approximation we will use again third-order approximation since we will limit the following treatment to angles which are less then 15°. The Taylor's expansions till the third-order for incidence (and refraction) angle expressed in radians are then:

$$\cos i = \sqrt{1 - \sin^2 i} = 1 - \frac{1}{2} i^2 \qquad (2.52)$$

$$\cos^2 i = 1 - \sin^2 i = 1 - i^2 \qquad (2.53)$$

$$\frac{1}{\cos^2 i} = 1 + \tan^2 i = 1 + i^2 \qquad (2.54)$$

Referring to figure 2.6 we can substitute the angle between the incidence ray and the optical axis γ with intercept height y by geometrical equalities:

$$y = l \cdot \tan\gamma \qquad (2.55)$$

and since we consider that the angles are small we can write:

$$\gamma = \frac{y}{l}. \qquad (2.56)$$

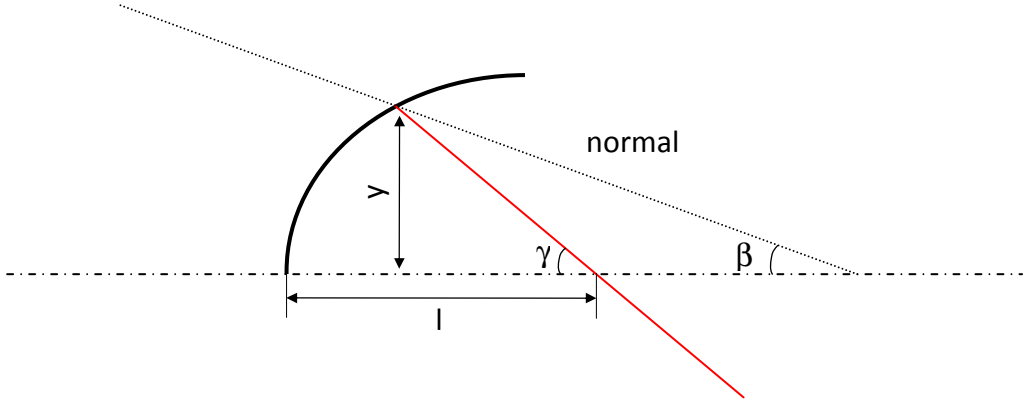

Figure 2.6 Calculation of angle between normal and optical axis for an aspheric surface

As for the previous angle we can write a similar expansion for the angle between the normal of the surface at the interception point and the optical axis in the tangential plane, previously named β in figure 2.1. If we consider an aspherical surface we have to find a relationship between the angle β and the intersection height y.

In the tangential plane we can write:

$$y = r_s \cdot \sin\beta \qquad (2.57)$$

since the first derivative of the surface can be expressed as:

$$\frac{\partial y}{\partial z} = \frac{\sqrt{r_s^{\,2} - y^2}}{y} \qquad (2.58)$$

we can define the sagittal radius r_s , apart from the sign, as:

$$r_s = y \cdot \sqrt{1 + \left(\frac{\partial y}{\partial z}\right)^2} \qquad (2.59)$$

substituting that equation in the previous one we find that:

$$\sin\beta = \frac{1}{\sqrt{1 + \left(\frac{\partial y}{\partial z}\right)^2}}. \qquad (2.60)$$

As it can be seen, this expression doesn't take count of the sign of the angle β between the normal of the surface and the optical axis; in particular if the chief ray intercepts the surface behind the optical axis, negative y-direction, the angle β should be negative.

To take into account the sign of the angle, and remembering that in previous section we have calculated δz / δy, and we are considering continuous surfaces, we can write:

$$\sin\beta = \frac{\frac{\partial z}{\partial y}}{\sqrt{1 + \left(\frac{\partial z}{\partial y}\right)^2}}. \qquad (2.61)$$

Substituting the previous expression of the first derivative we find:

$$\sin\beta = \frac{y}{\sqrt{r^2 - q \cdot y^2}} \tag{2.62}$$

where the height y is taken with it signs.

If we now would like to find the cosine of angle β after simple substitution we find:

$$\cos\beta = \frac{\sqrt{1-(1+q)\cdot\left(\frac{y}{r}\right)^2}}{\sqrt{1-q\cdot\left(\frac{y}{r}\right)^2}} \tag{2.63}$$

that is the analogous of the formula by Atchison (1984).

Applying now the third-order approximation to angle β we simply find what we are searching for:

$$\beta = \frac{y}{r} \tag{2.64}$$

where we can see show that the angle β between the normal of the surface and the optical axis does not depends neither by the asphericity q neither by sagittal or tangential radius.

In third-order theory so that the angles are considered small we can neglect the asphericity of the surface and consider only its vertex radius.

Finally we want to approximate the angle between the incidence ray and the normal i, referring to figure 2.5 we can find from geometrically:

$$i = \beta - \gamma = \frac{y}{r} - \frac{y}{l} \tag{2.65}$$

and substituting:

$$F = \frac{n'-n}{r} \quad \text{and} \quad L = L'-F = \frac{1}{l} \tag{2.66}$$

where F is the power of the single surface, and L is the vergence incoming to the surface and L' is the vergence outgoing from the surface, we obtain then:

$$i = y\left[\frac{F(n'-n+1)-L'(n'-n)}{n'-n}\right]. \tag{2.67}$$

We have now all the approximation needed into Coddington's equation; all the quantities are expressed in term of optical quantities, such as power or vergence, or geometrical quantities, such as interception height.

2.2.5. Thin lens in air with aspherical surfaces

We want now to calculate the outgoing vergence in sagittal and tangential plane for a thin aspherical lens in air. The refractive index of the material of the lens is n > 1 and the surrounding material is considered in the following section air so that $n_{air} = 1$. Due to lens fabrication matter we want to express these quantities in terms of total power of the lens F, power of the second surface F_2, and incidence height to the lens surface y.

Before applying the previous third-order approximation formulae we have to rewrite them for this specific case. In particular we want to express incidence angle a to the first surface and the refracted angle d from the second surface in term of total power F and of the power of the second surface F2. The other two angle will be found applying Snell's law a = nb and d = nc.

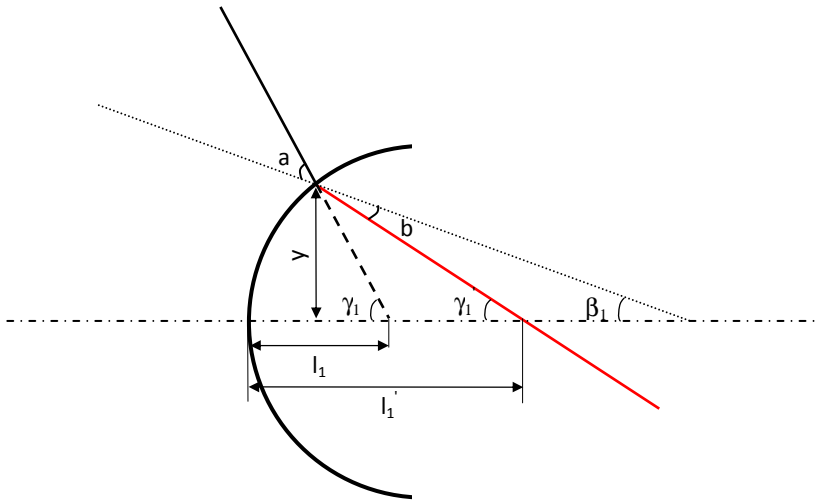

Figura 2.7 Refraction from first surface

Referring at figure 2.7 a = $\beta 1 - \gamma 1$ and applying the previous third-order approximation formulae we can write:

$$a = \frac{y}{r_1} - \frac{y}{l_1} \qquad (2.68)$$

and remembering that for a thin lens we have $F = F_1 + F_2$ substituting:

$$F_1 = F - F_2 = \frac{n-1}{r_1} \quad \text{and} \quad L_1 = L_1' - F_1 = L_1' - F + F_2 = \frac{1}{l_1} \qquad (2.69)$$

where F_1 and F_2 are the power of the first and second surface and F is the total power of the thin lens, we obtain then:

$$a = y\left[\frac{n(F - F_2) - L_1'(n-1)}{n-1}\right] \qquad (2.70)$$

and since the lens in thin we have that $L_1' = L_2 = L_2' - F_2$, and finally:

$$a = y\left[\frac{nF - F_2 - L_2'(n-1)}{n-1}\right] \qquad (2.71)$$

so that the angle a is function of the total power of the lens and of the power and vergence at the second surface.

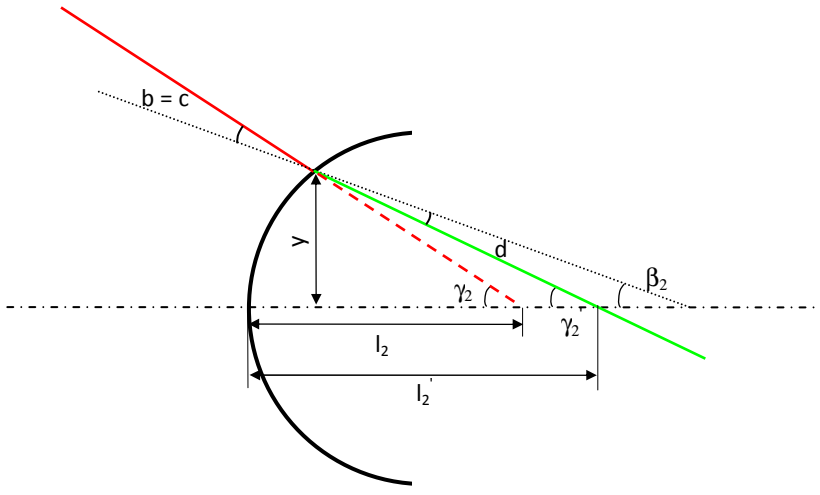

Figure 2.8 Refraction from second surface

As for angle a we can find similar equalities for angle d outgoing from the second surface, referring to figure 2.8, we have that a = $\beta 2 - \gamma_2'$ and applying third-order approximation we have:

$$d = \frac{y}{r_2} - \frac{y}{l_2'} \qquad (2.72)$$

and substituting:

$$F_2 = \frac{1-n}{r_2} \qquad (2.73)$$

where F_2 is the power of the second surface, we obtain then:

$$d = -y\left[\frac{F_2 + L_2'(n-1)}{n-1}\right] \qquad (2.74)$$

so that the angle d, taken with it sign, is function of the power and vergence at the second surface.

Consider finally the lens in Figure 2.9. A narrow pencil of light, represented by its chief ray, is incident upon the lens at the point G. The angle between the incident ray and the normal, C_1G, at the point G we will be denoted by a, the angle of refraction at this surface by b, and the angle between the normal and the optical axis by β_1. The distance C_1G in the tangential plane is the sagittal radius r_{1s}.

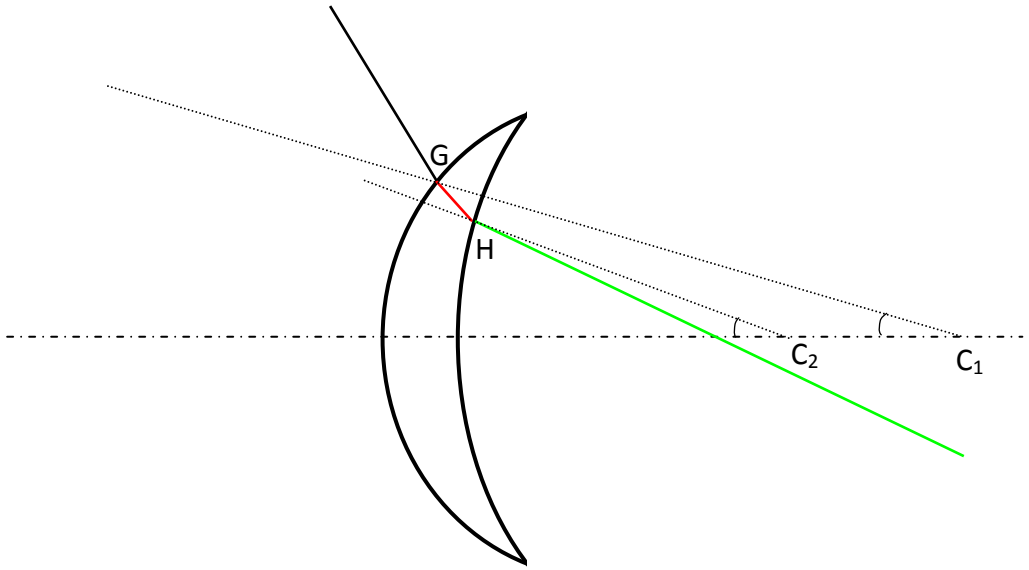

Figure 2.9 Thin lens in air

The ray then meets the second surface at the point H; the angle between the incidence ray and the normal is denoted by c. We will assume that the lens is infinitely thin and therefore the point G and H coincide. Then the vergence of the pencil leaving the first surface will equal the vergence entering the second. Finally the light emerges from the second surface into air with an angle of refraction d. The distance C_2H in the tangential plane is the sagittal radius r_{2s}, and the angle between the normal and the optical axis is denoted by β_2.

The narrow pencil of light is astigmatic since the incidence points are out of optical axis, the

distance of the sagittal focus from the point H will be denoted by s_2' and the distance of the tangential focus from H by t_2'.

We will now use Coddington's sagittal equation for aspherical surfaces placed into air; at the first surface we find:

$$\frac{n}{s_1'}-\frac{1}{s_1}=\frac{n\cdot\cos b-\cos a}{r_{1s}} \qquad (2.75)$$

and then at the second one:

$$\frac{1}{s_2'}-\frac{n}{s_2}=\frac{\cos d-n\cdot\cos c}{r_{2s}}. \qquad (2.76)$$

Since the lens is thin we can write the vergence equality $L_1' = L_2$ so that $n / s_1' = n / s_2$, adding the first equation to the second one we obtain:

$$L_{2s}'=L_{1s}+\frac{n\cdot\cos b-\cos a}{r_{1s}}+\frac{\cos d-n\cdot\cos c}{r_{2s}} \qquad (2.77)$$

where L_{2s}' is the sagittal vergence emerging from the lens. Similar to sagittal focus we can find the tangential one; so as previous the Coddington's tangential equation for first surface is

$$\frac{n}{t_1'}-\frac{\cos^2 a}{t_1\cdot\cos^2 b}=\frac{n\cdot\cos b-\cos a}{r_{1t}\cdot\cos^2 b} \qquad (2.78)$$

second surface:

$$\frac{\cos^2 d}{t_2'\cdot\cos^2 c}-\frac{n}{t_2}=\frac{\cos d-n\cdot\cos c}{r_{2t}\cdot\cos^2 c}. \qquad (2.79)$$

Since $n / t_1' = n / t_2$ we can add again the previous equations obtaining the tangential vergence:

$$L_{2t}'=L_{1t}\cdot\frac{\cos^2 a\cdot\cos^2 c}{\cos^2 b\cdot\cos^2 d}+\frac{n\cdot\cos b-\cos a}{r_{1t}}\cdot\frac{\cos^2 c}{\cos^2 b\cdot\cos^2 d}+\frac{\cos d-n\cdot\cos c}{r_{2t}}\cdot\frac{1}{\cos^2 d}. \qquad (2.80)$$

These expressions for the oblique astigmatic error exhibited by a lens still contain the angles of incidence and final emergence, a and d respectively, and they are true for every angle without any kind of approximation. We will now substitute their paraxial equivalents which we have determinate before.

For sagittal focus we have:

$$L_{2s}'=L_{1s}+\left[n\cdot\left(1-\frac{1}{2}b^2\right)-\left(1-\frac{1}{2}a^2\right)\right]\cdot\frac{1}{r_1}\cdot\left(1+\frac{q_1y^2}{2r_1^{\,2}}\right)+\left[\left(1-\frac{1}{2}d^2\right)-n\cdot\left(1-\frac{1}{2}c^2\right)\right]\cdot\frac{1}{r_2}\cdot\left(1+\frac{q_2y^2}{2r_2^{\,2}}\right) \qquad (2.81)$$

applying now Snell's law we have:

$$L_{2s}'=L_{1s}+\left[(n-1)\cdot\left(1+\frac{a^2}{2n}\right)\right]\cdot\frac{1}{r_1}\cdot\left(1+\frac{q_1y^2}{2r_1^{\,2}}\right)+\left[(1-n)\cdot\left(1+\frac{d^2}{2n}\right)\right]\cdot\frac{1}{r_2}\cdot\left(1+\frac{q_2y^2}{2\cdot_2^{\,2}}\right) \qquad (2.82)$$

remembering the thin lens power law $F = F_1 + F_2$ and $F_1 = (n - 1) / r_1$ and $F_2 = (1 - n) / r_2$, we have:

$$L_{2s}'=L_{1s}+F\cdot\left(1+\frac{a^2}{2n}\right)-F_2\cdot\frac{a^2-d^2}{2n}+\frac{y^2}{2}\cdot\left[\frac{q_1(F-F_2)^3}{(n-1)^2}\left(1+\frac{a^2}{2n}\right)+\frac{q_2F_2^{\,3}}{(1-n)^2}\left(1-\frac{d^2}{2n}\right)\right] \qquad (2.83)$$

finally we can substitute the values for a and d obtained before, and we can consider only terms up to the second degree so we have:

$$L_s'=L'+\frac{y^2F}{2n(n-1)^2}\left[F_2^{\,2}(2n+1)+F_2\left[2L_2'\left(n^2-1\right)-nF(n+2)\right]+n^2F^2-2nFL_2'(n-1)+L_2'^2(n-1)^2\right]+$$

$$+\frac{y^2}{2(n-1)^2}\left[q_1(F-F_2)^3+q_2F_2{}^3\right] \qquad (2.84)$$

where we assume that $L_{1s} + F = L'$ the outgoing vertex vergence from the second surface or the lens itself, and $L_{2s}' = L_s'$ the outgoing sagittal vergence from the second surface or the lens itself.

We would like to show that the first part of the equation is equal to the one gave by Jalie (1977) if we consider the surfaces of the lens spherical so that $q_1 = q_2 = 0$. The whole equation is equal to the one given by Atchison (1984) for aspherical surfaces where the terms containing y^4 are neglected. This expression can be revised in a more compact form as:

$$L_s' = L' + y^2 S. \qquad (2.85)$$

For tangential focus, applying the third-order equations, we have as well:

$$L_{2t}' = L_{1t}\cdot\left(1-a^2+b^2-c^2+d^2\right)+\left[n\cdot\left(1-\frac{1}{2}b^2\right)-\left(1-\frac{1}{2}a^2\right)\right]\cdot\frac{1}{r_1}\cdot\left(1+\frac{3q_1y^2}{2r_1{}^2}\right)\cdot\left(1+b^2-c^2+d^2\right)$$

$$+\left[\left(1-\frac{1}{2}d^2\right)-n\cdot\left(1-\frac{1}{2}c^2\right)\right]\cdot\frac{1}{r_2}\cdot\left(1+\frac{3q_2y^2}{2r_2{}^2}\right)\cdot\left(1+d^2\right) \qquad (2.86)$$

applying now Snell's law we have:

$$L_{2t}' = L_{1t}+L_{1t}\frac{\left(1-n^2\right)}{n^2}\left(a^2-d^2\right)+\left[(n-1)\cdot\left(1+\frac{a^2}{2n}\right)\right]\cdot\frac{1}{r_1}\cdot\left(1+\frac{3q_1y^2}{2r_1{}^2}\right)\cdot\left(1+\frac{a^2}{n^2}-\frac{d^2}{n^2}+d^2\right)$$

$$+\left[(1-n)\cdot\left(1+\frac{d^2}{2n}\right)\right]\cdot\frac{1}{r_2}\cdot\left(1+\frac{3q_2y^2}{2r_2{}^2}\right)\cdot\left(1+d^2\right) \qquad (2.87)$$

if we apply the laws for lens power we obtain as before:

$$L_{2t}' = L_{1t}+L_{1t}\left(a^2-d^2\right)\frac{\left(1-n^2\right)}{n^2}+(F-F_2)\left(1+\frac{a^2}{2n}\right)\left(1+\frac{a^2}{n^2}-\frac{d^2}{n^2}+d^2\right)+F_2\left(1+\frac{d^2}{2n}\right)\left(1+d^2\right)$$

$$+\frac{3y^2}{2}\left[\frac{q_1(F-F_2)^3}{(n-1)^2}\left(1+\frac{a^2}{2n}\right)\left(1+\frac{a^2}{n^2}-\frac{d^2}{n^2}+d^2\right)+\frac{q_2F_2{}^3}{(1-n)^2}\left(1+\frac{d^2}{2n}\right)\left(1+d^2\right)\right] \qquad (2.88)$$

after simplifications and neglecting terms above the second degree:

$$L_{2t}' = L_{1t}+L_{1t}\left(a^2-d^2\right)\frac{\left(1-n^2\right)}{n^2}+F\left(1+\frac{a^2}{2n^2}(n+2)+\frac{d^2}{n^2}\left(n^2-1\right)\right)-F_2\left(a^2-d^2\right)\frac{(n+2)}{2n^2}$$

$$+\frac{3y^2}{2}\left[\frac{q_1(F-F_2)^3}{(n-1)^2}\left(1+\frac{a^2}{2n^2}(n+2)+\frac{d^2}{n^2}\left(n^2-1\right)\right)+\frac{q_2F_2{}^3}{(1-n)^2}\left(1+\frac{d^2}{2n}(2n+1)\right)\right] \qquad (2.89)$$

finally we can substitute again the values for a and d obtained before, and consider only terms up to the second degree so we have:

$$L_t' = L'+\frac{y^2F}{2n(n-1)^2}\left[F_2{}^2(4n+5)+F_2\left[2(3L_2'+2L)\left(n^2-1\right)-F(n+2)^2\right]-2FL_2'(n-1)(n+2)+nF^2(n+2)+\right.$$

$$\left.+L_2'^2(n-1)^2(2n+1)-2nFL\left(n^2-1\right)+4LL_2'\left(n^2-1\right)(n-1)\right]+\frac{3y^2}{2(n-1)^2}\left[q_1(F-F_2)^3+q_2F_2{}^3\right] \qquad (2.90)$$

where we assume that $L_{1t} + F = L'$ the outgoing vertex vergence from the second surface or the lens itself, and $L_{2t}' = L_t'$ the outgoing tangential vergence from the second surface or the lens itself. Again this equation is equal to Jalie one if we consider spherical surfaces, and to Atchison one.

We can also show that the quantity in the second bracket is equal to the previous one except for a scale factor. The main difference between sagittal and tangential equation is that the tangential vergence depend by the incoming vergence L, while the sagittal vergence is not. This

expression can be revised in a more compact form as:

$$L_t' = L' + y^2 T. \qquad (2.91)$$

2.2.6. Aberration minimization

Along to correct an eye aberration with a spectacle lens, the back vertex focus of the lens must be made to coincide with the eye's far point. Since the far point is conjugate with the most sensitive portion of the retina, the fovea, rays of light that pass through the pupil of the eye will then be focused on to the fovea (see chapter 3 for more details). The average pupillary aperture in normal conditions 4 mm in diameter and therefore only a small portion of the lens may be used at any one time. When the eye looks straight ahead, it is said to be in its primary position (figure 2.10) and the line passing through the centre of the pupil, P, and the fovea, FC, is the primary line of the eye.

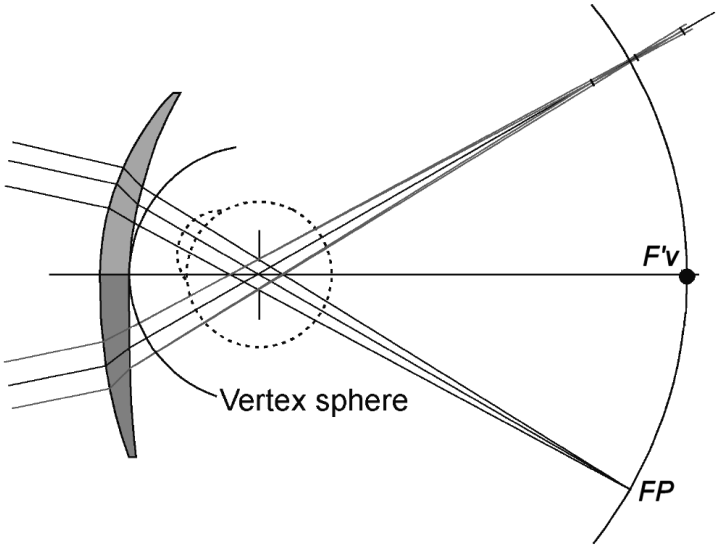

Figure 2.10 Far point sphere (Alonso and Alda, 2003)

The back vertex focus of the lens, F'v, then coincides with the eye‘s far point, FP. When the eye rotates to view a distant object which lies off the primary line, the far point, which remains conjugate with the fovea, also rotates as shown in Figure 2.9. Since the eye may rotate about its centre of rotation, H, the far point must also rotate, but remaining at a fixed distance from the centre of rotation of the eye. We can imagine that as the far point rotates it traces a spherical surface concentric with the centre of rotation of the eye.

This surface upon which the far point remains as the eye rotates is called the far point sphere. The far point sphere, whose centre lies at the eye‘s centre of rotation, lies behind the eye in hypermetropia as shown in Figure 346, and in front of the eye in myopia (remembering the sign convention). Its radius of curvature is g – f’v where f’v is the back vertex focal length of the correcting lens and g is the distance from the back vertex of the lens to the centre of rotation H.

The aim of spectacle lens design is designing a single lens which will focus narrow pencils of light which pass, after refraction, through H, upon the far point sphere. The narrow pencils may be incident parallel to the optical axis of the lens, or obliquely, but in all cases the lens must produce point images of distant point objects upon the far point sphere (Jalie, 1977).

A similar condition can be found for near vision and the above we can find a sphere that rotate along the rotation of the eye and is called near point sphere.

The images produced by the spectacle lens will of course suffer from all the aberrations described in the last chapter but owing to the smallness of the stop at R we can immediately see that the effects of spherical aberration and coma can be ignored. To design a lens that minimizes the aberrations we have the following variables:

- distance, g , from the back vertex of the lens to the centre of rotation
- thickness, t, of the lens
- refractive index, n, of the material of the lens
- the individual surface powers, F_1 and F_2, which sum must remain equal to the total power, F, of the lens.

Since the distance of the lens from the eye and the refractive index cannot be modified by designers the only real variable which remains is the form of the lens.

With this one variable it is possible to correct only phew aberrations at a time. Since the effect of distortion does not alter the position of the image, but merely its shape, we will deal first with the oblique astigmatism. We deal now with the so called best form lenses.

2.2.6.1. Best form lens: Tscherning's ellipse

From previous chapters we have found third-order approximated formulas for sagittal, L'_s, and tangential vergence, L'_t, which denote the distance from the interception point at the surface of the principal ray and the image focus point Q's and Q't respectively. The distance between Q's and Q't expressed in dioptres is called oblique astigmatic error, and is denoted by A and we can write:

$$A = L_t' - L_s'. \qquad (2.92)$$

Instead of the vergence L we can use the tangential (F_t') and sagittal (F_s') vertex power calculated from a reference sphere called vertex sphere. The vertex sphere is concentric with the centre of rotation of the eye, H, and have radius equal to l_2' so that touch the back vertex of the lens. This reference plane allows the comparison of different lens form performance which may have different distances from the back surface to the vertex sphere which from the geometry of the figure 2.9 is simply found as:

$$v = \frac{y_2}{\sin\gamma_2'} - l_2' \qquad (2.93)$$

To minimize the oblique astigmatism of the lens we can then choose to different approaches: let the astigmatism itself be zero, or let the mean focus between Q's and Q't, the so called circle of least confusion, lies on the far point sphere.

The first technique is known till the early century and in 1904 Tshcerning published his results for spherical surfaces and relating oblique astigmatism to the first surface power F_1 and total power F. For spherical surfaces, such as q = 0, the previous formulas reduce to be quadratic in these terms and can be plotted in F against F_2 (in our dissertation) graphs that will take the common shape of ellipses known as Tscherning's ellipses. We will now see the computational form of these ellipses and them expansion to aspherical surfaces.

2.2.6.2. Best form lens: zero astigmatism error condition – point focal lens

For a given position of the eye's centre of rotation H, which distance from the back vertex of the lens is equal to l_2' (usually 27 or 25 mm), we can find from previous formulas that oblique astigmatism error is:

$$A = L_t' - L_s' = \left(L' + y^2 T\right) - \left(L' + y^2 S\right) = y^2 (T - S). \qquad (2.94)$$

Equating this equation to zero we will find the first condition to eliminate oblique astigmatism along with third-order theory, we will see further that by a forward ray trace that this condition is able only to minimize the astigmatism but not to fully eliminate it. So that substituting previous equations we will finally have:

$$\frac{F}{2n(n-1)^2}\left[F_2{}^2(2n+4)+F_2\left[4(L_2{}'+L)(n^2-1)-2F(n+2)\right]-4FL_2{}'(n-1)+2nF^2+\right.$$

$$\left.+2nL_2{}'^2(n-1)^2-2nFL(n^2-1)+4LL_2{}'(n^2-1)(n-1)\right]+\frac{1}{n(n-1)^2}\left[q_1(F-F_2)^3+q_2F_2{}^3\right]=0 \qquad (2.95)$$

This equation derives from previous formulae that are true both for distant and near vision; and not only for spherical surfaces, as in original Tscherning work but also for aspherical surfaces. This equation is cubic in F_2 if q_1 or q_2 are not equal to zero so that we are considering aspherical surfaces. In the following figures for distant (figure 2.11a) or near (figure 2.11b) vision we have depict the solution of this equation with q_2 from -0.2 to 0.6 with 0.1 steps, $q_1 = 0$, and l' = 1 / L' = 300 mm for near vision. The equation reduce instead to a quadratic form if both the surface are spherical and we will found the common Tscherning's ellipses that are remarked in bold in figures.

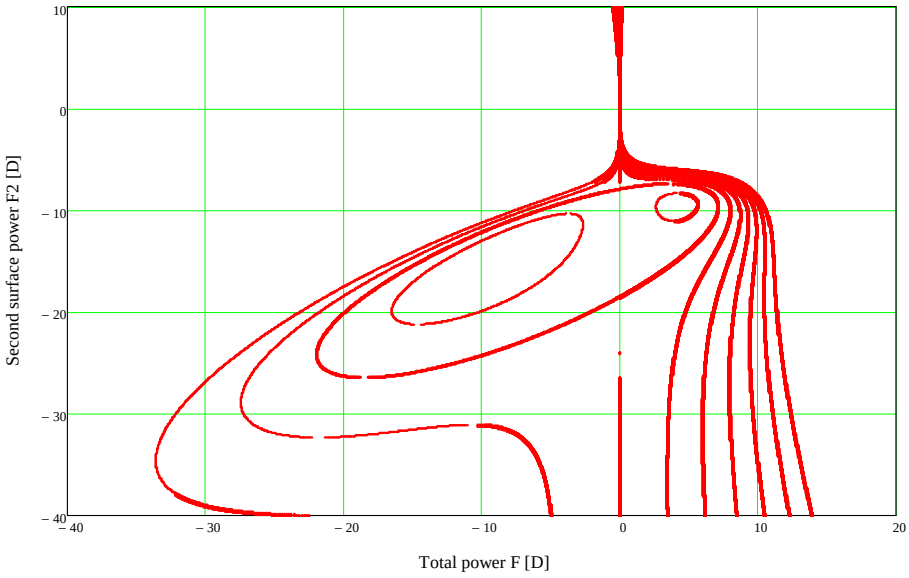

(a)

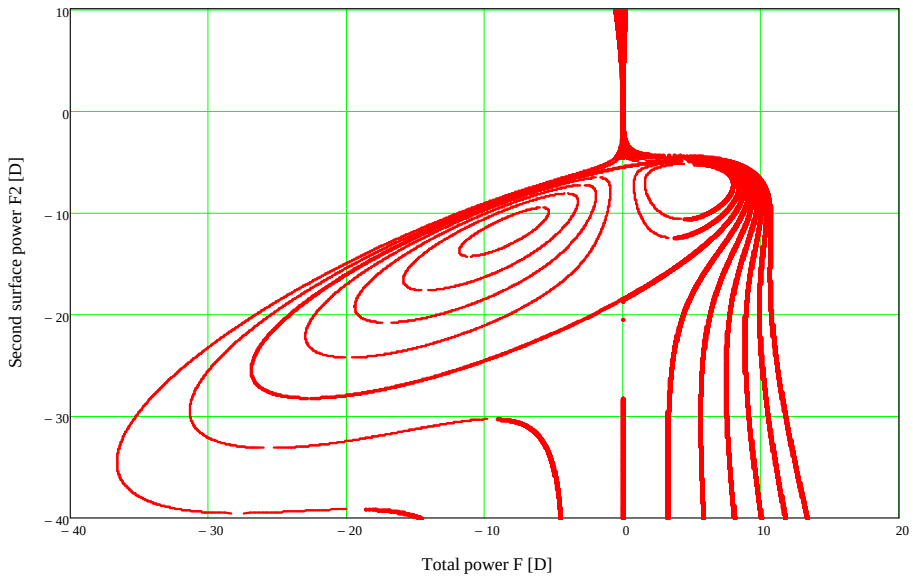

(b)

Figure 2.11 (a) point focal lens solutions for distant vision for different back surface q_2 values; (b) point focal lens solutions for near (30 cm) vision for different back surface q_2 values

2.2.6.3. Best form lens: zero mean oblique error condition – Percival lens

As said previously another condition so that the astigmatism is equal to zero in third-order theory is to put the circle of least confusion on the far (or near) point sphere. This let the sagittal and tangential foci to fall one per side of that sphere and equidistant from that.

This lead to vergence equalities (that can be transformed in power equalities for distant vision letting L be substituted by F):

$$\frac{L_t'+L_s'}{2}-L'=0 \qquad (2.96)$$

that is the Percival condition; the left hand is also called mean oblique error. Again substituting we will have:

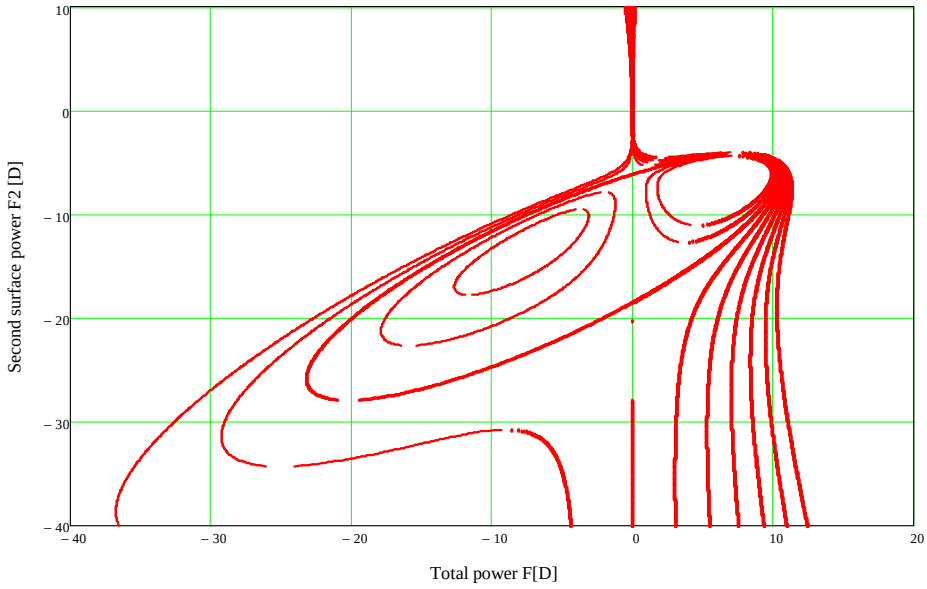

(a)

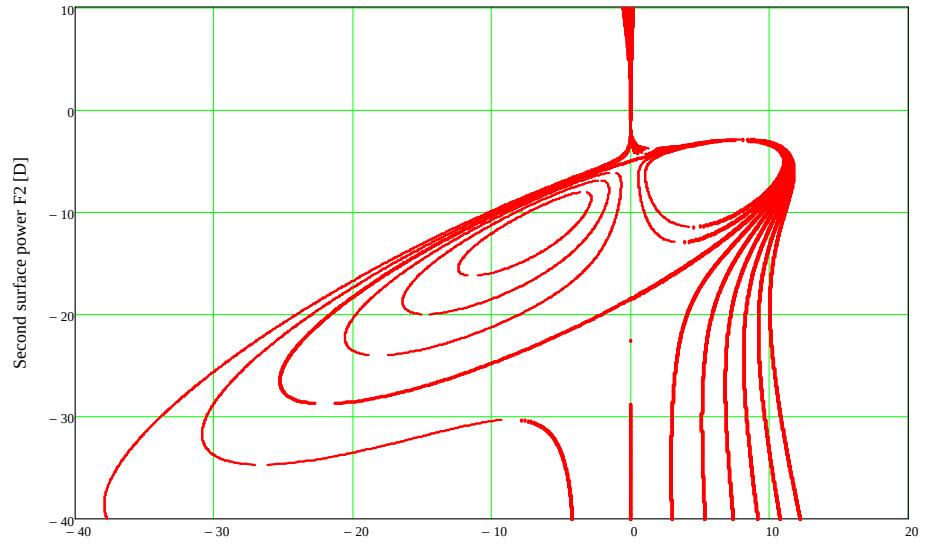

(b)

Figura 2.12 (a) Percival lens solutions for distant vision for different back surface q_2 values; (b) Percival lens solutions for near (30 cm) vision for different back surface q_2 values

$$\frac{F(n+1)}{n(n-1)^2}\left[3F_2{}^2+F_2\left[2(2L_2'+L)(n-1)-F(n+2)\right]+nF^2-(2L_2'+nL)F(n-1)+\right.$$

$$\left.+L_2'^2(n-1)^2+2LL_2'(n-1)^2\right]+\frac{2}{(n-1)^2}\left[q_1(F-F_2)^3+q_2F_2{}^3\right]=0 \qquad (2.97)$$

That again is cubic in F_2 if we consider at least one aspheric surface, and collapse to Tscherning ellipses if we consider spherical surfaces. In figure 2.12 we have depict the solution of the previous equation for q_2 from -0.2 to 0.6 with 0.1 steps, $q_1 = 0$, and l' = 1 / L' = 300 mm for near vision.

2.2.7. Spectacle lens analysis

In the previous chapters we have limited the treatment of spectacle lens design to third-order theory and thin lenses, although we have already considered aspherical surfaces. To fully analyse the performances of a lens, such as best form lenses that minimize the astigmatism error it is necessary to use accurate trigonometrical computation.

The third-order relationships are not false, but are limited to a so called paraxial zone around the optical axis where the angles do not exceed about l5°. We will find, however, that a lens form which the third-order calculation predicts should be free from astigmatism at l0° may not be tree from astigmatism at 30°. Since the movements of the eye behind the lens may also have a maximum range of 35 – 40° we have to go behind the third-order theory.

A scholastic procedure for designing a best form lens of a given back vertex power is as follows. A range of different base curves is chosen for investigation. The preliminary choice could be based on the results indicated by third-order calculations.

It is assigned a suitable centre thickness so that the lens has the back vertex power intended. An average centre of rotation distance is then chosen for the lens. When all the lens parameters have been decided the trigonometrical ray-tracing procedure can commence.

Starting at the eye‘s centre of rotation, the eye is assumed to rotate through an angle γ', from the optical axis and the ray which enters the pupil of the eye is traced backwards through the lens. This backward ray-trace allows determining the angles of incidence and refraction at each surfaces, the oblique ray path within the lens and the distance from the back surface of the lens to the vertex sphere (chosen as reference plane).

Completed the backward ray-trace through the lens, a forward ray-trace is now performed to determine the tangential and sagittal powers of the lens for the angle under consideration. These oblique powers are referred to the vertex sphere and called the oblique vertex sphere powers, from which we can find the oblique astigmatic error and the mean oblique error.

2.2.7.1. Line of sight: backward ray-trace

We will give now the equations for the backward ray-trace, from the geometry of the figure and using the sine theorem, according to sign convention:

$$\sin i' = (l' - r_{se})\frac{\sin\gamma'}{r_s} \qquad (2.98)$$

where we have indicated with r_{se} the interception of the sagittal ray with optical axis, we would like to remember that if the surface is spherical then $r_{se} = r_s = r$.

From the Snell’s law we have:

$$\sin i = \frac{n'}{n}\sin i' \qquad (2.99)$$

and from trigonometrical relations:

$$\gamma = \gamma' + i' - i \qquad (2.100)$$

and again the sine theorem:

$$l - r_{se} = r_s \frac{\sin i}{\sin \gamma} \qquad (2.101)$$

from which we can find the interception between the incident ray and the optical axis l. To continue the backward ray-trace from the second surface to the first surface we also need to know the path length inside the lens t_e, from trigonometrical equalities we can then write:

$$t_e = \frac{y_1 - y_2}{\sin \gamma_2} \qquad (2.102)$$

where y_1 is the interception height to the first surface and y_2 is the interception height to the second surface and we can write for both heights the relationship with the radius r and the angle between the normal of the surface and the optical axis β:

$$y = r_s \cdot \sin\beta \qquad (2.103)$$

We would like to underline that in the previous equations we have already substitute the radius r for a spherical surface with sagittal radius r_s that is the radius of curvature of the surface at the interception point in tangential plane.

2.2.7.2. Mean power and astigmatism: forward ray trace

After the backward ray-trace we know all the quantities to perform forward ray-trace using Coddington's equations, where we can write the astigmatic constant in a more useful form:

$$\frac{n'\cos i' - n\cos i}{r} = \frac{n'\sin(i - i')}{r \cdot \sin i} \qquad (2.104)$$

where r may be sagittal or tangential radius depend on which equation we are looking at.

We also want to remember that we are no more considering thin lenses. So instead of the previous treatment we have to write:

$$s_2 = s_1' - t_e \quad \text{and} \quad t_2 = t_1' - t_e \qquad (2.105)$$

that link the object sagittal and tangential focus of the second surface with the image sagittal and tangential focus of the first surface, as it can be seen the path inside the lens play an important role, and can make the difference between third-order theory best form lens performance and the real ray-trace.

2.2.8. Thick lens in air with aspherical surfaces

We will now show how the analysis exposed before can be applied to a thick lens in air with aspherical surfaces. For clarify the exposition we will give a numerical example (taken from Jalie, 1967) of a point focal lens with total power F = –6.00 D, a centre thickness t = 2 mm and a refraction index n = 1.5. We want to analyse that lens for distant vision so using the formula (2.95) we find that for $q_1 = 0$ and $q_2 = -1.3$ we can take $F_2 = -7.00$ D so we have a flat first surface with F_1 = +1.00 D. The first surface power is found applying the following formula for thick lens power:

$$F_1 = \frac{F - F_2}{1 + \frac{t}{n}(F - F_2)}. \qquad (2.106)$$

From the power expression we can easily find the vertex radius of the first and second surface:

$$F_1 = \frac{n-1}{r_1} \qquad F_2 = \frac{1-n}{r_2} \qquad (2.107)$$

that in our example are r_1 = 500.667 mm and r_2 = 71.429 mm.

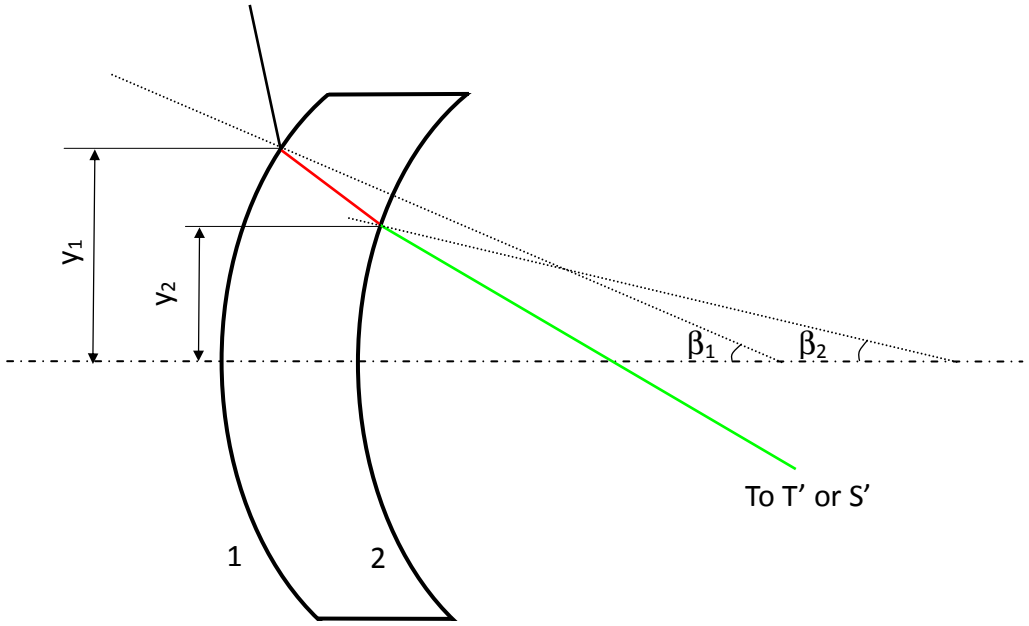

Figura 2.13 far point sphere

Full details of the ray-trace can be seen in figure 2.13. We start performing a back ray-trace at the angle γ_2' = 35° that denote rotation angle at which the eye is looking at. The centre of rotation behind the vertex of the second surface (the back vertex of the lens) is denoted by l_2' = 27 mm. A problem that we haven't achieved yet is to find the interception point between an aspherical surface (that we remember is in the form $z = \left(r - \sqrt{r^2 - (1+q)y^2}\right) / (1+q)$) and a straight line along a fixed direction (in this case is the line of sight along angle γ' so we can of course write $y = \tan\gamma' \cdot (z - z_e) + y_e$)). Solving the simple system of equations between the line equation and the aspherical surface lead to:

$$z_e = \frac{r + l\tan^2\gamma - \sqrt{r^2 + 2rl\tan^2\gamma - (1+q)l\tan^2\gamma}}{1 + q + \tan^2\gamma} \qquad y_e = (l - z_e)\tan^2\gamma \qquad (2.108)$$

these are the coordinates of the interception point E_2 with the aspherical surface of vertex radius r and aspherical coefficient q and the line passing through the optical axis in l forming with it an angle y. Even if we are referring now to the second surface we omit the subscripts and the apexes since the previous formulae have a general validity. In our example we would like to find the interception between the line of sight at 35° and the second surface so we have z_{e2} = 2.116 mm and y_{e2} = 17.424 mm.

After we have found the interception point E_2 we have to find the sagittal and tangential radii at that point of the surface so referring to (2.51) we have that the sagittal radius r_{2s} = 74.140 mm and the tangential radius r_{2t} = 79.875 mm.

From the sagittal radius and the interception point we can find then the angle β between the normal of the surface and the optical axis:

$$\sin\beta = \frac{y_e}{r_s} \qquad (2.109)$$

and substituting our results we have β = 13.593°. Tracing a line from interception point E along normal direction β we can find the interception point between the normal and the optical axis r_{se2}:

$$r_{se2} = \frac{y_{e2}}{\tan\beta} + z_{e2} \qquad (2.110)$$

that for the second surface has a value of 74.179 mm.

After this we can find the outgoing angle from the second surface using the (2.74) that in our case is d = –21.407°. Using the Snell's law and remembering that in this case n' = 1 and n = 1.5, since the media on the left part of the surface is the lens and on the right part is air, we can find the incidence angle to the second surface

$$c = \operatorname{asin}\left(\frac{1}{1.5}\sin d\right) = -14.083^\circ . \qquad (2.111)$$

As we have stated before continue the back ray-trace we have to find the distance l between the vertex of the surface and the interception between the incidents ray at the surface and the optical axis, so that:

$$l_2 = r_{2s}\frac{\sin c}{\sin\gamma} + r_{se2} = 35.338 \text{ mm} \qquad (2.112)$$

where $\gamma = \gamma' + d - c = 27.676^\circ$.

We have now found all the data concerning the second surface. Now we have to move the axis origin to the first surface that is at distance t from the second surface along z-axis. We have to add the quantity t to all the data referring to optical axis, in particular:

$$l_1' = l_2 + t = 37.338\text{mm} . \qquad (2.113)$$

Tabella 2.1 Back ray-trace for a thick aspheric lens

F = -6.00 D, t = 2.000 mm, n = 1.5, q_1 = 0, q_2 = –1.3			
l_2'	27.000 mm	4.224 mm	t_e
$\gamma 2'$	35.000°	27.676°	$\gamma 1' = \gamma 2$
F2	-7.00 D	+1.00 D	F1
y_{e2}	17.424 mm	19.386 mm	y_{e1}
z_{e2}	4.116 mm	0.375 mm	z_{e1}
r_{2s}	74.140 mm	500.667 mm	r_{1s}
r_{2t}	79.875 mm	500.667 mm	r_{1t}
$\beta 2$	13.593°	2.219°	$\beta 1$
d	–21.407°	–40.147°	a
c	–14.083°	–25.457°	b
$l_2 = l_1'$	37.338 mm	21.631 mm	l_1
$\gamma 2$	27.676°	42.366°	$\gamma 1$

As before we can use the (2.108) to find the interception point E_1 between the first surface and

the back ray which has in this case $l = l_1'$ and an angle with the optical axis $\gamma = 27.676°$ as calculated before. After that we can perform all the calculation to find the interception angle a with the first surface and the refracted angle b, and using the (2.38) we can finally find the path length that the ray trace inside the lens $t_e = 4.224$ mm.

Before applying the Coddington's equations to find the optical properties of the designed lens is useful to summarise in table 2.1 the data that we have found with the back-ray trace:

These results are shown referring to the apex of the first surface as axis origin, so that we have already added the lens thickness t to second surface data.

Now we have all the necessary quantities to find the mean power and astigmatism for 35° line of sight direction along a nominal point focal lens. Applying Coddington's equation for first surface in which n' = n, n = 1, i = a, i' = b, 1 / s = 1 / t = 0, $r = r_{1s}$ or r_{1t} whether we considering sagittal or tangential direction we find:

$$s_1' = r_{1s}\frac{\sin a}{\sin(a-b)} = 1273 \text{ mm} \qquad t_1' = r_{1t}\frac{\sin a \cdot \cos^2 b}{\sin(a-b)} = 1038 \text{ mm} \tag{2.114}$$

where we have used the (2.92) for the astigmatism error into the Coddington's equations. This is useful since we take trace of the signs. Propagating the ray inside the lens we can find the incident rays to the second surface that are:

$$s_2 = s_2' - t_e = 1269 \text{ mm} \qquad t_2 = t_2' - t_e = 1034 \text{ mm}. \tag{2.115}$$

Applying now Coddington's equation for second surface in which n' = 1, n = n, i = c, i' =d, $s = s_2$, $t = t_2$ and $r = r_{2s}$ or r_{2t} whether we considering sagittal or tangential direction we find:

$$s_2' = \frac{1}{\frac{n}{s_2} - \frac{\sin(c-d)}{r_{2s}\sin c}} = -169.948 \text{ mm} \qquad t_2' = \frac{\cos^2 d}{\frac{n\cdot\cos^2 c}{t_2} - \frac{\sin(c-d)}{r_{2t}\sin c}} = -166.891 \text{ mm} \tag{2.116}$$

From which we can find the vergence $L_s' = 1 / s_2' = -5.88$ D, $L_t' = 1 / t_2' = -5.99$ D expressed in dioptres. As mentioned before we can find the sagittal and tangential vergence referred to the vertex sphere so that we have to find before the distance between the interception point E_2 on the second surface and the vertex sphere of radius l_2'. Using the (2.91) in this case we find that v = 3.378 mm. Subtracting this quantity from s_2' and t_2', we can find the vergence $L_{sv}' = 1 / (s_2' - v) = -5.77$ D and $L_{tv}' = 1 / (t_2' - v) = -5.87$ D that are the vergence referred to vertex sphere. Using the vertex sphere as reference allow to compare lenses with different form (i.e. different aspheric coefficients q) but this will not slightly change the following treatment. Remembering that the mean power F_m is:

$$F_m = \frac{L_{sv}' + L_{tv}'}{2} \tag{2.117}$$

we can find the mean oblique error $MOEv = F_m - F = 0.179$ D where F_m is the mean power calculated as above, F is the nominal vertex power of the lens (e.g. –6.00 in our case) and the letter v means that we are referring to vertex sphere. Remembering that the oblique astigmatism error, referred to vertex sphere, OAEv is equal to:

$$OAEv = L_{sv}' - L_{tv}'$$

we finally find A = –0.104 D. Before conclusions we show in a table a summary of the data founded in this example.

Tabella 2.2 Mean power error and astigmatism for thick aspheric lens

F = -6.00 D, t = 2.000 mm, n = 1.5, $q_1 = 0$, $q_2 = -1.3$			
s_1	∞	∞	t_1
s_1'	1273 mm	1038 mm	t_1'
s_2	1269 mm	1034 mm	t_2
s_1'	–169.948 mm	–169.891 mm	t_1'
L_{sv}'	–5.769 D	–5.873 D	L_{tv}'
MOEv	0.179 D	–0.104 D	OAEv

We can now show the difference between the third order approximation thin lens and the real ray trace. From theoretical assumptions we should find an OAEv equal to zero since we have designed a zero astigmatism lens. Of course this is not true but the error that we commit is really low, and it can be hardly recognizing by the human eye which threshold is about 0.25 D of astigmatism. If we perform this calculation along different angles γ_2' with a 5° step we can show the results in the below graph.

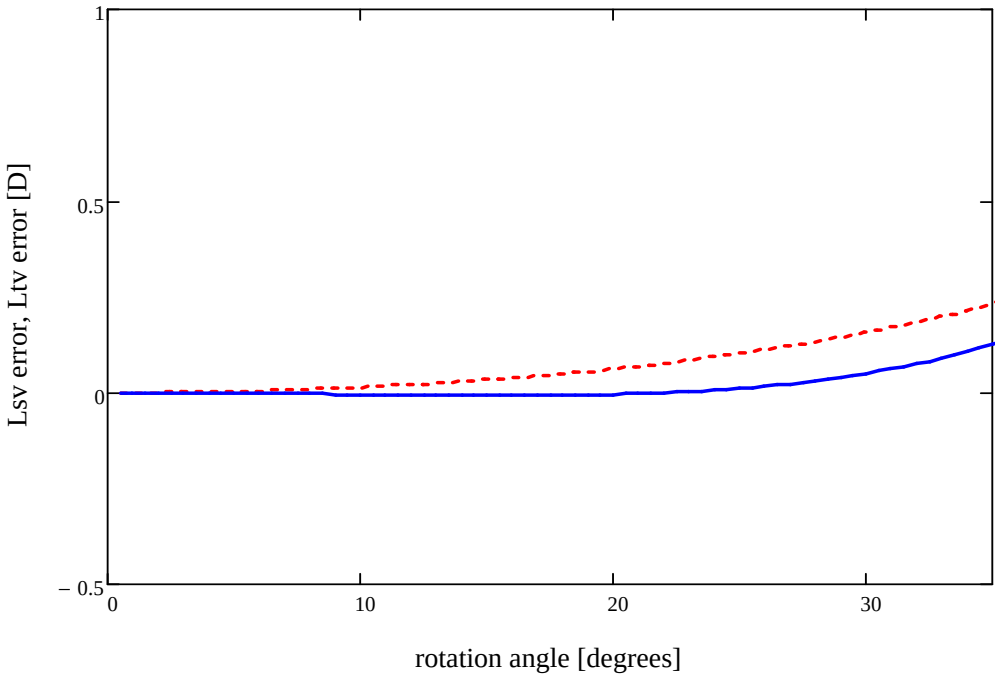

Figura 2.14 Zero astigmatism thick lens with aspherical surfaces along different rotation angles.

In figure 2.14 we have graph the outgoing sagittal vergence error $L_{sv}' - F$ (dot line), and the tangential one $L_{tv}' - F$ (solid line), where F is the nominal vertex power. As it can be seen through the whole field of vision the outgoing vergence is really low and is close to zero (and so the astigmatism is).

This lead to the conclusion that the zero astigmatism solution that we have found before, under the hypothesis of third order theory and thin lens, gives a good approximation and a first step for further and more suitable lenses.

Since before we have found the errors referred to the vertex sphere we want now to show another example. Instead of using a simple conicoids surface as we have done till now we would like to introduce more complex surfaces. As Atchison (1992) we will use the following expression:

$$z = \frac{y^2}{r + \sqrt{r^2 - (1+q)y^2}} + A_4 y^4 + A_6 y^6 + A_8 y^8 + A_{10} y^{10} \qquad (2.118)$$

that has additional coefficients A called figuring terms. With such an aspherical surface we are able to modify the surfaces especially in the peripherical part without slightly modify the optical central zone.

These modifications allow the manufacturing of lenses more thin then simple conicoids lenses, which is for sure one of designers aims. If we consider to modify the back surface of the previous example adding the figuring term $A_{10} = -2 \cdot 10^{-15}$ mm^{-9} we can perform a ray trace through the lens as we have done before. We have however to remember that we are no more considering a conicoid surface and so we have to calculate, with a numerical approach, the interceptions between the line of refraction and the surface during the back ray trace, and we have to calculate also the sagittal and tangential radius that have been modified especially in the peripheral zone of the lens. For more details about the radii calculation we refer to Appendix B.

In the figure 2.15 we graph the sagittal and tangential vergence error for different rotation angle of the lens modified with figuring term.

As predicted the central zone is not slightly modified by the new term that instead decreases the optical performance of the lens in the peripheral zone, while it increase the mechanical one in that zone (the lens is more thin with a loss of weight of 8% against a spherical lens of same vertex power (Atchison, 1992)).

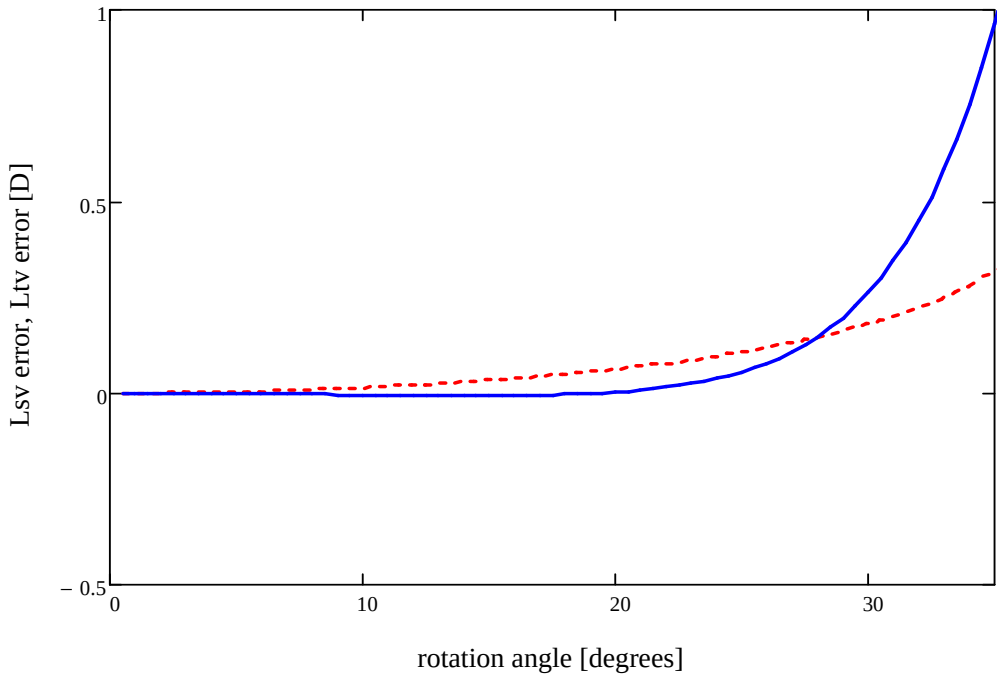

Figura 2.15 Zero astigmatism thick lens with aspherical surfaces along different rotation angles (Atchison, 1992)

2.3. Optics of the human eye

The description of the anatomy of the eye is provided according to Atchison and Smith (2000). The refracting elements of the eye are the cornea and the crystalline lens. In order to provide a good quality retinal image, these elements must be transparent and have appropriate curvatures and refractive indices. Refraction takes place at four surfaces, the anterior and posterior interfaces of the cornea and the lens, and there is also continuous retraction within the lens.

In this part we describe the optical structure of the normal cornea and lens taking into account that in many eyes there are significant departures from these norms. Some of these are due to serious ocular defects or irregularities, which can have a major impact on vision; some other just depends on the deviation from one subject to another one. There are also changes with age, gender and accommodation status of the eye.

2.3.1. Cornea

The cross-sectional structure of the cornea is shown in figure 2.16. The whole cornea is protected by a tear film of about 4-7 μm thickness, which is composed of aqueous and mucous layers but it doesn't provide any significant refractive power.

The front surface of the cornea is the epithelium which consists of approximately six layers of cells, after that there's the Bowman's membrane, formed by collagen fibrils. The stroma is the thickest part of the cornea providing about the 90% of the total thickness and consists of collagen lamellae. After stroma there's Decemet's membrane and endothelium, which consists of a single layer of hexagonal cells.

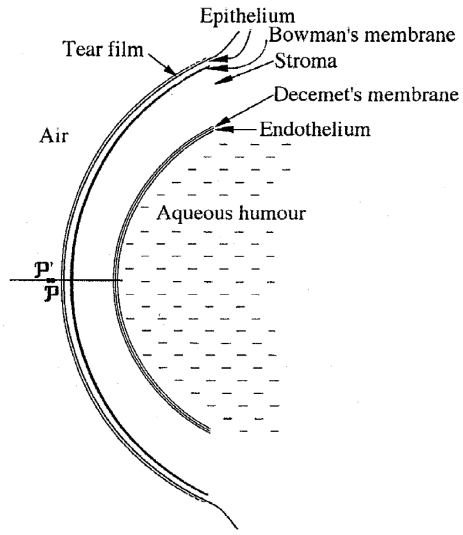

Figura 2.16 Cornea cross-section (Atchison and Smith, 2000)

The paraxial region of a corneal surface can be described with an apical radius of curvature. However this is not sufficient, since the radius of curvature increases with distance from the surface apex, so that the surface flattens away.

The shape of the anterior corneal surface has been extensively studied, especially over the central 7 mm, which is the zone that forms the foveal image.

Tabella 2.3 Experimental results of anterior corneal radii and asphericity

author	year	num. of eye	method	anterior corneal radius (mm) (val ± SD)	asphericity (val ± SD)
Stenström[1]	1948	1000	—	7.86 ± 0.80	—
Sorsby et al.[1]	1957	194	—	7.79 ± 0.27	—
Townsley[1]	1970	350	—	—	–0.30
Mandell and St. Helen[1]	1971	8	—	—	–0.23
Lowe and Clark[1]	1973	92	Slit lamp	7.65 ± 0.27	—
Kiely et al.[1]	1982	176	—	7.72 ± 0.27	–0.26 ± 0.18
Edmund and Sjøntoft[2]	1985	40	—	—	–0.28 ± 0.13
Guillon et al.[1]	1986	220	—	7.77 ± 0.25	–0.19 ± 0.16
Sheridan and Douthwaite[2]	1989	56	—	—	–0.11
Royston et al.[1]	1990	15	Slit lamp Purkinje image	7.77 7.77	—
Lam and Loran[2]	1991	65	—	—	–0.11
Dunne et al.	1992	80	Purkinje image	7.96 ± 0.03 (young) 7.77 ± 0.06 (old)	—
Patel et al.[2]	1993	20	—	—	–0.01 ± 0.25
Eghbali et al.[2]	1995	41	—	—	–0.18 ± 0.21
Carney et al.[2]	1997	105	—	—	–0.402 ± 0.23 – 0.032SR
Budak et al.[2]	1999	150	—	—	–0.04 ± 0.23
Lam and Douthwaite	2000	240	Purkinje image	7.66 ± 0.26 (young) 7.70 ± 0.23 (old)	–0.30 ± 0.13[3]
Guirao et al.[2]	2000	27	—	—	–0.10 ± 0.06 (young)
Dubbelman et al.	2002	83	Slit lamp	8.0 ± 0.27 – 0.004A	–0.2 ± 0.18 + 0.0003A
Dubbelman et al. (Norrby)	2005	83	Slit lamp	7.87 ± 0.27	–0.18 ± 0.18
Atchison	2006	121	Video-keratography	7.77 + 0.0221SR	–0.148 ± 0.107

[1]Data from Liou and Brennan (1997), [2]Data from Atchison (2006), [3]Data from Lam and Douthwaite (1997)

A popular formula for describing a cross-section of a corneal surface is Baker's equation introducing the shape factor (Baker 1943):

$$y^2 - 2rz + (1+q)z^2 = 0 \qquad (2.119)$$

where r is the apical radius and q is the shape factor, called before aspherical coefficient. This is in general the mathematical description of a conic section, which optical characteristics has been extensively shown in the previous chapters.

The formula describing the cross-sectional shape can easily be used to define a three dimensional surface. By building the surfaces of revolution one gets the associated three dimensional objects, the conics are extended to conicoids:

sphere to spheroid; ellipse to ellipsoid; parabola to paraboloid; hyperbola to hyperboloid.

Over the last century many authors set up different techniques (see appendix C) to acquire the radius and asphericity of anterior corneal surface, in table 2.3 it is presented an overview of the results of different methods.

Frequently the anterior corneal surface exhibits toricity; which produces astigmatism. In young eyes, the radius of curvature is generally greater in the horizontal than in the vertical meridian (referred as with-the-rule astigmatism), but this trend reverses with an increase in age becoming against-the-rule in older people.

Tabella 2.4 Experimental results of posterior corneal radii and asphericity

author	year	num. of eye	method	posterior corneal radius (mm) (val ± SD)	asphericity (val ± SD)	A/P ratio
Lowe and Clark[1]	1973	92	Slit lamp	6.46 ± 0.26	—	P = –(0.791A + 0.409)
Royston et al.[1]	1990	15	Slit lamp	6.35	—	1 : 0.817
			Purkinje image	6.40		1 : 0.824
Dunne et al.	1992	80	Purkinje image	6.45 ± 0.04 (young)	—	1 : 0.823
				6.25 ± 0.06 (old)		1 : 0.824
Patel et al.[2]	1993	20	—	5.81 ± 0.41	–0.42	1 : 0.81
Lam and Douthwaite	2000	240	Purkinje image	6.39 ± 0.26 (young)	–0.66 ± 0.38[3]	P =–(0.90A – 0.54)
				6.39 ± 0.24 (old)		
Dubbelman et al.	2002	83	Slit lamp	6.6 ± 0.27 – 0.005A	–0.1 ± 0.1 – 0.007A	1 : 0.81 ± 0.02
Dubbelman et al. (Norrby)	2002	83	Slit lamp	6.40 ± 0.8	–0.38 ± 0.27	1 : 0.81 ± 0.02

[1]Data from Liou and Brennan (1997), [2]Data from Atchison (2006), [3]Data from Lam and Douthwaite (1997)

Baker's formula is a simple method to describe the shape of the cornea and more sophisticated models are necessary when leaving the optical zone and moving to the outer periphery beyond the limbus. Furthermore Baker's equation is not sufficient for describing abnormally shaped corneas such as after corneal refractive surgery or keratoconus. However it is sufficient for describing normal corneas and is widely used by various eye models.

Several studies have measured the anterior radius of curvature, but there have been far fewer investigations of the posterior surface. Experimental distributions of the anterior vertex radii of curvature and asphericity coefficient are given in table 2.4.

As can be also seen there's a modification of cornea radius with age as Dubbelman et al.(2002) have calculate there's a loss of about 0.004 mm per year leading that young people have a flatten cornea than old people, as it has been confirmed by previous studies (Dunne et al., 1992).

The radius and the asphericity of the posterior part of the cornea are difficult to measure because of the influence of anterior surface shape on any measurement. But it was known that there is a high linear correlation between the anterior and posterior radii of curvature (Lowe and Clark, 1973; Dunne et al., 1992; Patel et al., 1993) and a reasonable fit of this relationship is $r_p = 0.81\, r_a$.

Even it is of lesser significance than the anterior surface shape because of the small refractive index difference across the posterior corneal boundary but the asphericity coefficient of the posterior cornea is not of negligible significance. Patel at al. (1993) are the first to estimate this shape factor.

The surface description as conicoid section is applicable to, both, the anterior and posterior corneal surface. Every surface of the cornea has its own refractive index, but since the stroma is the thickest layer, its refractive index dominates. The mean value of refractive index is usually taken as 1.376, and that of the aqueous humour, in contact with the back surface of the cornea, as 1.336.

So it is a reasonable approximation to describe the refraction process at the cornea as two refractions according to Snell's law: a first refraction at the anterior corneal surface and a second refraction at the posterior corneal surface, assuming a constant refraction index in between.

We can now find a mean value, which may change subject by subject and eye model by eye model, for the two surface powers. Using the formula founded in the previous paragraphs we can write:

anterior surface power: posterior surface power:

$$F_1 = 1000 \cdot \frac{1.376 - 1}{7.77} = +48.39\text{D} \qquad F_2 = 1000 \cdot \frac{1.336 - 1.376}{6.4} = -6.25\text{D} \qquad (2.120)$$

The power of the cornea as a whole is therefore about +42 D, over two-thirds of the total power of the eye.

Between the cornea and the next refractive layer there is the anterior chamber. It is filled with a colourless liquid called the aqueous humour since its water content is 98%. The depth of the anterior chamber measured along the eye's optical axis has an average value of about 3.0 mm.

From an optical point of view the depth of the anterior chamber is important as much as it affects the total power of the eye. If all other elements remained unchanged, a reduction of 1mm in the depth of the anterior chamber (through a forward shift of the crystalline lens) would increase the eye's total power by about 1.4D. The reverse effect would result from a shift in the opposite direction.

2.3.2. The Pupil

In human optics, the opening formed by the iris is known as the pupil. The size of the pupil controls the amount of light entering the eye. In normal conditions the pupils react to:

- a change in luminance, the 'direct' reflex
- a change in luminance applied to one eye only, also producing a 'consensual' reflex
- near fixation.

The pupil size decreases with age at an approximately uniform rate which does, however tend to slow down in later life. Largely because of differences in techniques of measurement, there is

only a limited measure of agreement between various published studies. The following diameters can be taken as typical. For the eye in total darkness, 7.6 mm at age 10, 6.2 mm at age 45 and 5.2mm at age 80. For the light-adapted eye, 4.8 mm at age 10, 4.0mm at age 45 and 3.4 mm at age 80 (Atchison and Smith, 2000).

2.3.3. Lens

The structure of the lens is shown in figure 2.17. The lens is an elastic capsule containing cellular tissue of non-uniform gradient index. This is difficult to measure and makes it difficult to deal with human lens parameters, especially for posterior surface of the lens that is difficult to image since it is seen through all the previous layers. The lens grows continually throughout life, with new epithelial cells forming at the equator, all the properties of the lens, are then age-dependent.

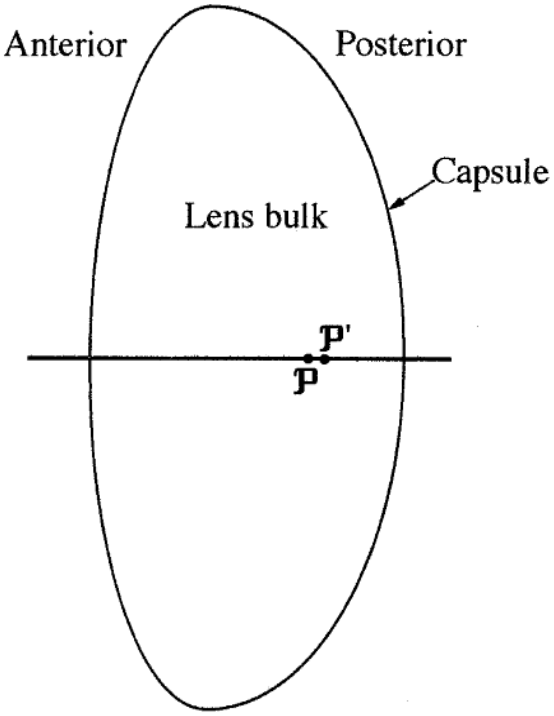

Figura 2.17 Lens (Atchison and Smith, 2000)

As first approximation of the lens surface it is described as aspheric curve. The first one to use sphere was Gullstrand (1909) in his well know model eye but from the first experimental data it was seen that an aspherical coefficient must be taken into account also for the optical zones of the lens that are about 5 mm diameter for anterior surface and 4 mm diameter for posterior surface.

It must be said that there are different methods to investigate the lens shape and we then refer to Appendix C. In table 2.5 experimental results of anterior lens radii and asphericity are given, it can be seen that even if there is a less variation for the radii, a bigger variation can be seen for the asphericity values, this happen due to the difficulties of the various techniques and inter-individual variations.

Tabella 2.5 Experimental results of anterior lens radii and asphericity

author	year	num. of eye (age ± SD)	method	anterior lens radius (mm) (val ± SD)	asphericity (val ± SD)
Lowe[1]	1972	92 (23 – 77)	in vivo	10.29 ± 1.78	—
Parker[1]	1972	100 (12– 91)	in vivo	5.0	–1.5
Lowe and Clark[1]	1973	92 (45)	in vivo	11.26	
Brown[1]	1974	200 (3 – 82)	in vitro	12.4 ± 2.6 (central) 13.3 ± 3.2 (peripheral)	—
Howcroft and Parker	1977	120 (52 ± 22)	in vitro	7.3 ± 0.3	–1.08 ± 9.41[2]
Pierscionek and Chan	1989	11 (57 ± 22)	in vitro	9.6 ± 0.9	3.5 ± 0.9
Glasser and Campbell	1999	13	in vitro	4.32 + 0.068 A	–1
Dubbelman et al.	2001	102	Slit lamp	12.9 ± 0.4 – (0.057 ± 0.009)A	–6.4 ± 1.6 + (0.03 ± 0.04)A[3]
Schachar	2004	30	in vitro	10.0 ± 0.5	—
Manns et al.	2004	24	in vitro	10.15 ± 1.39	–2.66 + 0.077A
Dubbelman et al. (Norrby)	2005	—	—	1 / [1 / (12.7 – 0.058A) + 0.0077D]	–5 + 0.5D
Jones et al.	2005	20	MRI	11.6 ± 4.8	—
Rosen et al.	2006	37	in vitro	7.5 + 0.046A	–0.8 ± 1.7
Rosales et al.	2006	46 (30 ± 9)	Purkinje	10.8 ± 1.1	—

[1]Data from Liou and Brennan (1997), [2]Data from Smith et al. (1991), [3]not significant regression (P = 0.44)

The first to evaluate the dependence of the anterior radius by age was Dubbelman (2001), and Norrby in 2005 add to Dubbelman model the dependence by accommodation.

In a relaxed state the thickness of the lens was usually taken as 3.6 mm but Dubbelman et al. (2001) using balanced Sheimpflug imaging calculate a value for the lens thickness (in mm) = 2.93 (±0.07) + 0.0236 (±0.002) x age ($r = 0.81$; $p < 0.0001$)

The crystalline lens serves the double purpose of supplying the balance of the eye's refractive power and providing a mechanism for focusing at different distances. This latter faculty is called accommodation. As accommodation is brought into play; both surfaces, but especially the anterior, assume a more steeply curved form. The centre thickness thus increases and the vertex of the anterior surface moves forward, reducing the depth of the anterior diameter.

The refractive index within the lens is not constant, being greatest in the centre and least in the periphery (Nakao et al., 1969; Pierscionek et al., 1988; Pierscionek and Chan. 1989; Pierscionek, 1995). In particular, it is possible to distinguish a central biconvex portion called the nucleus, in which the refractive index is almost constant and reaches its maximum value between 1.40 and 1.41 but diminishes from the centre outwards, being about 1.386 near the poles and about 1.375 near the equator. It may easily be deduced that a refractive index gradient of this pattern, irrespective of any surface curvatures, must produce a converging effect like a positive lens.

Light rays are therefore refracted by the anterior surface and the posterior surface just as at the

cornea. But in between they undergo a continuous refraction; that means their direction is not a straight line within the lens. This is comparable to gradient index (GRIN) lenses which have a continuous refractive index distribution. Computational ray tracing through gradient index media is more complex than for homogeneous refractive index media, because the classical Snell's law has to be generalized.

Tabella 2.6 Experimental results of posterior lens radii and asphericity

author	year	num. of eye (age ± SD)	method	posterior lens radius (mm) (val ± SD)	asphericity (val ± SD)
Parker[1]	1972	100 (12– 91)	in vivo	–3.3	–1.0
Brown[1]	1974	200 (3 – 82)	in vitro	–8.1 ± 1.6 (central) –7.1 ± 1.4 (peripheral)	—
Howcroft and Parker	1977	120 (52 ± 22)	in vitro	–5.4 ± 0.1	–0.12 ± 1.74[2]
Pierscionek and Chan	1989	11 (57 ± 22)	in vitro	–8.1 ± 0.5	2.1 ± 0.2
Glasser and Campbell	1999	19	in vitro	–3.143 – 0.0536A + 0.0004173A^2	–1
Dubbelman et al.	2001	42	Slit lamp	–(6.5 ± 0.3 – (0.017 ± 0.008)A)	–6 ± 2 + (0.07 ± 0.06)A[3]
Schachar	2004	30	in vitro	–6.8 ± 0.9	—
Manns et al.	2004	18	in vitro	–2.313 – 0.050A	–1.7 ± 1.8
Dubbelman et al.(Norrby)	2005	—	—	–1 / [1 / (5.9 – 0.0015A) + 0.0043D]	–4
Jones et al.	2005	20	MRI	–7.2 ± 2.1	—
Rosen et al.	2006	37	in vitro	–5.5	–1.1 ± 1.5
Rosales et al.	2006	46 (30 ± 9)	Purkinje	–6.7 ± 0.8	—

[1]Data from Liou and Brennan (1997), [2]Data from Smith et al. (1991), [3]not significant regression (P = 0.21)

A common technique used for fast evaluate the optical behaviour of the lens and to estimate the posterior lens surface is to substitute the GRIN of the lens with an homogeneous index that instead must be of an higher value often taken as 1.42 to bring the power of a homogeneous crystalline lens up to a typical value in the neighbourhood of +21 D.

It is on the other hand known that the refractive index of the lens change with age as well and in recent studies by Navarro et al. (2007) they found a relationship between an equivalent homogeneous refractive index with age:

$$n = -3 \cdot 10^{-7} \times age^2 - 2 \cdot 10^{-5} \times age + 1.423 . \qquad (2.121)$$

Any measurements of the lens in vivo (within the eye) depend upon knowing the value of all the optical parameters that precede the particular surface. This is a particular problem for the posterior surface because of the uncertainty of the refractive index distribution in any particular lens. In table 2.6 as for the other refractive layers are reported the curvature radius and asphericity

coefficient for the posterior lens surface in the optical zone of 5 mm diameter.

As we have said to describe the geometry of the lens the simplest method used to interpolate the data is to use aspherical curves, but different mathematical models were proposed and used for optical and biomechanical analysis.

The aspherical curve is convenient since it has only two coefficients that must be determined and it is closely linked to the optical properties of the lens e.g. the vertex radius power. On the other hand the coefficient q drives the spherical aberration that decreases as long as q decreases (Smith et al, 2009).

Although this function is very simple it has two problems: r and q depend on the central fitting area used in its determination and moreover if we consider two functions one for the anterior and one for the posterior part it is not possible to connect the two functions at the equator continuously.

To counter this problem the aspherical equation is usually modified adding figuring terms as stated out by Smith (2003) so that the equation becomes:

$$y^2 = 2rz - (1+q)z^2 + v_1 z^3 + v_2 z^4 + v_3 z^5 \qquad (2.122)$$

where terms r, q, v_1, v_2 and v_3 are found by numerical optimization.

The addition of extra figuring higher order terms (v_i coefficients) allows a smooth connection at the equator of the anterior and posterior part of the lens without any hard modification of r, and, moreover, the fit accuracy improves.

Another approach used by Hermans et al. (2009) and based on the works of Dubbleman and Van der Heijde (Dubbelman and Van der Heijde, 2001; Dubbelman et al., 2002; Hermans et al., 2007), is to use different conic patches for the different zones of the lens.

Their curve is a parametric curve with a set of parameters that have a physical meaning. Their model is formed by an anterior and posterior conic function of the form:

$$y^2 = 2r_a(t_a + z) \qquad (2.121a)$$

$$y^2 = 2r_p(t_p - z) \qquad (2.123b)$$

where the anterior part (3a) stops when y = 2.5 mm (the radius of anterior optical zone) and the posterior one (3b) when y = 2 mm (the radius of posterior optical zone). These functions are then linked together by other two conics for anterior and posterior part that join at the equator plane, and are of the form:

$$y = R_{eq} - \frac{cz^2}{1+\sqrt{1-kc^2z^2}} \qquad (2.124)$$

where R_{eq} is the equatorial radius of the lens, k = 1 + q is the asphericity coefficient and c is the curvature of the conicoid junction.

To assure a continuous junction and a continuous derivative between the different conic patches, it is provided a formula to find the terms c and k for anterior and posterior surface:

$$c = \frac{R_{eq} - y_p}{z_p\left[\frac{(R_{eq} - y_p)y_p}{r} + z_p\right]} \qquad (2.125)$$

$$k = \frac{z_p\left[\frac{2(R_{eq} - y_p)y_p}{r} + z_p\right]}{(R_{eq} - y_p)^2} \qquad (2.126)$$

where the terms (z_p, y_p) stands for the interception of the junction zones with the anterior or posterior optic zone.

Only few authors try to use different equations to describe both the anterior and posterior lens

surface by a unique function, such as Kasprzak (2000) hyperbolic cosine functions, Urs et al. (2009) 10th–order polynomials or Urs et al. (2010) 10th–order Fourier series. Kasprzak model is particularly interesting since it has a continuous curvature profile. This model uses a function to describe shape of the lens, given in polar coordinates (see figure 1):

$$\rho(\theta) = \rho_a(\theta) + \rho_p(\theta) - t/2 \qquad (2.127)$$

where $\rho(\theta)$ is the distance from the lens centre along the angle θ that varies from 0 to π. The function has anterior and posterior contribution given by:

$$\rho_a(\theta) = (a_a/2)\cdot[\cosh((\pi-\theta)b_a)-1]\cdot[1-\tanh(m(s_a-\theta))]+t/2 \qquad (2.126a)$$

$$\rho_p(\theta) = (a_p/2)\cdot[\cosh(\theta b_p)-1]\cdot[1+\tanh(m(s_p-\theta))]+t/2 \qquad (2.128b)$$

where a and b can be derived by the lens radius and thickness t and the hyperbolic tangent terms give an appropriate cut–off function that reduce the mutual influence of the anterior and posterior contribution (the subscripts a and p are respectively referring to the anterior and the posterior contribution). The coefficients m and s describe the slope and the shift of the hyperbolic tangent. Modifying the parameter of equations 2.126a and 2.126b many model proposed in the literature can be approximate.

This model is one of the first that is not entangled to the standard conic view, and it is also a continuous curvature model that is an advantage for biomechanical characterization, but Kasprzak never gave a method to evaluate the coefficients expect numerical one.

As for Kasprzak model the Urs one (2010) uses trigonometric functions instead of conics. The Fourier series in a general form is written as:

$$\rho(\theta) = \sum_{n=0}^{10}(b_n)\cos(n\theta) \qquad (2.129)$$

where the anterior thickness is found when $\theta = \pi$, the posterior thickness for $\theta = 0$ and the equator for $\theta = \pi/2$.

A remarkable difference between the Urs model and the Kasprzak one is that she was able to assess the b_n coefficients and create then an age-dependent model so that equation 6 becomes:

$$\rho(\theta) = \sum_{n=0}^{10}(A_{n1} + A_{n2}\times \text{age})\cos(n\theta) \qquad (2.130)$$

in table 2.7 are collected the results of Urs et al. experiment with the values of the A_n parameters.

Tabella 2.7 Fourier coefficients of the age-dependent Fourier model (Urs et al., 2010)

Parameter	A_{n1}	A_{n2}
A_0	2.6466	$812.11\cdot10^{-5}$
A_1	0.2246	$170.62\cdot10^{-5}$
A_2	– 0.97938	$-297.37\cdot10^{-5}$
A_3	0.010573	$-34.901\cdot10^{-5}$
A_4	0.37993	$-26.276\cdot10^{-5}$
A_5	– 0.032321	$1.6647\cdot10^{-5}$
A_6	– 0.16846	$69.192\cdot10^{-5}$
A_7	0.027934	$-9.5571\cdot10^{-5}$
A_8	0.066522	$-42.251\cdot10^{-5}$
A_9	– 0.014232	$1.7295\cdot10^{-5}$
A_{10}	– 0.021375	$18.638\cdot10^{-5}$

2.3.4. Retina

The retina is the light-sensitive part of the eye. It consists of several layers playing different roles. This layer contains two types of receptor cells: the rods and cones. The rods are highly sensitive low-level light detectors responsible for vision in mid-light. In contrast, the cones need higher light levels but enable higher spatial resolution and are responsible for fine and colour vision. Therefore there are three types of cones absorbing long (red), middle (green) and short (blue) wavelength light. It is at the fovea that the eye attains its maximum resolving power. When an object engages visual attention, the two eyes are instinctively turned so that the image lies on each fovea.

From an optical point of view the retina could be described as the screen on which the image is formed. It can be regarded as part of a concave spherical surface with a radius of curvature in the neighbourhood of -12 mm and an aspheric coefficient that depend eye model by eye model.

2.3.5. Image Formation

The image formation process of the human eye is comparable to a man-made optical camera: the entering light is refracted by the cornea, limited by the pupil, refracted by the lens and focused at the retina. The cornea has a much higher optical power than the lens. However the power of the cornea is constant, while the human lens can accommodate and its power is therefore adjustable. The size of the pupil is variable and responsible for the amount of light entering the eye.

2.4. Eye Models

There are various schematic eye models based on population mean values. Theirs aim are to quantify the optical, or mechanical properties of the human eye. The models can be divided into two groups: paraxial schematic eyes and finite schematic eyes.

The paraxial schematic eyes are simpler and are only accurate in the paraxial region; they may be used for simulating basic optical properties, and they are useful for the calculation of entrance and exit pupil.

The finite schematic eyes are often based on paraxial ones, but they are more complex; usually they differ from the others by introducing non-spherical refracting surfaces, gradient index lenses and the components may be aligned arbitrarily. They may be used for simulating more accurately human optics, but different models may be designed for different purpose.

Some eye models provide data for different levels of accommodation and some others include aging factors.

2.4.1. Optical Centration

In the schematic eye it is assumed that all the refracting surfaces are coaxial, the cornea and crystalline having a common optical axis. The optical centration of the typical human eye seems to be defective, the crystalline lens being usually decentred and tilted with respect to the cornea. For this reason the eye does not possess a true optical axis.

2.4.2. Entrance and exit pupils

The real pupil H is assumed to lie in the plane of the anterior pole of the crystalline lens (figure 2.18). If its centre at E_0, is regarded as an object for the cornea, it will give rise to a lightly magnified image with its centre at E. This image is called the ‘entrance pupil’. Taken as an object for

the crystalline lens, the pupil H will give rise to another image, the 'exit pupil', with its centre at E'.

On the basis of paraxial theory, it may be shown that the entrance pupil is situated about 3mm behind the anterior surface of the cornea and is about 13% larger than the real pupil. The exit pupil lies closely behind the real pupil and is only 3% larger. (Atchison and Smith, 2000)

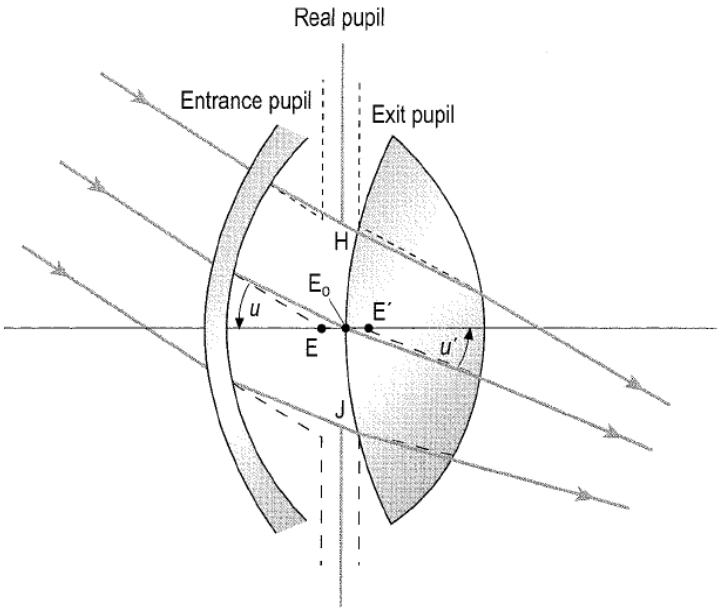

Figura 2.18 The eye's real pupil and its images, the entrance and exit pupil (Atchison and Smith, 2000)

2.4.3. The visual axis

It might be reasonable to expect that the fovea would be situated on the retina at its intersection with the optical axis. In fact, the fovea is normally displaced temporally and downwards from the expected position. We are therefore led to postulate a 'visual axis' as distinct from the optical axis. The visual axis has been taken by many writers to be the imaginary line directed towards the first nodal point E such that a parallel line through E' would pass through the fovea. Apart from a slight displacement due to the separation of the two nodal points, as seen in figure 2.19, an incident ray travelling along this path would be otherwise undeviated.

The angle between the optical and visual axis has a commonly accepted value in the neighbourhood of 5°.

The majority of eye models tend to unify the optical axis and the visual axis into one single axis, only few authors have taken into account this displacement, e.g. Liou and Brennan, 1997.

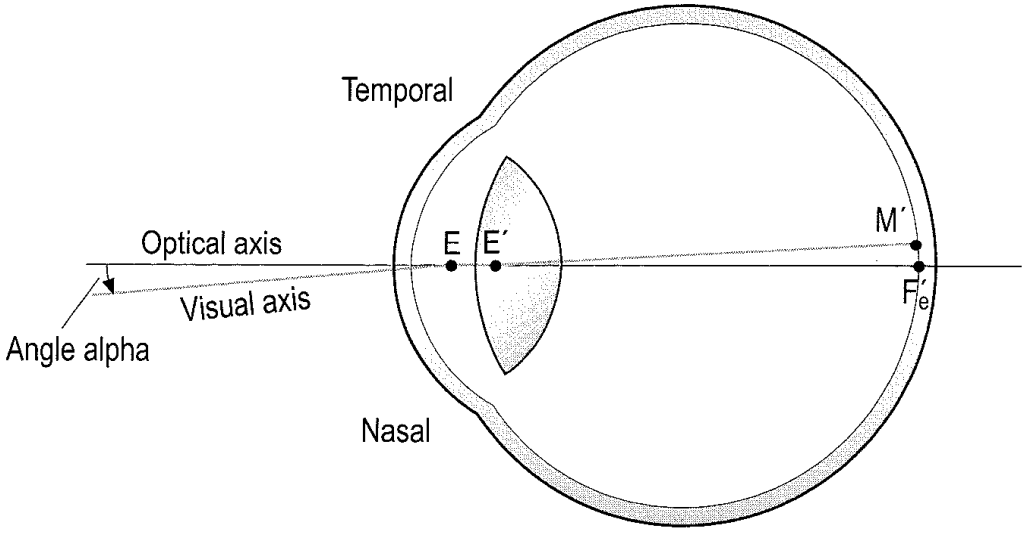

Figura 2.19 The optical and visual axes of the eye. Its second principal focus F'_e is shown. (Atchison and Smith, 2000)

2.4.4. Paraxial Eye Models

The first eye model was presented 1909 by Gullstrand (Helmholtz, Gullstrand et al. 1909). The exact-schematic eye consists of six spherical surfaces: two for the anterior and posterior cornea; four surfaces are used to model the gradient refractive index of the lens in which the inner shell (nucleus) had higher refractive index and more curved surfaces than the outer shell (cortex). The simplified schematic eye uses only three surfaces: one for the cornea and two for the anterior and posterior lens surface. Both models are at two levels of` accommodation (relaxed and maximal).

Similar to Gullstrand's model eye is the Le Grand full theoretical eye and Le Grand simplified eye (Le Grand and El Hage 1980). The full theoretical eye only has one refractive index and two surfaces for the lens (provided in relaxed and accommodated forms) and the simplified version uses a lens of zero thickness.

Emsley modified Gullstrand's simplified schematic eye for easier calculation purposes and introduced the Emsley standard reduced 60-diopter eye (Emsley 1952). His model consists of only one refracting surface.

Lately Rabbetts and Bennett introduced further data for accommodation levels and age levels (Rabbetts and Bennett 1998), and Blaker introduced a variable accommodative schematic eye together with age levels (Blaker 1980).

2.4.5. Finite Eye Models

Several finite or wide angles, eye models designs have been proposed and can offer good predictions for both on- and off-axis aberrations.

Lotmar's eye model is based on Le Grand full theoretical eye. He replaced the anterior corneal spherical surface by a polynomial representation and replaced the posterior lens surface by a paraboloid (Lotmar 1971).

Drasdo and Fowler's eye model is based on the Gullstrand-Emsley simplified eye. They add asphericity to the corneal surface and they change the planar retina by a sphere (Drasdo and Fowler 1974). Their purpose was to determine the retinal projection from the visual field.

Pomerantzeff et al. (Pomerantzeff et al. 1971), used a series of shells to model the gradient

refractive index of the lens, and both Al-Ahdali and El-Messiery (1995), who incorporated 300 such shells, and Liu et al. (Liu et al., 2005) who used 602, have extended this tactic.

Kooijman eye model was introduced to predict retinal illumination. All four refractive surfaces, two for the cornea and two for the lens, are aspherical. The retina is either spherical or aspherical (Kooijman 1983).

Navarro et al. provided a model also based on Le Grand full theoretical eye by refining it with asphericities. They also modelled the accommodation of the eye (Navarro et al. 1985).

Thibos et al. (1992), in opposite trend, proposed a single aspheric surface eye model that accurately predicted both the spherical and chromatic aberrations of the eye. The chromatic eye is not rotationally symmetric (Thibos et al. 1992), while their Indiana eye is rotationally symmetric (Thibos et al. 1997).

The advent of ray tracing capability through gradient index media (Sharma et al. 1982) has led to shell structured lenses being replaced by gradient refractive indices bounded by two aspheric surfaces.

Liou and Brennan model their eye with aspheric surfaces for both cornea and lens and include a gradient index lens. The specification of different axes leads to a non-rotationally symmetric model that let the model to resemble the anatomy of real eyes. No accommodation is modelled and age related parameters are assumed to be from a 45 year old person. Their aim is to correctly model the spherical and chromatic aberration of real eyes (Liou and Brennan 1997).

Popiolek-Masaqada et al. designed a schematic eye using four refracting surfaces and an alternative description of the lens profile with a combination of hyperbolic cosine functions and hyperbolic tangent functions (Popiolek-Masajada and Kasprzak 1999). The parameters of the lens are varied by the level of accommodation. The authors extended their model eye by using an accommodation dependent gradient refractive index (Popiolek-Masajada and Kasprzak 2002).

Siedlecki et al. (2004) proposed a model eye with aspherical surfaces like in Kooijman model adding a radially varying refractive index distribution of the crystalline lens. Their purpose was to analyse the spherical aberration.

Norrby took up the extensive analysis of the shape of real eyes of Dubbelman et al. to construct the Dubbelman eye model. It uses aspherical surfaces and it is rotationally symmetric. Similar to Navarro's eye model it uses a functional dependency of the lens parameters from accommodation level and age (Norrby, 2005).

From previous schematic eye and Dubbelman's data, Atchison proposed a refractive dependent model with aspherical surfaces and gradient index distribution of the crystalline lens (mean age is 25 year old). He also offers description of the chromatic dispersion of the index media of the eye model (Atchison 2005).

Goncharov and Dainty (2007) incorporated a mathematical representation of a gradient-index lens and were able to reproduce the properties of two well-known schematic eye models, namely Navarro's model for off-axis aberrations and Thibos's chromatic on-axis model.

We present a comprehensive table of the schematic eye, known by the author, ordered by year. We also tick the different characteristics of the models.

Our purpose in the present work is to analyse some selected schematic eye models. We would like to show how is possible to revise the common on-axis and off-axis properties by fundamental optical equations.

We also present a novel interpretation of gradient index lenses used in the more recent models by refraction surfaces.

Table 2.8 History of the schematic eye models

author	year	spheric surface	aspheric surface	GRIN lens	on-axis aberration	off-axis aberration	chromatic dispertion	age dependent	accomo-dation	ametropy dependent
Gullstrand	1909	6	—	—	✓	—	—	—	✓	—
Emsley	1952	1	—	—	✓	—	—	—	—	—
Lotmar	1971	3	1	—	✓	✓	—	—	—	—
Drasdo	1974	—	4	—	✓	✓	—	—	—	—
Pomerantzeff	1983	—	2	shell	✓	✓	—	—	—	—
Kooijman	1983	—	4	✓	✓	✓	—	—	—	—
Navarro	1985	1	3	—	✓	✓	✓	—	✓	—
Indiana (Thibos)	1992	—	1	—	✓	✓	✓	—	—	—
Liou and Brennan	1997	—	2	✓	✓	✓	✓	—	—	—
Popiolek-Masajada and Kasprzak	2002	2	2	✓	—	—	—	—	✓	—
Siedlecki	2004	—	4	✓	✓	✓	—	—	—	—
Liu	2005	—	4	shell	✓	—	—	—	—	—
Dubbleman (Norrby)	2005	—	4	—	✓	✓	—	✓	✓	—
Atchison	2006	—	2	✓	✓	✓	✓	—	—	✓
Goncharov	2007	—	2	✓	✓	✓	—	—	—	—

2.5. CAD and free-form eye model

In the mid—1960s Coons (1963, 1965), at MIT, and Ferguson (1964) at Boeing began important work in non rational free-form curves and sculptured surfaces, using the cubic Hermite interpolation scheme. Coons' pioneering work was also important because it stimulated the development of other curve and surface representations. The early efforts of de Casteljau (1959, 1963) were quickly followed by the independent and insightful work of Bézier (1966, 1967, 1968),

who produced a widely used method for curve and surface design.

These authors are the first to study both in university (MIT) and industry (Boeing, Citroen, Renault) the different possibilities that the computer aided design, CAD, gives in engineering modeling.

From this first studies in 2D representation are developed different mathematical representations also for 3D modeling: constructive solid geometry, CSG; and boundary representation, B-rep.

CSG representation is based on Boolean combination of basis 3D objects, e.g. cubes, sphere, cylinder.

B-rep on the other hand describes the boundary surfaces of the 3D object and gives topological rules to link together these objects.

Different CADs uses different representations to modelise the 3D object even if nowadays the differences between commercial programs are not so huge.

The key point we want to underline here is that for designing an eye model the best way is to describe the refractive surfaces of the eye, so the cornea and the lens, and the eye ball, retina and sclera. Let now introduce which are the element used for modelise a surface into a CAD.

2.5.1. Points, Nurbs and Mesh

The easiest way to define a surface into a CAD is to use a collection of points, usually called cloud of points. This is a quantization of the real surface but it does not give any kind of information about the surface itself, for example which is the inside part and the outside since no orientation is given. Cloud of points is an easy way to store and share data from one program to another one, in fact is usually the output of some imaging tools, so it can be imported into a CAD.

In figure 2.20 can be seen a cornea surface acquired as a cloud of points by a topographer and then imported into a CAD (Rhinoceros by McNeel & Associates).

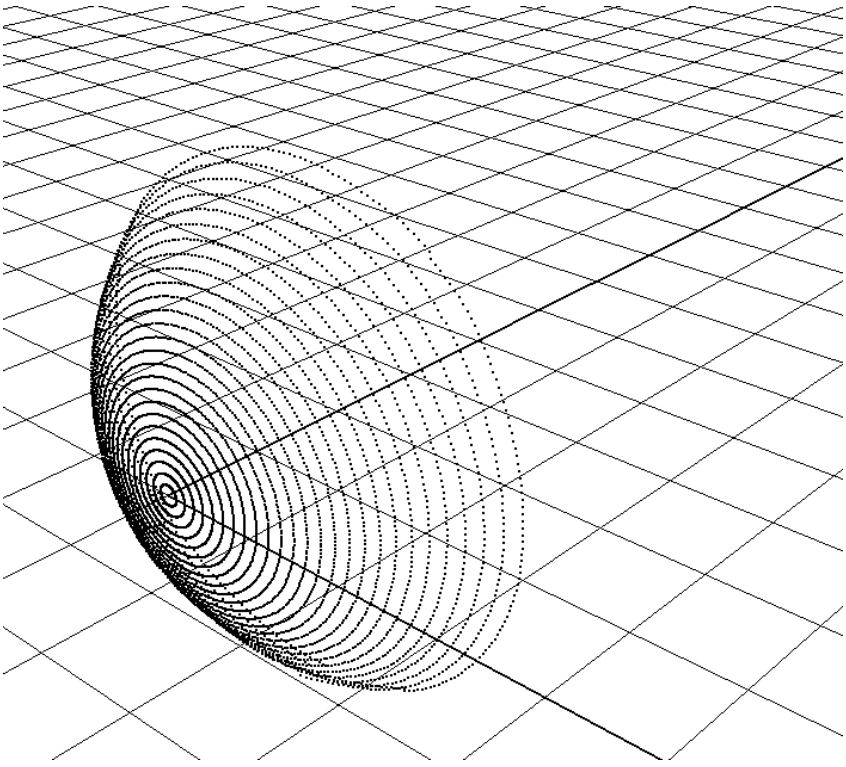

Figura 2.20 Output data of a topographer imported into a CAD as a cloud of points

NURBS curves and surfaces are the most general type of parametric surfaces a CAD is able to manage. Its name stands for Non Uniform Rational B-Splines and every kind of surface into a CAD, also conicoids, is modelised as a NURBS. Their general form is:

$$S(u,v) = \frac{\sum_i \sum_j N_i(u) N_j(v) w_{i,j} P_{i,j}}{\sum_i \sum_j N_i(u) N_j(v) w_{i,j}} \qquad (2.131)$$

where N_i and N_j are the basis function in the parameters u and v, $w_{i,j}$ is the weight, and $P_{i,j}$ are the control points of the NURBS surface. By modifying the control points the surface will be locally modified as well.

A NURBS surface can be used to modelise a conicoid defined by its analytical formulation, or to fit a cloud of point. Rather then cloud of points a NURBS surface be evaluated to find its normals and curvature.

In figure 2.21 the cloud of points of figure 2.19 was fitted by a NURBS, and control points of the surface are shown.

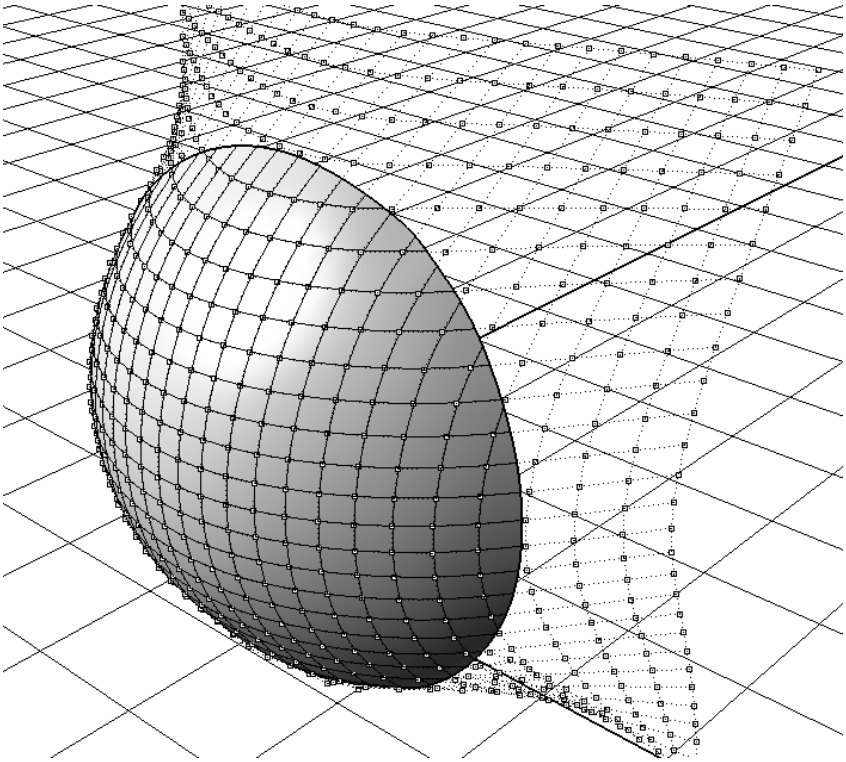

Figura 2.21 Output data of a topographer imported into a CAD as a NURBS

A polygon mesh or unstructured grid is a collection of vertices, edges and faces. The faces usually consist of triangles, quadrilaterals or other simple convex polygons, since this simplifies rendering. Usually along this collection of polygons is also given a topology of the mesh so it is easy to move from vertices to vertices or from face to face, and this speed up the calculus of mesh surface characteristics that cannot be immediately evaluated as NURBS surfaces.

A mesh surface such a NURBS surface can be used to modelise a conicoid defined by its analytical formulation, or to fit a cloud of point. In figure 2.22 the clouds of points of figure 2.21 was fitted by a mesh.

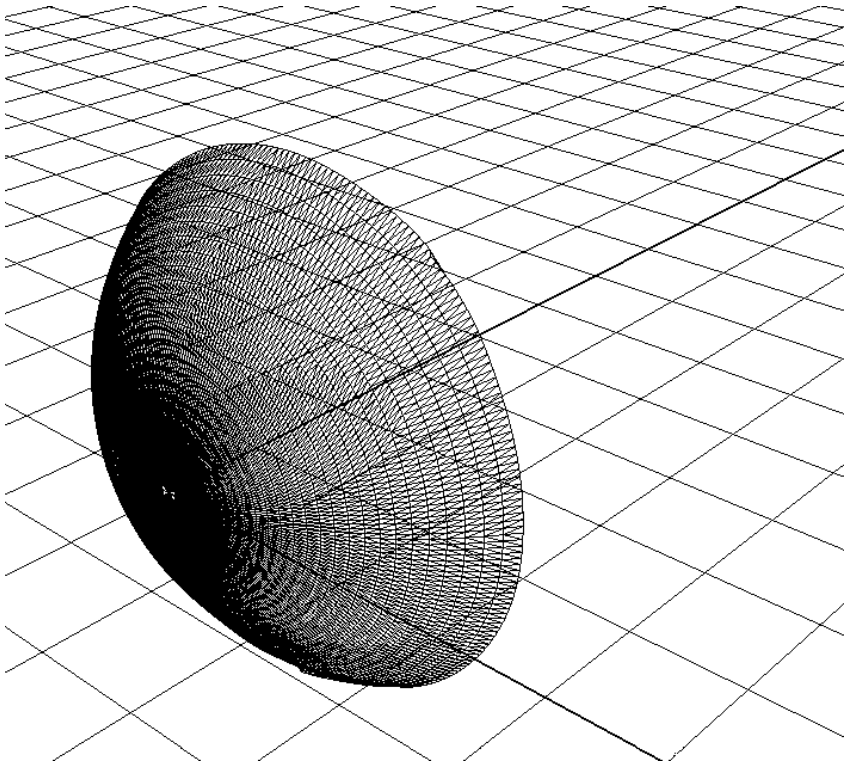

Figura 2.22 Output data of a topographer imported into a CAD as a mesh

2.5.2. 3D eye model

The eye models presented in paragraph 2.4 which are the most known in the literature are usually presented as 2D models. The 3D representation of these eye models is a simple rotation along the z-axis of the 2D profile. This for sure is a simplification of a real eye since the known toricity is not taken into account, but this permit to simplify both the modelisation and the analysis of the eye models. Commercial programs usually used for optical analysis are explicitly created for optical systems that use conics as refractive or reflective surfaces so the 2D representation of eye models can be simply used by these programs to analyse eye models.

Only few authors in their Ph.D. thesis (Einighammer, 2008; Tan, 2009) starts to use different surfaces in such a 3D representation, and they underline the need of more complex representation of eye models.

On the other hand in the last years many imaging systems are able to create 3D topographical image of corneal surface, new methods for imaging the crystalline lens are now available, e.g. MRI, and are able to create 3D image of the lens, but the image created by the software are usually not integrated into a CAD, but remain printed on a paper, or fitted by simple conics surfaces.

For the best of our knowledge no CAD integrated any plug-in that is able to import, modify and analyse, for example with ray-tracing technique, the output of these imaging tools, and for sure this is a gap that must be filled.

2.5.3. Finite element analysis

Beside the CAD representation another well known method to analyse 3D eye models is the finite element analysis, FEM.

From the enlightening Ph.D. thesis of Le (2005) some authors (Schachar et al., 2006a; Schachar et al., 2006b; Hermans et al., 2006; Liu et al., 2006) analyse the accommodation of the crystalline

lens with FEM method. The mathematical models used to create the lens in a 3D environment are Hermans et al. (2006) model (figure 2.23) refined later in 2009, or Chien et al. (2003) model.

These models have different curvature characteristics that will be explained in chapter 4, where a method to find Chien et al. coefficients is proposed. FEM analysis is for sure a new interesting method to investigate accommodation and its dependence by age, and can be useful to understand also the mechanic of the crystalline lens that is for sure the most difficult surface of the eye to be modelised.

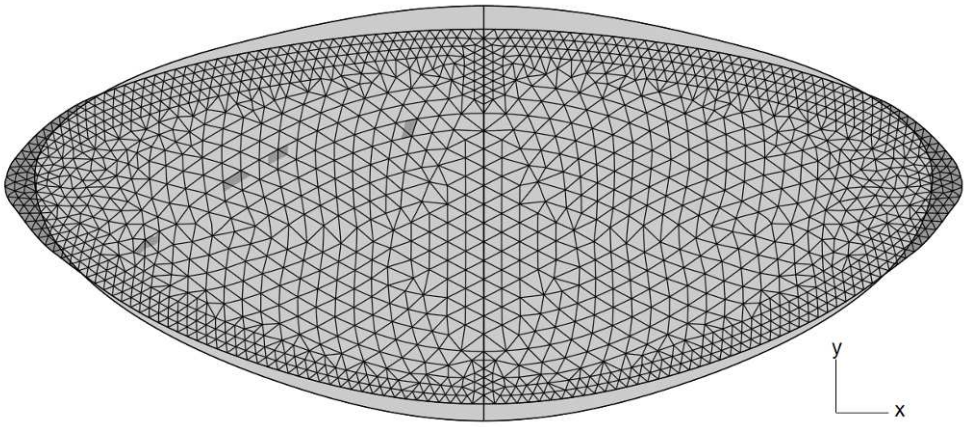

Figura 2.23 FEM model of the crystalline lens (Hermans et al., 2006)

Chapter 3. Virtual eye analysis: tools development

In this chapter we would like to introduce the tools developed for the surface analysis. In the first part we show a new method for curvature analysis of optical surfaces. The difference with existing methods is that the curvature calculus is done upon a surface patch that can be linked with entrance pupil dimension, or to the spot of optical analysis instruments.

In the second part we extend the ray trace of one single ray that was already shown in the first chapter in a 3D environment.

The CAD used for the analysis (Rhinoceros by McNeel & Associated) will be a useful environment not only for ray trace but also for modeling eye models and test contact or spectacle lenses as we will see better in the next chapter.

3.1. Curvature analysis for optical measurements

The primary method for ophthalmic lenses manufacturing is based on the production of a semi-finished lens blanks, where only one surface of the lens is completed, while the other surface must be machined in an ophthalmic prescription laboratory. At present the ISO standards (ISO 10322-1:2006 and ISO 10322-2:2006) define a testing method for power, astigmatism and addition of a single lens surface using a focimeter that measures the optical properties by light transmission.

The measures performed using these methods are affected also by the opposite non-finished surface characteristics/defects, as surface imperfections (as e.g. grooves, scratches, cracks, pores, blowholes, etc.) and macro/micro-geometry errors. Moreover, these measures depend on the semi-finished spectacle lens blank thickness and have been derived by the concave spherical curve, back vertex power and thickness measurements.

To overcome these limitations, the assessment of optical properties of a single surface could be performed adopting methods based on curvature estimation of a discrete geometrical model (i.e. mesh or cloud of points) derived from a physical model or directly generated in a virtual environment.

We first present two fitting methods, one for estimate the curvature of a curve in the plane and one to estimate the curvature of a surface in the space. Then a method based on second order polynomial fitting for estimating optical properties by curvature computation of ophthalmic surfaces (e.g. lenses) is here presented.

3.1.1. Curve curvature estimation method

A collection of points in the plane can be approximated by a circle. A circular fitting may be important if the curve is related with optical properties, since is immediate to find the radius of curvature of the fitting circle.

In the plane a circle can be expressed in implicit form as:

$$x^2 + y^2 + ax + by + c = 0\,. \qquad (3.1)$$

The sum of the squares of the distances between the points and the circle is expressed by the following equation:

$$\sum_i d_i^2 = \sum_i \left(x_i^{\,2} + y_i^{\,2} + ax_i + by_i + c\right)^2 \qquad (3.2)$$

and to apply the least square method is necessary to minimize this sum so that the derivative of the previous equation on the coefficients a, b and c is equal to zero. It means solving the 3-equation problem:

$$\frac{\partial \sum_i d_i^2}{\partial p} = 0 \qquad p = a,b,c \qquad (3.3)$$

equivalent to the linear system:

$$\begin{bmatrix} a \\ b \\ c \end{bmatrix} = \begin{bmatrix} \sum_{i=1}^{n} x_i^{\,2} & \sum_{i=1}^{n} x_i y_i & \sum_{i=1}^{n} x_i \\ \sum_{i=1}^{n} x_i y_i & \sum_{i=1}^{n} y_i^{\,2} & \sum_{i=1}^{n} y_i \\ \sum_{i=1}^{n} x_i & \sum_{i=1}^{n} y_i & n \end{bmatrix}^{-1} \begin{bmatrix} -\sum_{i=1}^{n} x_i^{\,3} - \sum_{i=1}^{n} x_i y_i^{\,2} \\ -\sum_{i=1}^{n} y_i^{\,2} - \sum_{i=1}^{n} x_i^{\,2} y_i \\ -\sum_{i=1}^{n} x_i^{\,2} - \sum_{i=1}^{n} y_i^{\,2} \end{bmatrix} \qquad (3.4)$$

where the summatory is calculated between 1 and n where n is the number of points considered for the least square method, of course to solve the system the minimum number of points should be three.

Once the coefficients a, b and c are founded for a set of point (x_i, y_i) is easy to find the radius of curvature r_i from the known formula:

$$r = \sqrt{\left(\frac{a}{2}\right)^2 + \left(\frac{b}{2}\right)^2 - c}\,. \qquad (3.5)$$

3.1.2. Surface curvature estimation method

A cloud of points in the space can be approximated by a quadric function fitting. The fitting technique used for creating the explicit quadratic function

$$f(u,v) = p_1 u^2 + p_2 v^2 + p_3 uv + p_4 u + p_5 v + p_6 \qquad (3.6)$$

is based on the least square method that minimizes the sum of the squares of the vertical deviations between the points (zi) and the surface f (u, v):

$$\sum_i d_i^2 = \sum_i \left(z_i - f(u_i, v_i)\right)^2 \qquad (3.7)$$

Subsequently, to obtain the coefficient p_j (j=1, 2, …, 6), the derivates of $\sum_i d_i^2$ function according to the p_j coefficients should be set equal to zero. It means solving the 6-equation problem:

$$\frac{\partial \sum_i d_i^2}{\partial p_j} = 0 \qquad j = 1,2,\ldots,6 \qquad (3.8)$$

equivalent to the linear system:

$$\begin{bmatrix} p_1 \\ p_2 \\ p_3 \\ p_4 \\ p_5 \\ p_6 \end{bmatrix} = \begin{bmatrix} \sum_{i=1}^{n} u_i^4 & \sum_{i=1}^{n} u_i^2 v_i^2 & \sum_{i=1}^{n} u_i^3 v_i & \sum_{i=1}^{n} u_i^3 & \sum_{i=1}^{n} u_i^2 v_i & \sum_{i=1}^{n} u_i^2 \\ \sum_{i=1}^{n} u_i^2 v_i^2 & \sum_{i=1}^{n} v_i^4 & \sum_{i=1}^{n} u_i v_i^3 & \sum_{i=1}^{n} u_i v_i^2 & \sum_{i=1}^{n} v_i^3 & \sum_{i=1}^{n} v_i^2 \\ \sum_{i=1}^{n} u_i^3 v_i & \sum_{i=1}^{n} u_i v_i^3 & \sum_{i=1}^{n} u_i^2 v_i^2 & \sum_{i=1}^{n} u_i^2 v_i & \sum_{i=1}^{n} u_i v_i^2 & \sum_{i=1}^{n} u_i v_i \\ \sum_{i=1}^{n} u_i^3 & \sum_{i=1}^{n} u_i v_i^2 & \sum_{i=1}^{n} u_i^2 v_i & \sum_{i=1}^{n} u_i^2 & \sum_{i=1}^{n} u_i v_i & \sum_{i=1}^{n} u_i \\ \sum_{i=1}^{n} u_i^2 v_i & \sum_{i=1}^{n} v_i^3 & \sum_{i=1}^{n} u_i v_i^2 & \sum_{i=1}^{n} u_i v_i & \sum_{i=1}^{n} v_i^2 & \sum_{i=1}^{n} v_i \\ \sum_{i=1}^{n} u_i^2 & \sum_{i=1}^{n} v_i^2 & \sum_{i=1}^{n} u_i \cdot v_i & \sum_{i=1}^{n} u_i & \sum_{i=1}^{n} v_i & n \end{bmatrix}^{-1} \begin{bmatrix} \sum_{i=1}^{n} u_i^2 z_i \\ \sum_{i=1}^{n} v_i^2 z_i \\ \sum_{i=1}^{n} u_i v_i z_i \\ \sum_{i=1}^{n} u_i z_i \\ \sum_{i=1}^{n} v_i z_i \\ \sum_{i=1}^{n} z_i \end{bmatrix} \quad (3.9)$$

where the summatory is calculated between 1 and n where n is the number of points considered for the least square method, of course to solve the system the minimum number of points should be six.

3.1.2.1. Maximum, Minimum, Mean and Gaussian Curvature for a Second Order Polynomial in Explicit Form in the Origin

A surface defined by an explicit quadratic function (3.6) can be expressed as a parametric surface S = (u, v, f(u,v)). Consequently the partial derivatives of S with respect to u and v, the normal vector, and the relative derivates to the surface can be expressed by:

$$S_u = \begin{bmatrix} 1 \\ 0 \\ 2p_1 u + p_3 v + p_4 \end{bmatrix} = \begin{bmatrix} 1 \\ 0 \\ l \end{bmatrix} \quad (3.10a)$$

$$S_v = \begin{bmatrix} 0 \\ 1 \\ 2p_2 v + p_3 u + p_5 \end{bmatrix} = \begin{bmatrix} 0 \\ 1 \\ m \end{bmatrix} \quad (3.10b)$$

and the normal to the surface:

$$\perp = \frac{1}{\sqrt{l^2 + m^2 + 1}} \cdot \begin{bmatrix} l \\ m \\ 1 \end{bmatrix} \quad (3.11)$$

and deriving again:

$$\perp_u = \frac{1}{\left(l^2 + m^2 + 1\right)^{3/2}} \cdot \begin{bmatrix} 2p_1\left(l^2 + m^2 + 1\right) - l \cdot \left(m \cdot p_3 + 2l \cdot p_1\right) \\ p_3\left(l^2 + m^2 + 1\right) - m \cdot \left(m \cdot p_3 + 2l \cdot p_1\right) \\ m \cdot p_3 + 2l \cdot p \end{bmatrix} \quad (3.12a)$$

$$\perp_v = \frac{1}{\left(l^2 + m^2 + 1\right)^{3/2}} \cdot \begin{bmatrix} p_3\left(l^2 + m^2 + 1\right) - l \cdot \left(2m \cdot p_2 + l \cdot p_3\right) \\ 2p_2\left(l^2 + m^2 + 1\right) - m \cdot \left(2m \cdot p_2 + l \cdot p_3\right) \\ 2m \cdot p_2 + l \cdot p_3 \end{bmatrix} \quad (3.12b)$$

If we consider calculating the curvature only at the centre of the quadric surface for every point z_i we can simplify the previous formulas obtaining:

$$S_u = \begin{bmatrix} 1 \\ 0 \\ p_4 \end{bmatrix} \qquad (3.13a)$$

$$S_v = \begin{bmatrix} 0 \\ 1 \\ p_5 \end{bmatrix} \qquad (3.13b)$$

$$\perp_u = \frac{1}{\left(p_4^2 + p_5^2 + 1\right)^{3/2}} \cdot \begin{bmatrix} 2p_1p_5^2 + 2p_1 - p_3p_4p_5 \\ p_3p_4^2 + p_3 - 2p_1p_4p_5 \\ 2p_1p_4 + p_3p_5 \end{bmatrix} \qquad (3.13c)$$

$$\perp_v = \frac{1}{\left(p_4^2 + p_5^2 + 1\right)^{3/2}} \cdot \begin{bmatrix} p_3p_5^2 + p_3 - 2p_2p_4p_5 \\ 2p_2p_4^2 + 2p_2 - p_3p_4p_5 \\ 2p_2p_5 + p_3p_4 \end{bmatrix}. \qquad (3.13d)$$

Computating k_M and k_G for the centre of the quadric surface we obtain these functions:

$$k_G = \frac{4p_1p_2 - p_3^2}{\left(p_4^2 + p_5^2 + 1\right)^2} \qquad k_M = \frac{p_1\left(p_5^2 + 1\right) + p_2\left(p_4^2 + 1\right) - p_3p_4p_5}{\left(p_4^2 + p_5^2 + 1\right)^{3/2}} \qquad (3.14)$$

Moreover, remembering that the principal curvatures k_1, k_2 and the relative difference k_D, can be computed from mean and Gaussian curvatures (eq. 13-14), for quadratic surface results:

$$k_1, k_2 = \frac{p_1\left(p_5^2 + 1\right) + p_2\left(p_4^2 + 1\right) - p_3p_4p_5 \pm \sqrt{\left[p_1\left(p_5^2 + 1\right) + p_2\left(p_4^2 + 1\right) - p_3p_4p_5\right]^2 + \left(p_3^2 - 4p_1p_2\right)\left(p_4^2 + p_5^2 + 1\right)}}{\left(p_4^2 + p_5^2 + 1\right)^{3/2}} \qquad (3.15)$$

But we can find also some interesting relationship if we consider a local parameterization centred on z_i so that p_4 and p_5 are equal to zero, then:

$$k_1, k_2 = \pm\sqrt{\left(p_1 - p_2\right)^2 + p_3^{\,2}} - p_1 - p_2 \qquad (3.16)$$

and if also p3 is equal to zero so it means that we are fitting with a paraboloid with u and v along x- and y-axis which explicit formula is:

$$f(x,y) = p_1x^2 + p_2y^2 \qquad (3.17)$$

we find that the principal curvatures are as expected:

$$k_1 = -2p_1 \qquad k_2 = -2p_2 \qquad (3.18)$$

3.1.2.2. Principal Curvature Directions for a Second Order Polynomial in Explicit Form in the Origin

Beside principal directions k_1 and k_2 we can also find their directions. According to Mortenson (2006) we can write the equation

$$(FN - GM)\cdot l^2 + (EN - GL)\cdot l + EM - FL = 0 \qquad (3.19)$$

where l = dw /du is the principal direction. One of the roots of this equation makes the normal curvature maximum, and the other makes it a minimum. At an ordinary point on a surface (not a plane or a sphere) there is only one direction for which the curvature is a maximum or a minimum.

As we have done for principal curvatures we can explicit the previous formula for a quadric surface computating the principal directions in the centre of the paraboloid:

$$l_1, l_2 = \frac{p_2\left(p_4^2 + 1\right) - p_1\left(p_5^2 + 1\right) \pm \sqrt{\left[p_2\left(p_4^2 + 1\right) - p_1\left(p_5^2 + 1\right)\right]^2 + \left(p_3\left(p_5^2 + 1\right) - 2p_2p_4p_5\right)\left(p_3\left(p_4^2 + 1\right) - 2p_1p_4p_5\right)}}{\left(p_3\left(p_5^2 + 1\right) - 2p_2p_4p_5\right)}$$

(3.20)

Again putting p_4 and p_5 are equal to zero as for we consider that paraboloid centred in the point zi we can simplify the above relationship as:

$$l_1, l_2 = \frac{p_2 - p_1 \pm \sqrt{(p_2 - p_1)^2 + p_3^2}}{p_3} \qquad (3.21)$$

and if also p_3 is equal to zero so it means that we are fitting with a paraboloid with u and v along x- and y-axis we find that the principal curvature directions formula become of the first order so we find that:

$$(p_1 - p_2) \cdot l = 0 \qquad (3.22)$$

Since we want to consider the angle between the x-axis and principal directions we can define:

$$\varphi = \arctan(l) \qquad (3.23)$$

and since the principal directions are orthogonal each other we can finally write:

$$\varphi_1 = 0 \qquad \varphi_2 = \pi/2\,. \qquad (3.24)$$

For umbilical points instead we find that all directions are principal directions.

3.1.3. Surface power of ophthalmic lenses

The spectacle lenses vocabulary is defined in the ISO 13666:1998 standard. More precisely an ophthalmic lens is a “lens intended to be used for purposes of measurement, correction and/or protection of the eye, or for changing its appearance”; a spectacle lens is an “ophthalmic lens worn in front of, but not in contact with, the eyeball”; the surface power is defined as the “ability of a surface (or part of a surface) to change the vergence of a bundle of rays incident in air at the surface”; the principal meridians of a surface are “those meridians of a surface which show the maximum and minimum curvatures on measurement”; the surface astigmatic power is the “difference between the surface powers in the principal meridians of a finished surface”; the refractive index is the “ratio of the speed of electromagnetic radiation in vacuum to the phase speed of monochromatic radiation of wavelength λ in the medium”.

The surface power along any meridian is correlated to the curvature by the refractive index n of the lens:

$$F = (n-1) \cdot k \qquad (3.25)$$

The definition of principal meridian of a surface is equivalent to that of principal direction, and consequently, the surface power of the principal meridians F_1 and F_2 can be derived by means of the principal curvatures:

$$F_1 = (n-1) \cdot k_1, \qquad (3.26a)$$

$$F_2 = (n-1) \cdot k_2 \qquad (3.26b)$$

According to the ISO 10322-1:2006 and ISO 10322-2:2006 standards, the tolerances used in the quality assessment, are applied to the mean surface power F_M and to the surface astigmatic power A:

$$F_M = \frac{F_1 + F_2}{2} = (n-1) \cdot \frac{k_1 + k_2}{2} = (n-1)k_M \qquad (3.27)$$

$$A = |F_1 - F_2| = (n-1) \cdot (k_1 - k_2) = (n-1) \cdot k_D\,. \qquad (3.28)$$

Moreover, the mean surface power and the astigmatic surface power, defined as a function of curvature and refractive index, can be applied to the progressive lens design as demonstrated by Loos et al. (1998) and Wang et al. (2003, 2004).

In ophthalmic optics, the measured power is the back vertex power F_{bv} and can be estimated, by the following relationship (Jalie, 2003):

$$F_{bv} = \frac{F_f}{\left(1 - \frac{t}{n} F_f\right)} + F_b \qquad (3.29)$$

where F_f and F_b are the convex surface power and concave surface power respectively and t is the lens thickness. Hence, starting from the surface power of the front and of the back surface, the lens back vertex power can be estimated.

3.1.4. Errors in curvatures and optical properties estimation

In order to estimate the error in curvature calculation, different test cases have been identified varying the following parameters: surface step sampling (ss), φ_1, φ_2, k_1, k_2 and lpss. Analyzing the test cases an error model can be derived as a function of the cited parameters.

Consequently, the error in the surface power and in the astigmatic surface power can be defined by the error propagation relationships (ISO/IEC Guide 98-3:2008). In this condition, given the function $f=f(x_1,x_2, \ldots, x_n)$, if the variables $x_1, x_2, \ldots, x_n$ are uncorrelated, the relative error εf and the absolute error Δf on f(x1,x2, …, xn) can be estimated as:

$$\varepsilon f = \left|\frac{\partial f}{\partial x_1}\right| \frac{x_1}{f} \varepsilon x_1 + \left|\frac{\partial f}{\partial x_2}\right| \frac{x_2}{f} \varepsilon x_2 + \ldots\ldots + \left|\frac{\partial f}{\partial x_n}\right| \frac{x_n}{f} \varepsilon x_n \qquad (3.30)$$

$$\Delta f = \left|\frac{\partial f}{\partial x_1}\right| \Delta x_1 + \left|\frac{\partial f}{\partial x_2}\right| \Delta x_2 + \ldots\ldots + \left|\frac{\partial f}{\partial x_n}\right| \Delta x_n \qquad (3.31)$$

where $\varepsilon x_1, \varepsilon x_2, \ldots, \varepsilon x_n$ and $\Delta x_1, \Delta x_2, \ldots, \Delta x_n$ are respectively the relative and absolute errors of the $x_1, x_2, \ldots, x_n$ variables.

Applying the error propagation relationships (eq. 3.30-3.31) to the equations (eq. 3.27-3.28), in the hypothesis of uncorrelated variables, the relative and absolute error on the surface power εFM, ΔFM and surface astigmatic power εA, ΔA can be derived:

$$\varepsilon F_M = \varepsilon n + \varepsilon k \qquad \Delta F_M = k_M \cdot \Delta n + (n-1) \cdot \Delta k_M \qquad (3.32)$$

$$\varepsilon A = \varepsilon n + \varepsilon k_D \qquad \Delta A = k_D \cdot \Delta n + (n-1) \cdot \Delta k_D \qquad (3.33)$$

where ε and Δ denote respectively the relative and absolute error of the variables n, k_M, k_D.

3.1.5. Proposed method for optical properties estimation

In the literature, the points used for the curvature properties evaluation are identified by the n-ring neighbourhood of the point of the mesh, while, in this method, the points used are those included in a sphere. As a consequence, the tested lens area can be similar to the actual lens area used during vision or commonly adopted in the conventional measurements; noise sensitivity is reduced; mesh irregularities do not induce significant errors.

Moreover, the proposed method can be used in quality control of the lens moulds used to produce semi-finite resin spectacle lens blanks during the various steps of the manufacturing process (Meneghello et al. 2006). The actual surface of moulds can be sampled using Coordinate Measuring Machines (CMMs) or 3D scanners. Either technique is more and more frequently adopted in the ophthalmic lens field.

Finally, the proposed method can be adopted to simulate the optical properties on virtual models and therefore to support the lens design stage, particularly for progressive lens surfaces or other complex surfaces.

The proposed method is schematically described in figure 3.1a:

- the input data is a discrete model (cloud of points or mesh) derived from a virtual model or from a physical model acquired by means of reverse engineering techniques, recently introduced

in the quality control process of ophthalmic lenses;

- for every point of the discrete model, the points (local points set, lps) inside a sphere of radius lpss (local points set size) are selected (the sphere is centred on the measuring point) (figure 3.1b);
- on the local points set, a local coordinate system (u, v, w) is created, with origin on the point considered and the n-axis perpendicular to the surface (figure 3.1b);
- in the (u, v, w) coordinate system, a quadratic fitting function of the local points set is computed (figure 1b);
- the curvature properties are assessed, based on coefficients of the quadratic fitting function;
- the optical properties of the surface are calculated by the refractive index n.

Moreover, the error in curvature and optical properties calculation due to surface sampling, principal directions, nominal curvature and lpss, is estimated. In appendix D the list of command for the quadratic fitting and the estimation of optical properties in MATLAB are reported.

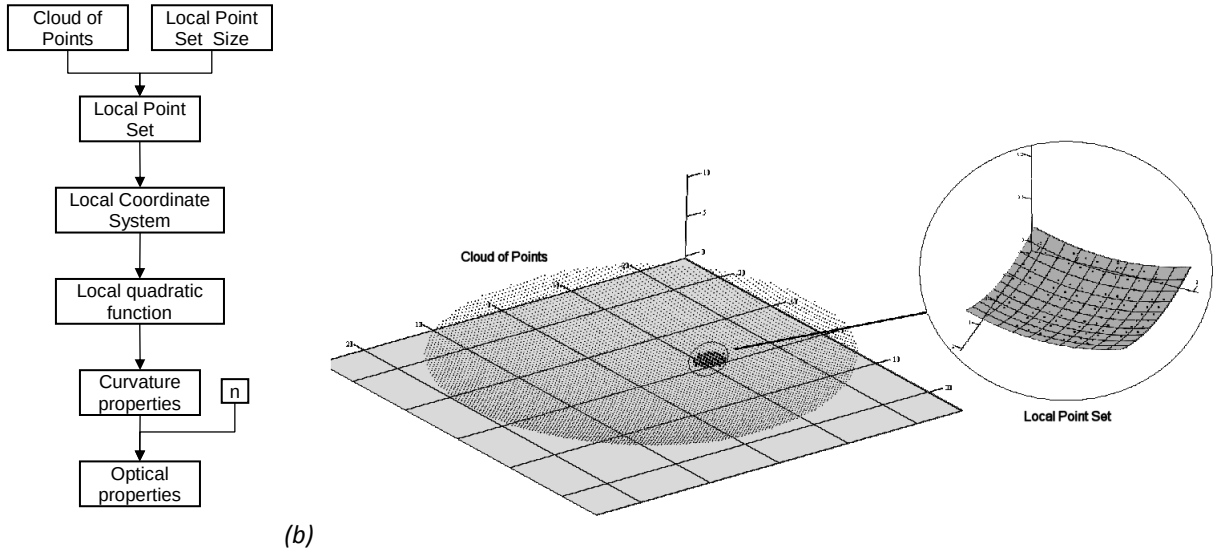

Figura 3.1 (a) Flow chart of the implemented algorithms for curvature and optical properties computation; (b) identification of the local points set for the quadratic fitting.

3.1.6. Method validation

In order to establishing the performance of the proposed method, curvature, principal directions and surface optical properties have been estimated in a set of test cases having toric shape, with surface power up to 20.00 D and surface astigmatic power up to 5.00 D, according to refractive index n=1.523 (crown glass). According to these parameters, the resulting back vertex power F_{bv} ranges between -20.00 D to +20.00 D with cylindrical power up to 5.00 D, which can be considered limit values in spectacle lens design. The test cases are described as discrete geometric models (i.e. clouds of points or meshes) characterized by variable and know sampling step, principal direction, principal curvature and lpss.

The proposed method is evaluated by the relative error on the principal curvatures (εk_1, εk_2), and by the absolute error on the mean curvature (Δk_M), on the difference between the principal curvature (Δk_D) and on the principal directions ($\Delta\varphi_1$, $\Delta_{\varphi 2}$), by means of the following relationships:

$$\varepsilon k_1 = \frac{k_{1,calc} - k_{1,nom}}{k_{1,nom}} \qquad \varepsilon k_2 = \frac{k_{2,calc} - k_{2,nom}}{k_{2,nom}} \tag{3.34}$$

$$\Delta k_M = k_{M,calc} - k_{M,nom} \qquad \Delta k_D = k_{D,calc} - k_{D,nom} \tag{3.35}$$

$$\Delta\varphi_1 = \varphi_{1,calc} - \varphi_{1,nom} \qquad \Delta\varphi_2 = \varphi_{2,calc} - \varphi_{2,nom} \tag{3.36}$$

where “calc” indicates the calculated values, while “nom” indicates the nominal values of the surface parameters.

The test cases adopted for evaluating the influence of the sampling in the curvature assessment are torii with constant ss along the x and y axes, $k_1 = k_2 = 0.01$ mm^{-1} and lpss = 4 mm, $\varphi_1 = 0$ rad $\varphi_2 = \pi/2$ rad. In the different cases, the ss parameter is varied from 0.1 mm to 2.0 mm with increment of 0.1 mm.

The principal directions are computed on a toric surface with $k_1 = 0.0125$ mm^{-1}, $k_2 = 0.01$ mm^{-1}, ss = 0.3 mm, lpss=4 mm, when φ_1 ranges between 0 to π rad with step $\pi/12$ rad. By construction, φ_2 is offset $\pi/2$ rad by φ_1.

The influence of the radius of curvature and of lpss is evaluated on test cases with ss = 0.3 mm, $\varphi_1 = 0$ rad, $\varphi_2 = \pi/2$ rad, and the values adopted for $r_1 = 1/k_1$ and $r_2 = 1/k_2$ are shown in figure 2. The radius values assumed are chosen in R10 normal numbers series according to ISO 3:1973 in a range between 25 mm and 250 mm. Every test case has been analyzed with different lpss ranging between 1 mm to 10 mm, chosen in the R5 normal numbers series (1, 1.6, 2.5, 4, 6.3, and 10).

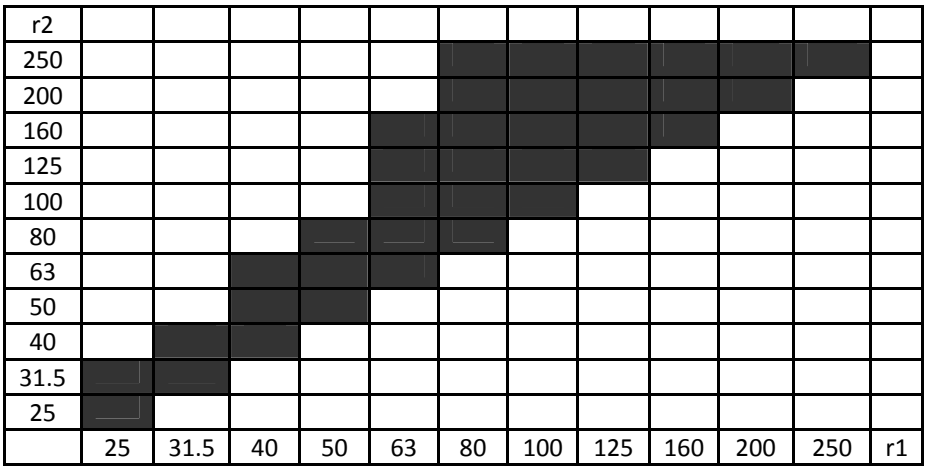

Figura 3.2 Test Cases adopted for evaluating the influence of the geometrical models curvature radius [mm] in the method performance.

By these test cases, as previously stated, an error function dependent by k_1, k_2 and lpss can be derived, defined in the range of curvatures radii typically adopted in ophthalmic lenses. In this way, by means the (eq. 32-33), the error function can be applied to the optical properties assessment.

3.1.7. Experimental results

The estimation accuracy of curvatures and optical properties, as a function of the ss, φ_1, φ_2, k_1, k_2 and lpss, was experimentally assessed as described in section 3.1.5.

The number of points (Pts) inside the sphere of radius lpss can be approximated with the following relationship:

$$\mathrm{Pts} \cong \frac{\pi \cdot \mathrm{lpss}^2}{\mathrm{ss}^2}. \qquad (3.37)$$

If Pts is less than a minimum value (<6), the fitting cannot be performed. Moreover, if Pts is less than about 100, εk_1 and εk_2 are affected by a random component, due to the low number of points taken into account in the fitting. These results are show in figure 3.3a where the errors εk_1 and εk_2 are plotted as functions of ss. Similarly, Pts can be related to ss by the function (eq. 37), plotted in figure 3.3b, for different values of lpss. The recommended minimum value for Pts (≅100) can be

derived by the figure 3.3a recognizing ss = 0.7 mm as limit value, and adopting lpss = 4 mm in the equation 3.37. Consequently the minimum recommended value of lpss for a given ss can be derived from the following relationship:

$$lpss \geq 10 \cdot ss \cdot \sqrt{\pi} \qquad (3.38)$$

or by figure 3.3b.

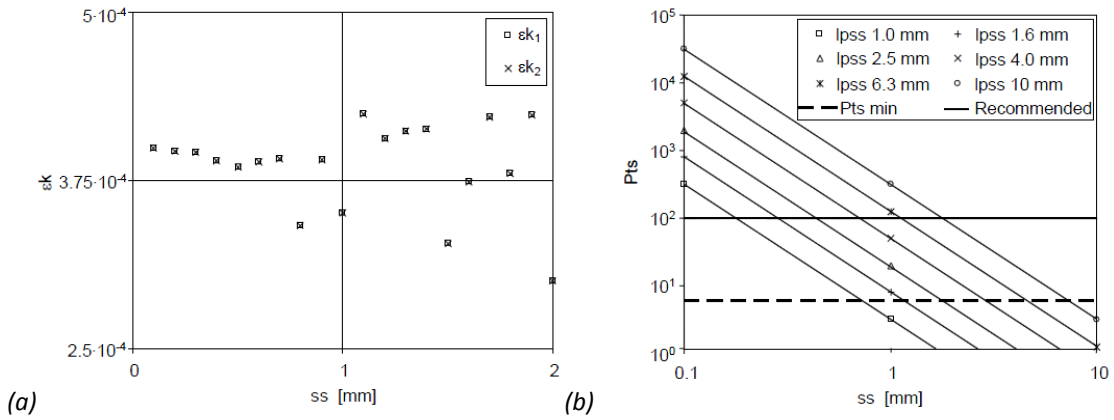

Figura 3.3 (a) Relative curvature errors (εk_1 and εk_2) vs sampling step (ss) and (b) relation between number of points (Pts) as a function of lpss and ss.

The effect of the principal direction φ_1 on the relative curvature errors and on the absolute errors on principal directions, are show in figure 3.4: the principal directions have a negligible effect on curvature error (εk_1 and εk_2) and the error on the principal directions ($\Delta\varphi_1$, $\Delta\varphi_2$) ranges between $\pm 6 \cdot 10^{-6}$ rad.

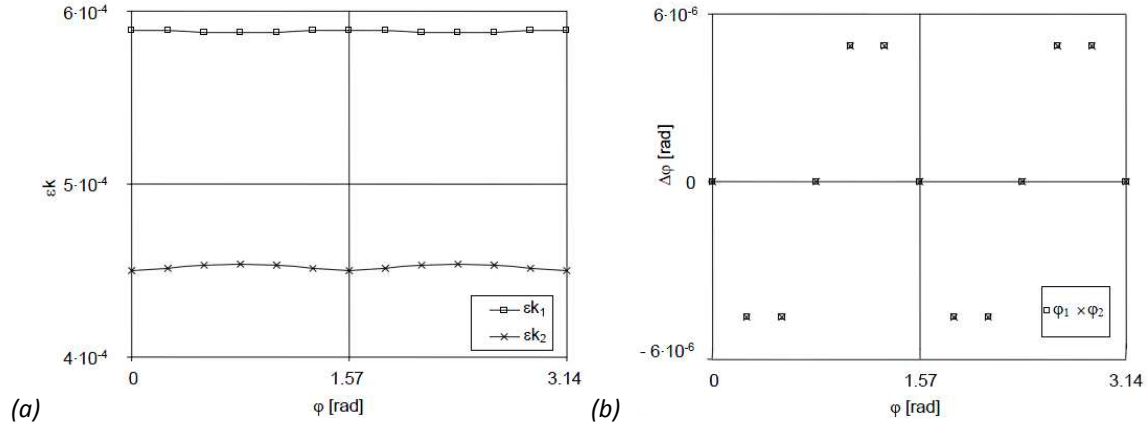

Figura 3.4 (a) Relative curvature errors (εk_1 and εk_2) vs principal direction φ_1 and (b) absolute error on principal directions ($\Delta\varphi_1$, $\Delta\varphi_2$) as a function of theoretical principal direction φ_1.

In figure 3.5a both relative errors εk_1 and εk_2 are plotted against the square of principal curvature k_1^2, assuming ss = 0.3 mm, lpss = 4 mm (comparable with eye pupil aperture in human vision) and $k_2 = 0.004$ mm^{-1}.

Analysing the test cases, εk_1 and εk_2 showed a quadratic behaviour as a function of the principal curvature k_1:

$$\varepsilon k_1(k_1) = C_1 \cdot k_1^2 + C_2 \qquad (3.38a)$$

$$\varepsilon k_2(k_1) = C_3 \cdot k_1^2 + C_4 . \qquad (3.39b)$$

Adopting a quadratic regressions, R^2 (coefficient of determination) ranges between 0.99990 and 0.99996.

Moreover, in all the test cases, for Δk_M and Δk_D a cubic dependence of the errors by k_1 can be noticed:

$$\Delta k_M(k_1) = C_5 \cdot k_1^3 + C_6 \cdot k_1^2 + C_7 \cdot k_1 + C_8 \qquad (3.39a)$$

$$\Delta k_D(k_1) = C_9 \cdot k_1^3 + C_{10} \cdot k_1^2 + C_{11} \cdot k_1 + C_{12} . \qquad (3.40b)$$

In figure 5b the absolute errors Δk_M and Δk_D are plotted as a function of k_1, assuming the same parameters as in figure 5a. Adopting a cubic regression in order to estimate the absolute errors as a function of k_1, the R^2 factor differs from unit less then 10^{-9}.

The same error trends can be obtain as a function of the principal curvature k_2 as show in figure 5c-d where ss = 0.3 mm, lpss = 4 mm and $k_1 = 0.0125$ mm^{-1}.

The linear trend for curvature relative error vs the square of principal curvature (figure 3.5c) shows $R^2 = 0.980$ for $\varepsilon k_1 = f(k_2)$, which is the worst result obtained. Moreover the cubic trend (figure 3.5d) is really close to the computed data, yielding the same R^2 factor as above.

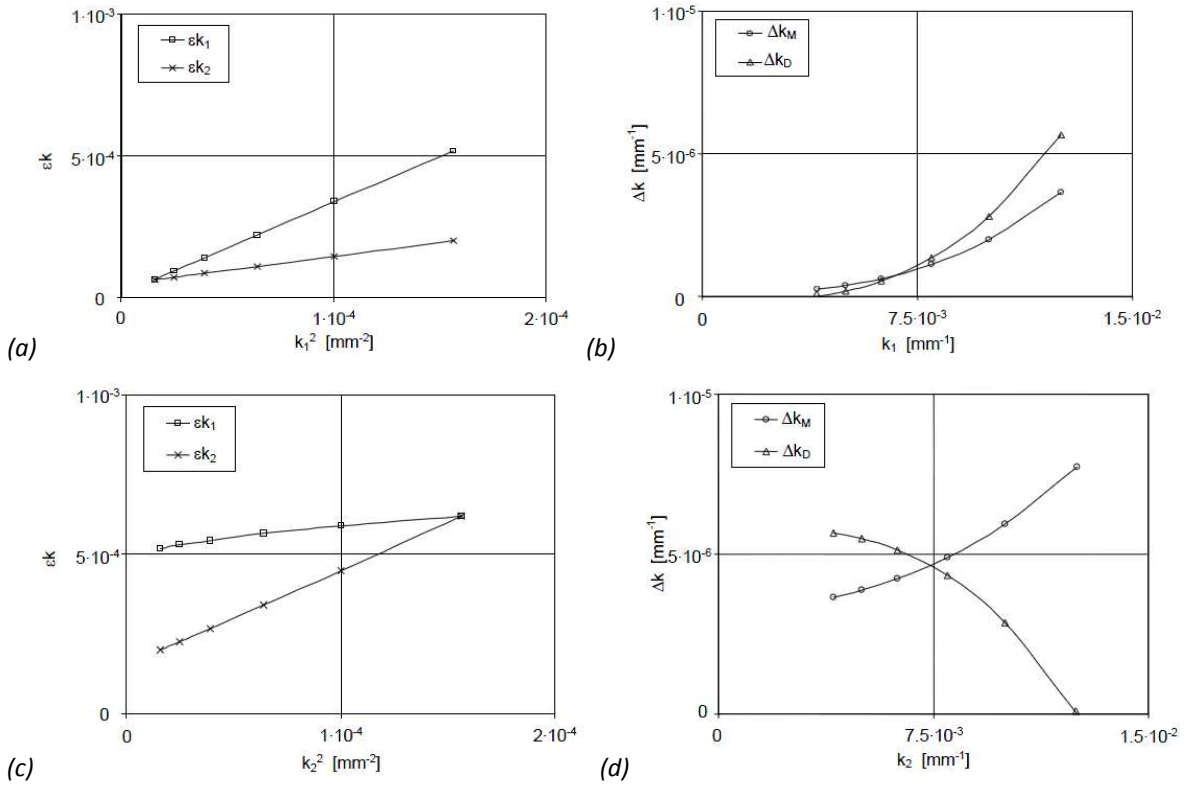

Figura 3.5 Errors on curvature estimation as a function of the principal curvatures: (a) εk_1, εk_2, (b) Δk_M and Δk_D vs k_1 (ss=0.3 mm, lpss=4 mm and k_2=0.004 mm^{-1}); (c) εk_1, εk_2, (d) Δk_M and Δk_D vs k_2 (ss=0.3 mm, lpss=4 mm and k_1=0.0125 mm^{-1}).

Similarly a quadratic dependence of relative and absolute errors εk1, εk2, Δk_M and Δk_D by lpss has been found:

$$\varepsilon k_1(lpss) = C_{13} \cdot lpss^2 \qquad \varepsilon k_2(lpss) = C_{14} \cdot lpss^2 \qquad (3.41)$$

$$\Delta k_M(lpss) = C_{15} \cdot lpss^2 \qquad \Delta k_D(lpss) = C_{16} \cdot lpss^2 \qquad (3.42)$$

as depicted in figure 3.6, where the relative and absolute errors are plotted as a function of the square of, assuming ss = 0.3 mm, $k_1 = 0.0125$ mm^{-1} and $k_2 = 0.004$ mm^{-1}.

The quadratic fitting has shown R^2 factors really close to the unit, ranging from 0.99994 (absolute error on curvature difference) to 0.99988 (relative error on maximum curvature).

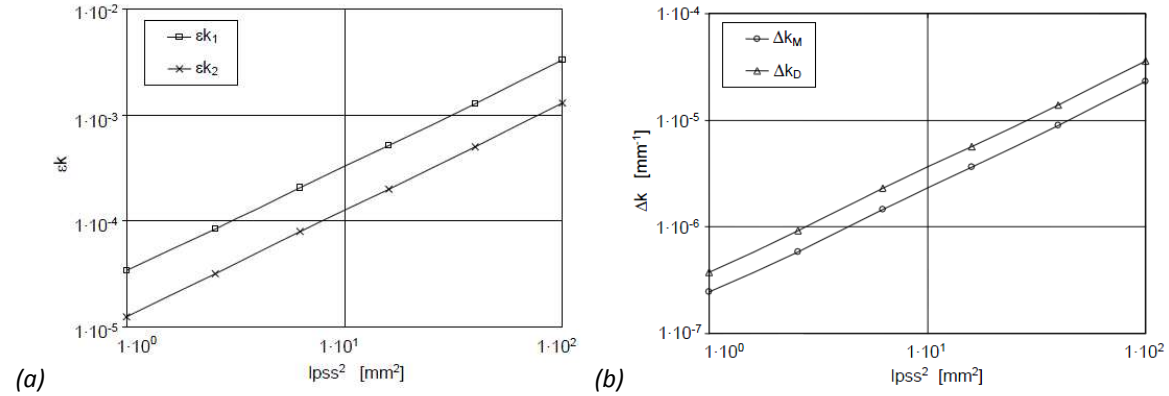

Figura 3.6 (a) Relative errors εk_1, εk_2 and (b) absolute errors Δk_M, Δk_D on curvatures estimation as a function of $lpss^2$, adopting ss=0.3 mm, k_1=0.0125 mm^{-1} and k_2=0.004 mm^{-1}.

Considering all the test cases, an error function for each εk1, εk2, Δk_M and Δk_D has been derived as a function of lpss, k_1 and k_2

$$\varepsilon k_1, \varepsilon k_2, \Delta k_M, \Delta k_D = f(lpss, k_1, k_2) \qquad (3.43)$$

by testing different regression functions.

The relative error εk1, εk2 regressions found are given by:

$$\varepsilon k_1 = \left(B1 \cdot k_1^{\,2} + B2 \cdot k_2^{\,2}\right) \cdot lpss^2 \qquad (3.44a)$$

$$\varepsilon k_2 = \left(B2 \cdot k_1^{\,2} + B1 \cdot k_2^{\,2}\right) \cdot lpss^2 \qquad (3.44b)$$

where B1 = 0.213 and B2 = 0.0533. According to this regression, a maximum error less then 9%, with an R^2 coefficient more then 0.9991 has been found, as reported in table 1.

In order to extend the obtained results to the measurement of the optical properties, the absolute error on the curvatures k_M e k_D, must be assessed. These relations can be derived using functions 3.27 and 3.28:

$$\Delta k_M = \left[\frac{B1}{2} \cdot \left(k_1^{\,3} + k_2^{\,3}\right) + \frac{B2}{2} \cdot k_1 \cdot k_2 \cdot \left(k_1 + k_2\right)\right] \cdot lpss^2 \qquad (3.45a)$$

$$\Delta k_D = \left[B1 \cdot \left(k_1^{\,3} - k_2^{\,3}\right) - B2 \cdot k_1 \cdot k_2 \cdot \left(k_1 - k_2\right)\right] \cdot lpss^2 \qquad (3.45b)$$

where B1 and B2 are the same coefficient found before. In this case, a maximum error less then 9%, with an R^2 coefficient more then 0.9990 has been found, as detailed in table 1.

Tabella 3.1 Maximum, minimum and mean errors and R factor between the computed error and relevant regression formula

Errors	Max error	Min error	Mean error	R^2
εk_1	7.8%	– 23.6%	4.0%	0.9991
εk_2	7.8%	– 8.8%	2.9%	0.9993
Δk_M	7.8%	– 3.7%	3.8%	0.9993
Δk_D	8.9%	– 5.3%	3.0%	0.9990

Consequently, the uncertainty on the surface optical properties measurements can be derived as a function of the principal curvatures k_1 and k_2, lpss, the refractive index n and its uncertainty

Δn. This result can be achieved substituting the errors model (eq. 50-51) in the error propagation relationship (eq. 32-33), obtaining:

$$\Delta F_M = \frac{k_1 + k_2}{2} \cdot \Delta n + (n-1) \cdot \left[\frac{B1}{2} \cdot \left({k_1}^3 + {k_2}^3 \right) + \frac{B2}{2} \cdot k_1 \cdot k_2 \cdot (k_1 + k_2) \right] \cdot lpss^2 \quad (3.46)$$

$$\Delta A = (k_1 - k_2) \cdot \Delta n + (n-1) \cdot \left[B1 \cdot \left({k_1}^3 - {k_2}^3 \right) - B2 \cdot k_1 \cdot k_2 \cdot (k_1 - k_2) \right] \cdot lpss^2 \quad (3.47)$$

where the uncertainties are expressed in dioptres [D or m^{-1}], the curvature in [m^{-1}] and lpss in [m].

Regarding single vision semi-finished spectacle lens blanks, the ISO 10322-1:2006 standard defines the tolerances on the surface power F_M and on the astigmatic surface power for different ranges of F1 and A. Analogously, the ISO 10322-2:2006 standard establishes the tolerances on distance surface power F_M and on distance astigmatic surface power A for different ranges of distance surface power F_1. In table 3.2, relations derived by equation 3.46 and 3.47 are given, for the different ranges reported in the ISO Standard for a crown glass (n=1.523). Through this relations, the uncertainties Δk_M and ΔA in every range of the optical properties F_1 and A can be easily estimated as a function of Δn and lpss. Consequently, establishing a maximum uncertainty on the optical properties and given the uncertainty on the refractive index Δn, the maximum value of lpss can be derived for each value of curvatures and, according to the (eq. 38); the sampling step ss can also be established.

It should be noted that in the spherical surfaces test cases ($k_1=k_2$) the uncertainty on the surface astigmatic power is zero and actually in this condition the experimental results give a negligible value of uncertainty (less then $5 \cdot 10^{-7}$ D) probably due to numerical approximation.

Tabella 3.2 Relations for estimating the maximum uncertainty in the measurement of the optical properties FM and A for the range proposed in ISO Standards

Range	ΔF_M [D]	ΔA [D]	ΔF_M [D]	ΔA [D]	ΔF_M [D]	ΔA [D]
	A = 0.00 D		0.25 ≤ A ≤ 4.00 D		4.00 < A ≤ 5.00 D	
$0.00 \le F_1 \le 2.00$ D	$3.82\Delta n+7.79lpss^2$	Negligible	$3.59\Delta n+6.48lpps^2$	$3.82\Delta n+6.23lpss^2$	$1.91\Delta+3.12lpss^2$	$3.82\Delta n+6.23lpss^2$
$2.00 < F_1 \le 10.00$ D	$19.1\Delta n+974lpss^2$	Negligible	$18.9\Delta n+938lpss^2$	$7.65\Delta n+564lpss^2$	$15.3\Delta+567lpss^2$	$9.56\Delta n+633lpss^2$
$10.00 < F_1 \le 15.00$ D	$28.7\Delta n+3287lpss^2$	Negligible	$28.4\Delta n+3206lpss^2$	$7.65\Delta n+1463lpss^2$	$24.9\Delta+2251lpss^2$	$9.56\Delta n+1704lpss^2$
$15.00 < F_1 \le 20.00$ D	$38.2\Delta n+7791lpss^2$	Negligible	$38.0\Delta n+7647lpss^2$	$7.65\Delta n+2791lpss^2$	$34.4\Delta+5834lpss^2$	$9.56\Delta n+3310lpss^2$

Finally an example of geometrical and optical properties measurements has been performed on a progressive lens surface. The lens design is based on CR-39 plastic material with refractive index n=1.498; the design data (curvature, surface power, astigmatic surface power and addition) in correspondence of the distance reference point (DRF) and of the near reference point (NRF) are reported in table 3. In the same table, the measured value of curvatures and optical properties, together with the relevant uncertainties, are detailed. Particularly, for the optical properties, the uncertainty is the combination of a component due to the refractive index and another due to the adopted method for curvature estimation. Assuming Δn = 0.0005 and lpss = 0.002 m (as in table 3.2), the uncertainty is mainly due to the refractive index. Moreover, comparing the design data with the measured values, it is possible to verify that the difference is less than the tolerance value defined in the ISO 10322-2:2006 standard.

The whole surface of the progressive design has been measured and the principal curvatures with the relevant principal directions, the surface power, the astigmatic power, the uncertainty on

the surface power and on the surface astigmatic power (evaluated by eq. 3.26a and 3.26b assuming $\Delta n = 0.0005$ and lpss = 0.002 m) are plotted in figure 3.7.

Tabella 3.3 Design data (position of the reference points, curvature and optical properties), measured value with the relevant uncertainty and tolerance assumed according the ISO standard at the distance reference point (DRP) and near reference point (NRP) for the surface of a progressive lens (Δn=0.0005, lpss=0.002 m).

	x [mm]	z [mm]	Parameter	Design data	Measured value	Uncertain due to curvature	Uncertain due to refraction index	Total uncertain	Tolerance (ISO 10322-2: 2006)
DRP	1	9	k1 [m-1]	10.5108	10.5092	± 0.0012		± 0.0012	
			k2 [m-1]	10.5108	10.5087	± 0.0012		± 0.0012	
			FM [D]	5.2344	5.2335	± 0.0006	± 0.0052	± 0.0058	± 0.09
			A [D]	0.0000	0.0002	l.t. 0.0001	l.t. 0.0001	l.t. 0.0001	± 0.09
NRP	-1.5	-13	k1 [m-1]	14.4009	14.4036	± 0.0031		± 0.0031	
			k2 [m-1]	14.4009	14.4007	± 0.0031		± 0.0031	
			FM [D]	7.1716	7.1723	± 0.0015	± 0.0072	± 0.0087	± 0.09
			A [D]	0.0000	0.0014	l.t. 0.0001	l.t. 0.0001	l.t. 0.0001	± 0.09
Addition [D]				1.9373	1.9388	± 0.0022	± 0.0124	± 0.0146	± 0.12

Other design data (point positions):
Alignment reference marking positions (x -16 mm, z 0 mm), (x 18 mm, z 0 mm)
Fitting point (x 1 mm, z 5 mm)
Prism reference point (x 1 mm, z 0 mm)
Note: x-axis and z-axis refer to figure 7 (x axis passes through the alignment reference markings).

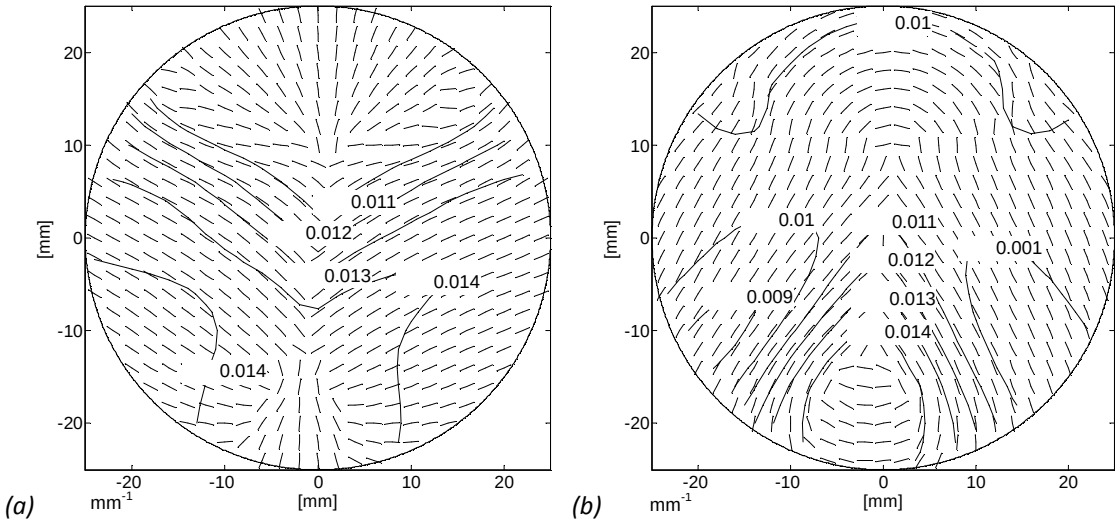

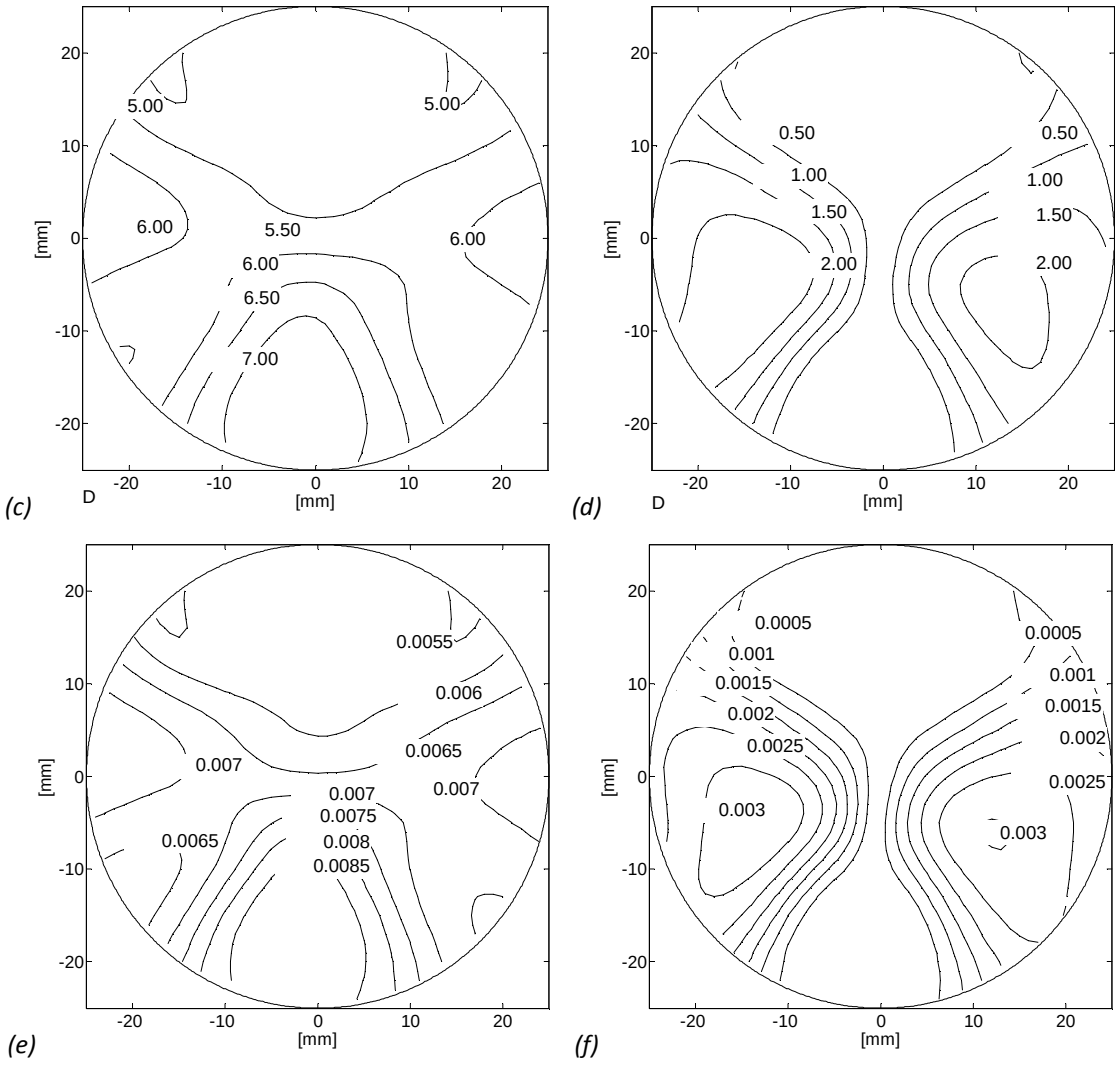

Figura 3.7 Curvature and optical properties measurements of a progressive lens surface (design data in table 3): (a) principal curvature k_1 with related principal direction (b) principal curvature k_2 with related principal direction (c) surface power (d) astigmatic surface power (e) uncertainty on surface power (f) uncertainty on astigmatic surface power.

In this work a method for optical surface properties measurement, based on curvature estimation, is proposed. The curvature estimation is assessed by a fitting method, where the selected area adopted for the surface optical properties measurement is enclosed into a sphere. In this way, the portion of surface taken into account is similar to the area used by both the eye in the human vision and the instruments commonly used to measure the surface optical properties of a lens.

By the test cases, performed on toric surfaces with typical curvatures used in the spectacle lens design, a curvature error function, dependent on the principal curvatures and on the dimension of the selected area, has been found. Consequently, adopting the propagation error relationships, the uncertainty on the optical property measurements has been established.

Following the ISO standards 10322-1: 2006 and 10322-2: 2006, the surface power can be derived from (eq. 29) by measuring the “concave spherical curve”, the thickness and the back power vertex (with a calibrated focimeter). Analogously, the proposed method can be used to assess the surface optical properties according to the ISO standards, overcoming the problem

induced by the transmission based instruments, especially regarding the quality of the not finished surface.

Moreover, as shown, the proposed method can be adopted to support the design of complex lens geometries, as progressive lenses, by allowing the computation of the optical properties on virtual models.

3.2. Ray tracing in a 3D virtual environment

In chapter 2 we have reviewed simple principles of a single ray tracing through one single surface and then through more complex optical systems. In this paragraph the basis of ray tracing in a CAD environment and examples of surfaces and mashes ray trace are shown to validate the proposed method. The ray tracing method is schematically described in figure 3.8a:

- incident vector i intersect the selected layer
- intersection point P is calculated
- layer normal ⊥ is calculated
- generalised Snell's law is applied
- refracted vector I' is found

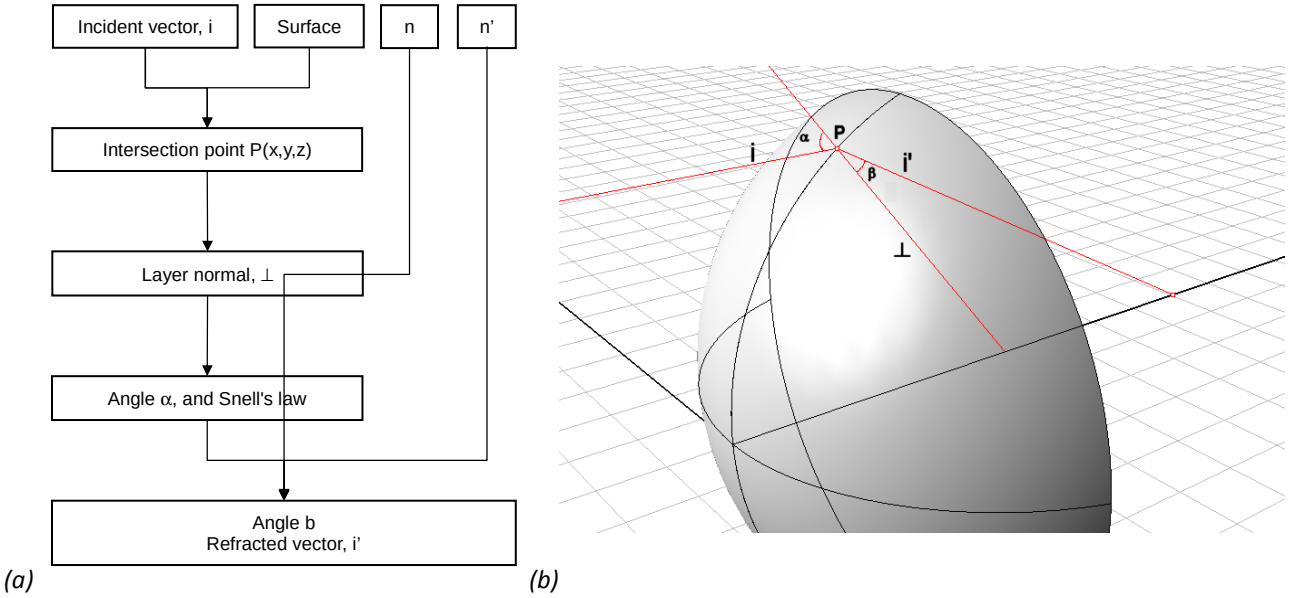

Figura 3.8 (a) Flow chart of the implemented algorithms for curvature and optical properties computation; (b) identification of the local points set for the quadratic fitting.

This scheme is repeated for every refractive layer encountered along the ray path. In this section we indicate with layer the refractive surface itself, instead we use surface to indicate the mathematical formulation of the refractive surface, and this is in contrast with mesh that is another formulation that may be used to indicate the refractive surface; these differences are used to be as close as possible to the proper CAD language.

The use of a CAD is useful for a series of reasons: the calculation of intersection points and normals are delegated to the CAD itself. In particular the CAD chosen for the analysis (Rhinoceros by McNeel & Associated) allow the use of built-in scripts for these tasks.

Furthermore a CAD is able to manage complex layers, that not necessary arise from a well defined mathematical definition. These layers are generally imported into the CAD as clouds of points fitted with a mesh, or if is possible with a surface. We will see that this is the case of

topographical image of the cornea.

As we have said the normal vector is calculated by the use of built-in function Rhino.SurfaceNormal but differences arise if the layer is a surface or a mesh. The calculation of the normal for a NURBS surface in a point P follow what already said in section 3.1.2. The calculation of the normal for a mesh needs a further explanation.

A mesh is formed by triangles that cover all the layer, number of triangle surfaces, area of the triangles, form of triangles and number of total vertices, may differ for one mesh to another. There are different methods to create a mesh from a cloud of points, but is not the aim of the present thesis to explain the different tessellation methods.

What we would like to show here is that usually an incident vector will cross a triangle in the point P, which is calculated by the CAD, but the CAD will not calculate the normal at the incident point of the mesh, and moreover the normal of the layer is not the normal of the triangle surface.

A method to find the normal $\perp$ for a mesh at the intersection point P is to first find the normals at the vertices V_1, V_2 and V_3 of the triangle and weight these normals along the distance of the point P from the vertices V, this method was proposed by Gouraud (Angel, 1990). (figure 3.9).

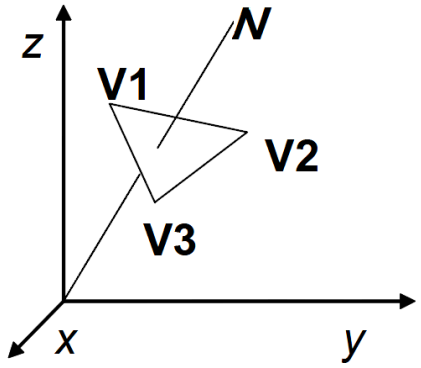

Figura 3.9 Mesh triangle of vertices V_1, V_2 and V_3 and normal n

Called u the vector between V_1 and V_2, called v the vector between V_1 and V_3 and called w the vector between the origin and V_1 we can the find the weights S and T:

$$S = \frac{(u\cdot v)\cdot(w\cdot v)-(v\cdot v)\cdot(w\cdot u)}{(u\cdot v)^2-(u\cdot u)\cdot(v\cdot v)} \qquad (3.48a)$$

$$T = \frac{(u\cdot v)\cdot(w\cdot u)-(u\cdot u)\cdot(w\cdot v)}{(u\cdot v)^2-(u\cdot u)\cdot(v\cdot v)} \qquad (3.48b)$$

using these weight the normal vector $\perp$ at the intersection point P can be calculated:

$$\perp = (1-S-T)\cdot\perp_1 + S\cdot\perp_2 + T\cdot\perp_3 \qquad (3.49)$$

where $\perp_1$, $\perp_2$ and $\perp_3$ are the normal vectors calculated, by the CAD, on the vertices V_1, V_2 and V_3.

Knowing then the incident vector i and the normal $\perp$, directly calculated from the surface or using the method explained above for a mesh, and the refraction indexes n and n', on the left and on the right of the surfaces respectively, the refracted vector i' outgoing from the layer can be calculated using the generalised Snell's law:

$$i' = \left(\frac{n}{n'}\right)i + \left(\cos\beta - \frac{n}{n'}\cos\alpha\right)\perp \qquad (3.50)$$

where angles α and β are the angles between the incident vector and the normal vector, and between the refracted vector and the normal vector respectively and are calculated by:

$$\cos\alpha = i \cdot \perp \qquad (3.51a)$$

$$\cos\beta = \sqrt{1-\left(\frac{n}{n'}\right)^2\left(1-\cos^2\alpha\right)}. \qquad (3.51b)$$

In appendix E the list of command for the ray trace in Rhinoceros is reported. Ray trace is a useful method to evaluate the performance of optical surfaces, as it was already seen in chapter 2, in the following paragraph the set up adopted for the analysis performed on the virtual eye (see chapter 5) are shown: two on-axis analysis, longitudinal spherical aberration and spot of confusion, and one off-axis analysis, power error.

3.2.1. Longitudinal spherical aberration

The effect of spherical aberration is shown in figure 3.10b, which present two rays coming from object space. If the height h_2 is close to zero the paraxial ray focus is in point P_2'.

When spherical aberration is present, non paraxial ray, i, which intercept the surface in point P_1 will not have its focus in point P_2' but in point P_1'. If the non paraxial ray intercepts the optical axis before the paraxial ray the spherical aberration is taken positive; if the paraxial ray intercepts the optical axis after the paraxial ray the spherical aberration is taken negative.

Spherical aberration is in the image space but usually in the practice the reverse of the spherical aberration is considered and called longitudinal spherical aberration which is the power of the correcting lens that must be adopted to correct in the object space the spherical aberration:

$$LSA = \frac{n'}{l'} - \frac{n'}{l'+\Delta l'} \qquad (3.52)$$

where l' is the distance between the vertex of the surface and the paraxial focus P_2'and Δl' is the distance between the two foci P_1' and P_2'.

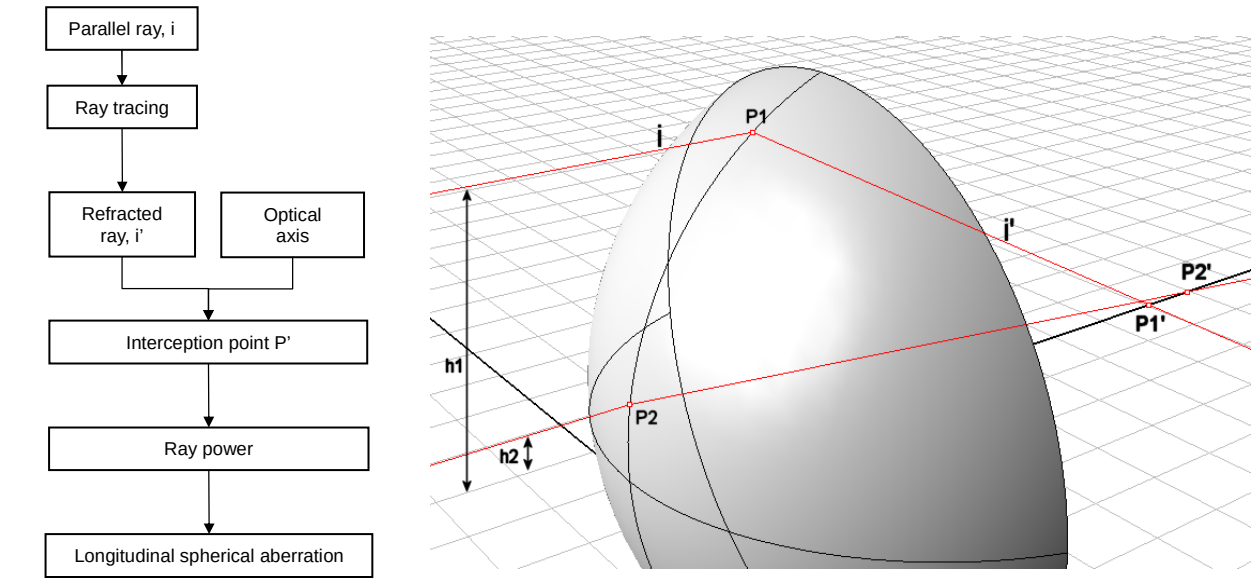

Figura 3.10 (a) Flow chart of the implemented algorithms for curvature and optical properties computation; (b) identification of the local points set for the quadratic fitting.

For the longitudinal spherical aberration tool is decided to take a parallel pencil of rays, so that the vergence of the object is taken zero. The basis of the rays is formed by concentric circles of which can be defined the maximum radius (h_1 in figure 3.10); the step between one circle and

another one can be defined as well.

Distance between one ray and another one inside the same circle is taken constant and equal to the distance between circle and circle.

The longitudinal spherical aberration method is schematically described in figure 3.10a:

- ray tracing through the n-th surfaces S_n, for n = 1 to N,
- interception between refracted ray i' and optical axis z,
- determination of the power P for non paraxial ray,
- evaluation of the longitudinal spherical aberration between non-paraxial ray and paraxial ray.

this scheme is repeated for every ray of the basis.

As it can be seen the longitudinal spherical aberration can be adopted if for the optical system under analysis the optical axis is well defined. For complex optical systems such as non rotational lenses, e.g. progressive lens, or real eyes is not always possible to define one single optical axis. So that longitudinal spherical aberration may not be defined in a unique way but can be always calculated locally. The following analysis is instead more interesting for such complex optical systems.

3.2.2. Spot of confusion

For complex systems it has been seen that may be difficult to define one single axis and so to perform the longitudinal spherical aberration analysis. The following tool is thought to overcome this problem is the analysis of the spot of confusion.

In this case is not taken a single axis, e.g. the optical axis, as reference but a whole layer is defined as reference surface. Figure 3.11a shows the schema used for the development of the CAD tool:

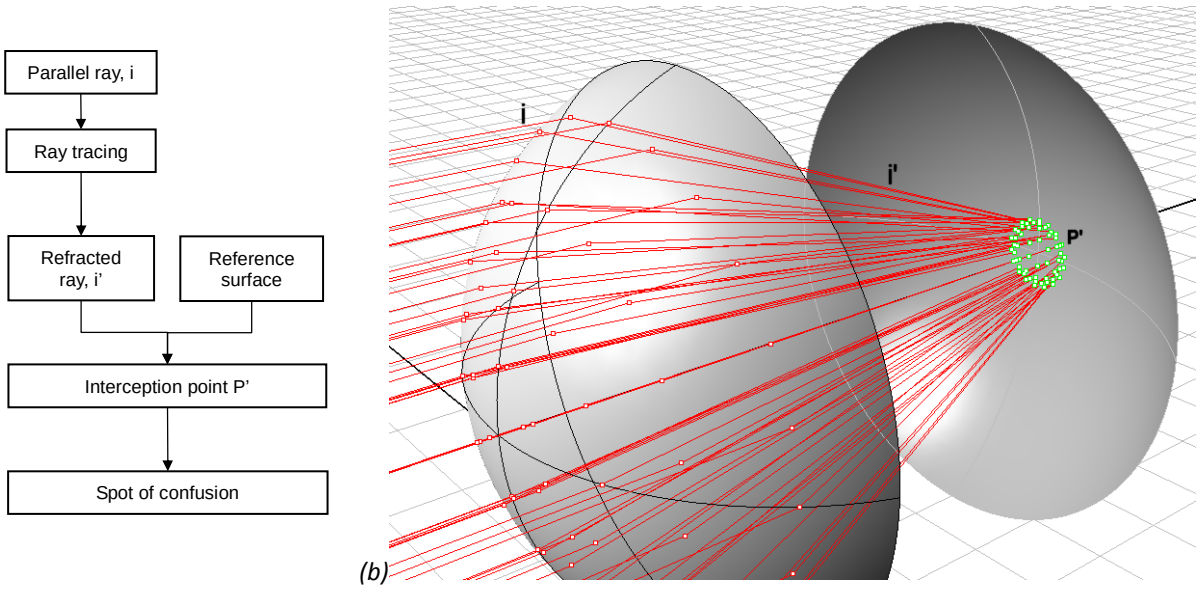

Figura 3.11 (a) Flow chart of the implemented algorithms for curvature and optical properties computation; (b) identification of the local points set for the quadratic fitting.

It can be seen that the longitudinal spherical aberration tool and the spot of confusion tool are very similar except for the reference. In figure 3.11b is depicted a complete ray basis path refracted by a single surface, the second surface instead is taken as reference and the interception points P', located on this surfaces, are shown.

The coordinate of the interception points P' can be exported from the CAD and analysed with

other tools. In particular barycentre, standard deviation of the points respect to the barycentre and area of the spot are commonly taken as interesting output data for this kind of analysis.

3.2.3. Sagittal and tangential power error

In paragraph 2.1 has been given methods to find maximum and minimum curvature of curves and surfaces. In particular if a revolution surface is considered, maximum and minimum curvatures correspond to sagittal and tangential one.

In paragraph 2.2 has been already shown the refraction by a single surface, in particular an aspheric surface where is possible to calculate tangential and sagittal radius by analytical formulation.

Our aim is to create a tool for evaluating the sagittal and tangential power also in a 3D environment. At this stage revolution surface are considered.

The basis of the rays used for the ray tracing is formed by concentric circles of which can be defined the maximum radius, the step between one circle and another one can be defined as well.

Distance between one ray and another one inside the same circle is taken constant and equal to the distance between circle and circle.

Considering a point E on the optical axis where the incident ray at different angles u will be trace through the following schema will be used for every ray (figure 3.12):

- ray tracing through the surfaces S_n,
- evaluation or calculation of the tangential radius r_t for the surface S_n at interception point P,
-- evaluation or calculation of the sagittal radius r_s for the surface S_n at interception point P,
- Coddington's law for the calculation of sagittal and tangential focus,
- ray tracing and calculation of the foci for every surface n = 1 to N,
- calculation of the sagittal and tangential power.

this scheme is repeated for every ray of the basis.

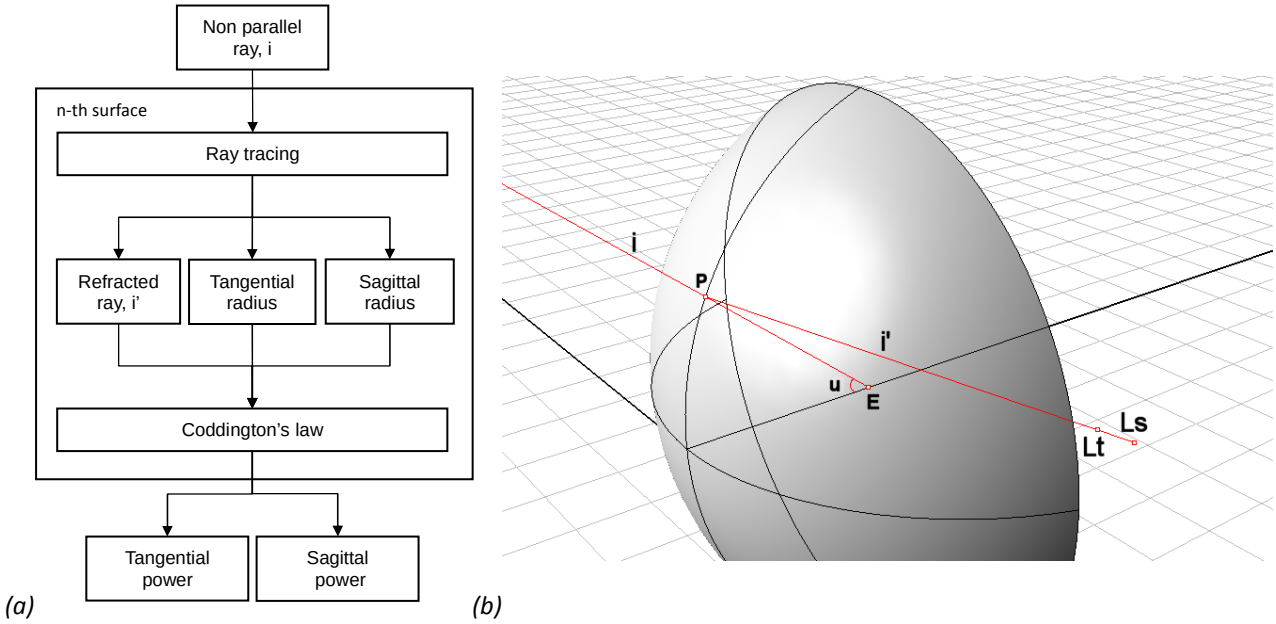

Figura 3.12 (a) Flow chart of the implemented algorithms for curvature and optical properties computation; (b) identification of the local points set for the quadratic fitting.

Usually the sagittal power L_s and the tangential power L_t are referred to the object space that is

usually air. From the sagittal and tangential power of the non paraxial rays can be then calculated the sagittal P_s and tangential P_t power errors:

$$P_s = F - L_s \qquad (3.53a)$$

$$P_t = F - L_t \qquad (3.53b)$$

where F is the paraxial, or vertex, power of the lens. From these power errors can be calculated the mean spherical power P:

$$P = \frac{P_s + P_t}{2} \qquad (3.54)$$

and the astigmatism:

$$A = P_s - P_t . \qquad (3.55)$$

Beside this direct method to calculate the curvature in chapter 3 has been shown methods to evaluate curvature of complex surfaces, where in general is not possible to define maximum and minimum curvature all over the surface but only in a local portion of it.

Following evaluation methods can be then found local sagittal and local tangential radius and the above method can be then applied also for complex surfaces. At this stage the local power is not yet implemented in CAD tools.

Chapter 4. Lens model: development and validation

The crystalline lens is one of the most complex optical elements of the eye and only few techniques, such as Scheimpflug imaging (Dubbelman and Van der Heijde, 2001; Dubbelamn et al., 2002; Rosales et al., 2006; Hermans et al. 2007) and MRI imaging (Jones et al., 2007; Kasthurirangan et al., 2008; Hermans et al. 2009) allow to obtain in vivo data.

Problems with the first technique arise from two types of optical distortions that must be addressed. The first distortion is linked with the Scheimpflug photography due to the different angles in the space between object and image planes, but this type of distortion is easy to correct.

The second type of distortion originates from the optical system of the eye. Every part of the eye (e.g. posterior cornea surface, anterior and posterior lens surface), except the anterior cornea, are photographed through different media, i.e. cornea, aqueous humor, and lens.

This creates a distortion that must be corrected knowing all individual refractive index of the ocular media. Errors become greater as long as inside part of the eye are photographed, especially the posterior lens surface that must be seen through the gradient index (GRIN) of the crystalline lens.

Dubbelman and Van der Heijde's group studied these types of distortions and developed software correction methods. Even if they use a constant refraction index for the lens instead of the gradient index, which should be more appropriate but also more difficult to handle, there is evidence of better accuracy of the Scheimpflug imaging method compared with other method such as Purkinje imaging (Rosales et al., 2006) and MRI imaging (Hermans et al., 2007).

On the other hand MRI imaging isn't affected by optical distortions and can also provide information on lens shape, in Scheimpflug imaging in fact diameter of the lens cannot be seen. It must be said that an MRI study is much longer and difficult to set up then a slit lamp, and accommodation problems must be taken into account with more care. Pixel size may also affect MRI imaging precision.

Other methods are available to derive the shape of the internal structures of the eye such as off–axis wavefront measurements proposed by Goncharov et al. (2008). Similarly, ocular wavefront tomography (OWT) is the process of using wavefront aberration maps obtained along multiple lines-of-sight proposed by Wei and Thibos (2008).

Beside this in vivo measurements, ex vivo imaging techniques, such as the optical coherence tomography (OCT), are able to obtain the crystalline lens shape (Urs et al., 2009; Urs et al., 2010) and the grin distribution (de Castro et al., 2010).

To describe the geometry of the lens, acquired by the techniques described above, different mathematical models were proposed and used for optical and biomechanical analysis.

Despite the complexity of the lens, its surface is commonly approximated by conicoid of revolution with the meridian section in the y–z plane given by the equation:

$$y^2 = 2Rz - (1+q)z^2 \qquad (4.1)$$

where y is the radial distance from the optical axis, z is the surface sagitta, R is the vertex radius

and q is the asphericity coefficient.

Most of the data that can be found in the literature report the radius R and the coefficient q, and they refer to in vitro investigations (Liou and Brennan, 1997; Howcroft et al., 1977; Pierscionek and Chan, 1989; Glasser and Campbell, 1999; Schachar, 2004; Manns et al., 2004; Rosen et al., 2006).

As we have said in chapter 1 this function is very simple but it has two problems: r and q depend on the central fitting area used in its determination and usually is not possible to link anterior and posterior part of the lens continuously at the equator.

To counter this problem different models have been developed. First simple modification of the conicoid was done adding figuring terms, as Smith (2003); this allows the modification of the junction zone without altering the optical zone of the lens.

Using different conicoid patches along the lens surface, and rules to connect these patches together, Hermans et al. (2009) are able to model a lens that was successively used for mechanical studies of the ciliary muscle stress on the lens.

Beside these modification of conicoids other models are developed, Kasprzak (2000) one use a hyperbolic cosine function to modelise the lens in one single equation with continuous curvature characteristics really important for both optical and mechanical behaviour, but his function was difficult to use due the number of coefficients adopted. Urs et al. (2010) are able to use 10th-order Fourier series to develop an interesting age-dependent model validated with shadow photogrammetry image.

In this chapter it is proposed and verified a derivation of Chien et al. lens model coefficients based on geometrical constraints. MRI image (in vivo) or OCT (ex vivo) should be preferable to derive the coefficients of the proposed model, which uses the equatorial radius as an input data. Scheimpflug image can also be used but the equatorial radius must be derived from the literature. Beside experimental techniques, a large amount of literature data can be directly used to calculate the model coefficients.

The curvature continuity of the proposed model is useful for both optical (power and aberration statements) and biomechanical analysis (e.g. accommodation or FEM analysis).

4.1. Chien model

Chien et al. (2003) proposed and analysed twelve different mathematical lens models. The best function that fits Fincham's lens data (1937) from photomicrography is:

$$\begin{aligned} z(u) &= \left(b_0 + b_1 u^2 + b_2 u^4\right)\cdot \cos u \\ y(u) &= a \cdot \sin u \end{aligned} \qquad (4.2)$$

where u is the parameter ranging between 0 to $\pi/2$, z is the direction along the optical axis, y is the distance from the optical axis in radial direction, a and b_i are coefficients which are found with a fitting process. The reliability of the proposed model was confirmed by fitting five independently published MRI images from three different crystalline lenses. As Kasprzak model Chien equation is designed to link anterior and posterior part in a smooth way at the equator.

While on the one hand the simple models do not provide a continuous junction between the anterior and the posterior surface of the lens and than they do not qualify for biomechanical simulation, from the other hand more complex model do not provide a geometrical or optical interpretation of the coefficient involved in the model, which are typically derived by fitting or optimization methods that are often not define clearly.

The parametric model proposed is based on Chien et al. model (2003) in which the coefficients a and b_i are derived from geometrical constraint and not by fitting methods. Subsequently it was

obtained a physical interpretation of the Chien model coefficients, which derived from the thickness and the radius of curvature of the anterior and posterior lens side, and from the equatorial radius. Like most of the models proposed in the literature, both anterior and posterior surfaces of the lens are rotationally symmetric and consequently the profile of the lens is well defined, adopting the z–axis as optical axis and the y–axis as the radial axis positioned in the equatorial plane (see figure 4.1).

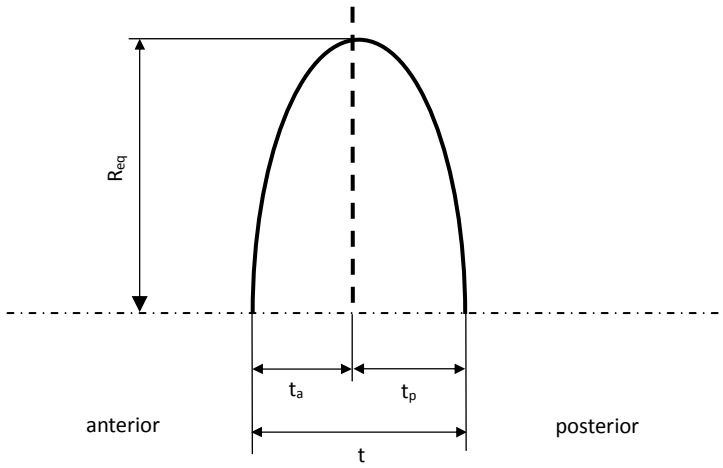

Figura 4.1 Reference frame definition for a crystalline human lens

Following this model the anterior part of the lens can be described by parametric function:

$$\begin{aligned} z_a(u) &= \left(b_{0a} + b_{1a}(\pi - u)^2 + b_{2a}(\pi - u)^4\right)\cdot \cos u \\ y_a(u) &= a_a \cdot \sin u \end{aligned} \quad \text{for} \quad \pi/2 \le u \le \pi \qquad (4.3)$$

while the posterior part of the lens can be written as:

$$\begin{aligned} z_p(u) &= \left(b_{0p} + b_{1p}u^2 + b_{2p}u^4\right)\cdot \cos u \\ y_p(u) &= a_p \cdot \sin u \end{aligned} \quad \text{for} \quad \pi/2 \le u \le \pi \qquad (4.4)$$

where u substitution with $(\pi - u)$ allows to mirrored the equation 4.3 and simultaneously gives a continuous passage through the junction zone due to parameterization.

This definition is compatible both with a canonical mathematical definition of the angles where the angles grow counter clockwise and with the lens disposition in an optical system so that the anterior part of the lens stands on the left and the posterior part stands on the right of the equatorial plane that pass through the origin of the axis (figure 4.1).

Any geometrical constraints, such as the vertical tangent in the optical axis or the horizontal tangent in the junction zone at the equator, were already proposed by Chien et al. in order to identify possible model equations.

To derive the eight coefficient a_i and b_i, eight geometrical constraints was imposed adopting simple considerations.

4.1.1. Geometrical constraints

We now show the geometrical constraints used to define the first set of parameters. To respect the lens shape, both the equation at the equator (where $z_a = z_p = 0$) must be equal to the lens

equatorial radius R_{eq}, than:

$$y_a\left(\frac{\pi}{2}\right) = y_p\left(\frac{\pi}{2}\right) = R_{eq}. \quad (4.5)$$

Taking into account the lens shape, in the optical axis ($y_a = y_p = 0$) the z_a value of the functions 7a must be equal to thickness of the anterior side t_a, while the z_p value of the functions 7_b must be equal to thickness of the posterior side t_p, than:

$$\begin{aligned} z_a(\pi) &= t_a \\ z_p(0) &= t_p \end{aligned} \quad (4.6)$$

These set of constraints are linked only to the contour extrema (thickness and equatorial radius) of the lens profile, so that we have call them geometrical constraints. By the first condition and the second condition the coefficients a_a, a_p, b_{0a} and b_{0p} were easily found:

$$a_a = a_p = R_{eq} \quad (4.7)$$

$$\begin{aligned} b_{0a} &= t_a \\ b_{0p} &= t_p \end{aligned} \quad (4.8)$$

4.1.2. Optical constraints

To ensure the optical properties, in the optical axis ($y_a = y_p = 0$) the curvature radius of anterior side R_a and posterior side R_p must be respected, than:

$$\begin{aligned} r(\pi) &= R_a \\ r(0) &= R_p \end{aligned} \quad (4.9)$$

calculating r(θ) by the equation 2.6 for $u = 0$ and $u = \pi$ the following relationships were obtained:

$$\begin{aligned} r(\pi) &= \frac{a_a^{\,2}}{b_{0a} - 2b_{1a}} \\ r(0) &= \frac{a_p^{\,2}}{b_{0p} - 2b_{1p}} \end{aligned} \quad (4.10)$$

Replacing in equation 4.10 a_a, a_p, b_{0a} and b_{0p}, derived from equations 4.7 and 4.8 and taking into account the constraints of equation 13, the coefficient b_{1a} and b_{1p} was found:

$$\begin{aligned} b_{1a} &= \frac{1}{2}\left(t_a - \frac{R_{eq}^{\,2}}{R_a}\right) \\ b_{1p} &= \frac{1}{2}\left(t_p + \frac{R_{eq}^{\,2}}{R_p}\right) \end{aligned} \quad (4.11)$$

we would like to remind that the radius of curvature of the anterior and posterior part of the lens are taken with their sign, so that the anterior one is taken positive and the posterior one is taken negative, so that the different sign in equation 4.11 arise.

The constraint of equation 13 ensures a good trend of the optical zone only at a first order of approximation. To let the model follow more the shape of the lens is necessary to expand the equation 4.2 in Taylor series. The explicit equation of the model for anterior part is from equation 4.4:

$$z_a = -\left(b_{0a} + b_{1a}\,\mathrm{asin}\left(\frac{y}{a}\right)^2 + b_{2a}\,\mathrm{asin}\left(\frac{y}{a}\right)^4\right) \cdot \frac{\sqrt{a^2 - y^2}}{a} \quad (4.12)$$

where the function cos(asin(y/a)) it has been explicitated. On the other hand the surfaces of the lens are usually approximated in the literature as conicoid:

$$z_a = \frac{y^2}{R_a + \sqrt{R_a - (1+q_a)y^2}} - t_a \qquad (4.13)$$

where the term t_a give the displacement of the conicoid so that the equator stands in z = 0, the conicoid has an important feature when that function is used to fit an image that can be the imaging of the crystalline lens or of the cornea or other optical surfaces.

The term R is the curvature radius of the central zone when y = 0, so that it is linked to a punctual characteristic of the surface. The term q is the aspherical coefficient as already pointed out and it is linked to the size of the fitting zone (Smith et al., 2009). This characteristic of the q coefficient is for sure not ideal if we want to fit a single conicoid on the lens surface but for our purpose is important since it is linked to a whole region of the lens and not only to a single point.

If we in fact expand in Taylor's series the aspheric function till the 6th term we obtain:

$$z_a = -t_a + \frac{1}{2R_a}y^2 + \frac{1+q_a}{8{R_a}^3}y^4 \qquad (4.14)$$

and if we do it swell for the Chien equation we obtain:

$$z_a = -b_{0a} + \left(\frac{b_{0a}}{2a^2} - \frac{b_{1a}}{a^2}\right)y^2 + \left(\frac{b_{0a}}{8a^4} + \frac{b_{1a}}{6a^4} - \frac{b_{2a}}{a^4}\right)y^4 \qquad (4.15)$$

If we want that in a region close to the optical axis, corresponding to the fitting zone, the model follow the aspheric equation 4.14 and 4.15 must be equated. Doing that we can easily found the coefficients b_{0a} and b_{1a} which meaning is already explained before. Instead equating:

$$\left(\frac{b_{0a}}{8a^4} + \frac{b_{1a}}{6a^4} - \frac{b_{2a}}{a^4}\right) = \frac{1+q_a}{8{R_a}^3} \qquad (4.16)$$

we can find the last coefficient b_{2a}:

$$b_{2a} = \frac{5}{24}t_a - \frac{1}{12}\frac{{R_{eq}}^2}{R_a} - \frac{1+q_a}{8}\frac{{R_{eq}}^4}{{R_a}^3} \qquad (4.17)$$

as it can be seen this constraints is closely linked to the shape of the whole anterior surface, by the use of the q coefficient. On the other hand if we would like to construct the aspheric function from the model we can find the asphericity coefficient q:

$$q = \frac{5}{3}\frac{{R_a}^3 t_a}{{R_{eq}}^4} - 8\frac{{R_a}^3 b_{2a}}{{R_{eq}}^4} - \frac{2}{3}\frac{{R_a}^2}{{R_{eq}}^2} - 1 \qquad (4.18)$$

where the terms referred to the anterior part of the lens may be substituted with the ones referred to the posterior one to find the posterior asphericity.

We have now to assess the last coefficient, to ensure continuity in the equatorial plane ($z_a = z_p = 0$) the same radius of curvature for both sides of the lens was imposed:

$$r_a\left(\frac{\pi}{2}\right) = r_p\left(\frac{\pi}{2}\right), \qquad (4.19)$$

in the equatorial plane, where $u = \pi/2$, the radius of curvature is given by:

$$r_a\left(\frac{\pi}{2}\right) = \frac{\left(z_a'\left(\frac{\pi}{2}\right)\right)^2}{y_a''\left(\frac{\pi}{2}\right)} \qquad (4.20)$$

$$r_p\left(\frac{\pi}{2}\right)=\frac{\left(z_p'\left(\frac{\pi}{2}\right)\right)^2}{y_p''\left(\frac{\pi}{2}\right)} \qquad (4.20)$$

One can show that the derivate of $y_a''(\pi/2) = y_p''(\pi/2) = -R_{eq}$ so that the previous equation become after some substitutions:

$$z_p'(\pi/2)=-b_{0p}-\frac{\pi^2\cdot b_{1p}}{4}-\frac{\pi^4\cdot b_{2p}}{16}=-b_{0a}-\frac{\pi^2\cdot b_{1a}}{4}-\frac{\pi^4\cdot b_{2a}}{16}=z_a'(\pi/2) \qquad (4.21)$$

and as a result:

$$b_{2p}=b_{2a}+2\frac{\pi^2+8}{\pi^4}\left(t_a-t_p\right)-2\frac{{R_{eq}}^2}{\pi^2}\left(\frac{1}{R_a}+\frac{1}{R_p}\right). \qquad (4.22)$$

These set of constraints are linked to optical properties of the central zone, by the radius of curvature R; to the whole optical zone, by the aspherical coefficient q; and let the model to have a continuous curvature along the whole profile, so that we have call the optical constraints.

Moreover, all the geometrical and optical constraints involved in the model are often available in the literature and frequently several equation relate this parameter with accommodation and age (Hermans et al., 2009; Rosen et al., 2006).

We summarise the presented model function and coefficient in the table 4.1:

Tabella 4.1 Proposed model function and coefficient

Anterior surface $\pi/2 \le u \le \pi$	Posterior surface $0 \le u \le \pi/2$
$z_a(u)=\left(b_{0a}+b_{1a}(\pi-u)^2+b_{2a}(\pi-u)^4\right)\cdot\cos u$	$z_p(u)=\left(b_{0p}+b_{1p}u^2+b_{2p}u^4\right)\cdot\cos u$
$y_a(u)=a_a\cdot\sin u$	$y_p(u)=a_p\cdot\sin u$
$a_a=R_{eq}$	$a_p=R_{eq}$
$b_{0a}=t_a$	$b_{0p}=t_p$
$b_{1a}=\frac{1}{2}\left(t_a-\frac{{R_{eq}}^2}{R_a}\right)$	$b_{1p}=\frac{1}{2}\left(t_p+\frac{{R_{eq}}^2}{R_p}\right)$
$b_{2a}=\frac{5}{24}t_a-\frac{1}{12}\frac{{R_{eq}}^2}{R_a}-\frac{1+q_a}{8}\frac{{R_{eq}}^4}{{R_a}^3}$	$b_{2p}=b_{2a}+2\frac{\pi^2+8}{\pi^4}\left(t_a-t_p\right)-2\frac{{R_{eq}}^2}{\pi^2}\left(\frac{1}{R_a}+\frac{1}{R_p}\right)$

4.2. Model analysis

We divide the analysis of the model into two different comparisons. The first part of the analysis is to compare the proposed model against four models presented in the literature: two independent conic equations, two interdependent figuring conicoid equations, conic patches model and modulated hyperbolic cosine.

This analysis allows us to understand which existing model the proposed model is closed to, and which the characteristics of the proposed model are then.

After that we have compare the proposed model against shadow-photogrammetry imaging data provided by R. Urs and F. Manns of the Ophthalmic Biophysics Center, Bascom Palmer Eye Institute, University of Miami Miller School of Medicine, Miami, USA.

This analysis allows us to check the performance of the presented model against real raw data, and to develop a growing model.

4.2.1. Proposed model against literature models

Adopting the proposed model as reference, shape, volume and curvature are compared with four models presented in the literature: two independent conic equations, two interdependent figuring conicoid equations, conic patches model and modulated hyperbolic cosine.

Input data for the model coefficients (Smith et al., 2009; Hermans et al., 2009; Kasprzak, 2000) are found in Smith et al. (2009) which used edge coordinates raw data obtained by Jones et al. (2007), relevant to a seven year old in vitro lens measured by from MRI imaging (see tables 2–5).

For the proposed model (7a, 7b) three different shapes, respectively called Model A, Model B and Model C, were adopted (see table 6).

The shape of the two conics model was derived by equation 1 assuming the parameters collected in table 4.2 (Smith et al., 2009) and substituting z with (t_a+z) for the anterior side and z with (t_p–z) for the posterior side of the lens, where the thickness t_a and t_p are referred to table 4.3. The two conics model was compared to Model A, where R_{eq} is referred to table 4.3.

The figuring conicoid shape was found by equation 2 assuming the parameters of table 4.3 and substituting z with (t_a+z) for the anterior side and z with (t_p–z) for the posterior side of the lens (Smith et al., 2009).

The profile of the conic patch model has been drawn applying the coefficients of table 4.4 to the equations 3a, 3b, and 3c. This coefficients are derived by the equations 7, 8, 9 and 10 of Hermans et al. (2009), adopting the thickness, the radii of curvature and the equatorial radius of Smith et al. (2009) The figuring conicoid model and the conic patch model were compared to Model B.

The contour of hyperbolic cosine model was derived adopting the equations 4, 5a and 5b and the parameters of table 4.5, data of the original work of Smith et al. R_{eq} is the maximum of the model equation, and the thickness is derived after the profile was translated along the z axis, in order to obtain the maximum in z = 0.

The profile of the Urs model was taken by parameter given in Urs et al. (2010) with an age equal to seven years and the coefficients are reported in table 4.6.

Tabella 4.2 Parameters for the two conic model

Parameter	Anterior surface	Posterior surface
R (mm)	6.191	– 4.849
q	0.921	0.296

Tabella 4.3 Parameters for the figuring conicoid model

Parameter	Anterior surface	Posterior surface
R (mm)	6.263	– 4.759
q	+ 0.718	+ 0.054
v1 (mm^{-1})	– 0.529621	– 0.102213
v2 (mm^{-1})	+ 0.191767	+ 0.078712
v3 (mm^{-1})	– 0.040665	– 0.029001
t (mm)	2.284	2.71
R_{eq} (mm)	4.004	

Tabella 4.4 Parameters for the conic patch model

Parameter	Anterior surface	Posterior surface
R (mm)	6.263	– 4.759
c (mm^{-1})	0.708	0.603
k	0.466	0.348
t (mm)	2.284	2.71
R_{eq} (mm)	4.004	

Tabella 4.5 Parameters for the hyperbolic cosine model

Parameter	Anterior surface	Posterior surface
a	0.965	0.977
b	1.186	1.061
s	1.808	1.669
m	3.706	
t (mm)	5.014	

Tabella 4.6 Parameter for the 10th-order Fourier series

Parameter	Anterior Surface	Posterior Surface
t (mm)	1.736	2.187
R_{eq} (mm)	8.658	
A_0	2.703	
A_1	0.237	
A_2	-1	
A_3	$8.13 \cdot 10^{-3}$	
A_4	0.378	
A_5	-0.032	
A_6	-0.164	
A_7	0.027	
A_8	0.064	
A_9	-0.014	
A_{10}	-0.02	

Tabella 4.7 Constraints adopted to define the shape of the lens adopting the proposed model, to compare it with the other models mentioned in the first column (values in mm).

Proposed model	Compared model	R_a	R_p	q_a	t_a	t_p	t	R_{eq}
Model A	Two conics	6.191	– 4.849	0.921	2.284	2.710	4.994	4.003
Model B	Figuring conicoid and conic patch	6.263	– 4.759	0.718	2.284	2.710	4.994	4.003
Model C	Hyperbolic cosine	5.431	– 4.454	– 0.078	2.339	2.675	5.014	3.992
Model D	Fourier series	6.160	– 4.160	– 2.500	1.736	2.187	3.922	4.329

The shape of the proposed model is compared with the others, plotting above the lens profile the magnified normal deviation. To summarize this results it was adopted the merit function proposed in Smith et al., which is the sum of the square error evaluated along the normal to the lens profile of the proposed model.

The merit function was performed in the optical zones, in the junction zones and in all the lens profile. Moreover, maximum and average distances between models are calculated.

In CAD environment Rhinoceros, starting from the lens profile equation, a solid of revolution

was created and then the volume is assessed. This property is particularly interesting in the models that perform the accommodation, which consider a constant volume during this phase.

Another geometrical characteristic often adopted in the lens evaluation is the radius of curvature. In this study it is performed adopting the circular fitting method proposed in the chapter 3 and it is plotted against the radial y–axis.

4.2.1.1. Results

Figure 4.2 shows the results of the normal deviation with its sign, between the proposed model and the other ones, magnified 20 times. It can be seen that, except for the two conics model near to the junction, the highest difference is lower than 0.08 mm.

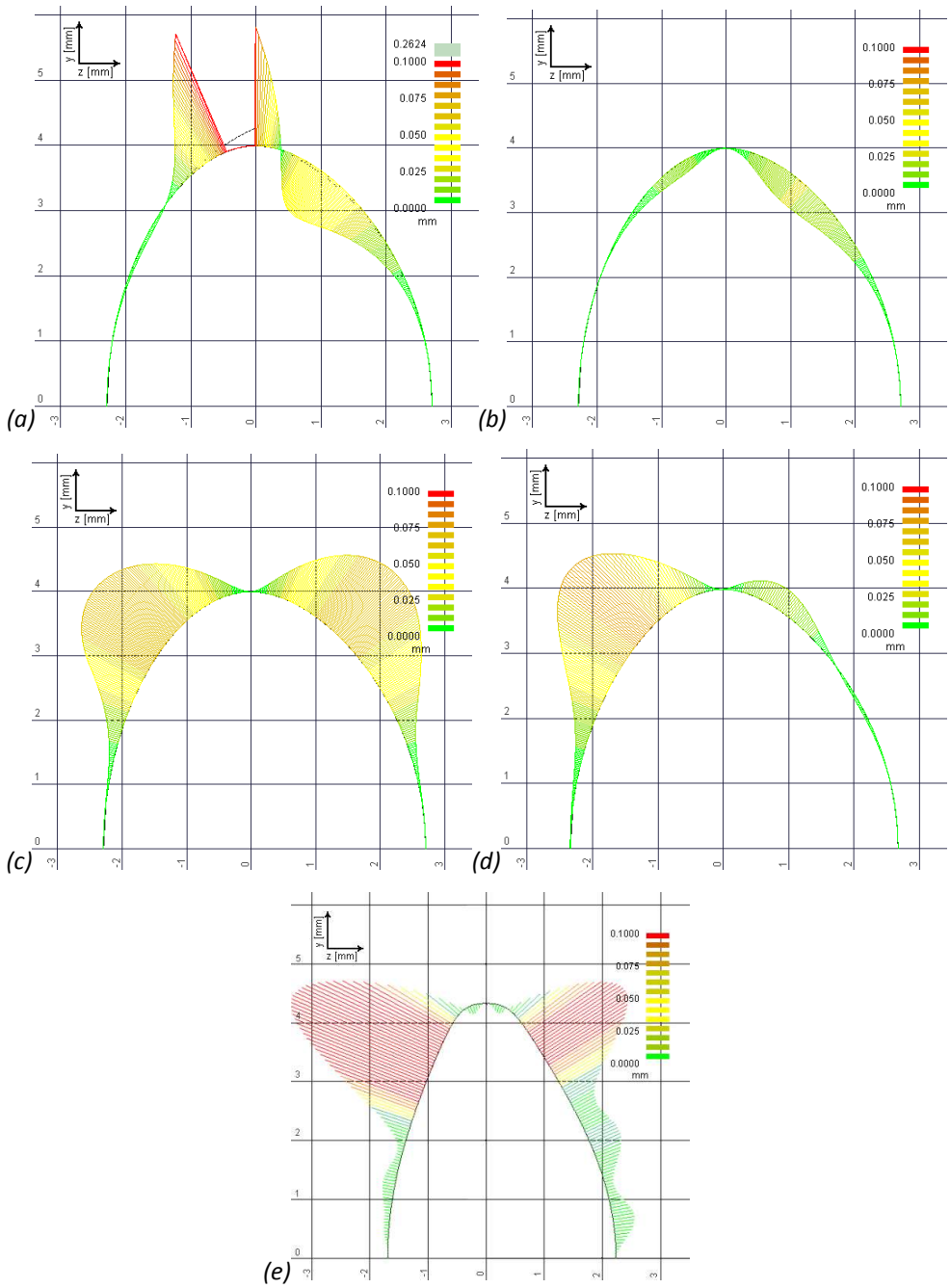

Figura 4.2 Comparison between the shape of the proposed model and other models: (a) two conics, (b) figuring conicoid, (c) conic patch, (d) hyperbolic cosine, (e) 10th-order Fourier series. The normal distances between the models, magnified 20 times, are depicted above the profile of the proposed model.

Looking at the anterior (y<2.5 mm) and posterior (y<2 mm) optic zone (the y amplitude is selected following the work of Hermans et al.) we can see that the proposed model is very close to both the two conics and the figuring conicoid models, which are the more typically implemented in the optical analysis. Moreover the posterior side of the lens of the hyperbolic cosine is much closed to the proposed model.

From an optical point of view this may lead to a situation where despite the differences in shape it can be seen fewer differences in power or spherical aberration this happen since the posterior zone drives more than the anterior part the total power of the crystalline lens, due to the highest curvature of the surface.

It can be seen (figure 4.2b) that the proposed model fits very well the figuring conicoid model in all the lens profile. In this case the maximum deviation between the models is equal to 22 μm (see table 4.8) which appear out of the optical zone, while the average deviation between them is equal to 4.8 μm.

In table 4.8 the deviations between the models are quantitatively summarized by the merit function for the whole lens and for its portions, together with the maximum and the average distances. Analysing this results similar conclusion can be drawn:

- the merit function between the proposed and the figuring conicoid model is the least in the anterior optic zone, in the anterior junction zone and in all the profile,
- the merit function between the proposed and the hyperbolic cosine model is the least in the posterior optic and junction zones,
- the merit function assume little value in the optical zones (less than $2.5 \cdot 10^{-6}$ mm^2) for the two conicoid and the figuring conicoid models,
- average and maximum deviations confirm that the figuring conicoid model is the closest to the proposed model.
- maximum deviation and average deviation for the Fourier series is higher then the other models.

Tabella 4.8 Merit Function, maximum and average deviation of the proposed model against the other ones. In addition to results for the entire lens profile, the values of merit function in anterior optic zone (z<0, y<2.5 mm), posterior optic zone (z>0, y<2 mm), and the two junction zones are shown.

Lens countour	Merit function [mm^2]					Max deviation [mm]	Average deviation [mm]
	Anterior optic zone	Anterior junction zone	Posterior junction zone	Posterior optic zone	All profile		
Two conics	$6.11 \cdot 10^{-7}$	$5.19 \cdot 10^{-3}$	$2.33 \cdot 10^{-4}$	$2.44 \cdot 10^{-6}$	$1.84 \cdot 10^{-3}$	0.262	0.0207
Figuring conicoid	$2.77 \cdot 10^{-8}$	$8.74 \cdot 10^{-6}$	$4.25 \cdot 10^{-5}$	$1.22 \cdot 10^{-6}$	$3.99 \cdot 10^{-5}$	0.022	0.0048
Conic patch	$1.16 \cdot 10^{-4}$	$5.33 \cdot 10^{-4}$	$3.90 \cdot 10^{-4}$	$1.85 \cdot 10^{-5}$	$6.23 \cdot 10^{-4}$	0.070	0.0245
Hyperbolic cosine	$1.29 \cdot 10^{-4}$	$6.58 \cdot 10^{-4}$	$3.19 \cdot 10^{-5}$	$4.08 \cdot 10^{-8}$	$6.07 \cdot 10^{-4}$	0.076	0.0170
10th-order Fourier	$1.27 \cdot 10^{-4}$	$2.24 \cdot 10^{-3}$	$8.46 \cdot 10^{-4}$	$5.06 \cdot 10^{-5}$	$1.55 \cdot 10^{-3}$	0.134	0.0375

In table 4.9 are summarised data for the volumes of the lenses. The proposed model have very similar volume in the case A and B, while in the case C and D it is slightly smaller.

As it can be seen the volume of the proposed model B is include between the figuring conicoid and conic patch one. In fact the differences between the proposed model and figuring conicoid and Hermans one have opposite sign as it is possible to see in figure 2b and 2c. It is interesting to consider that these three models have the same geometrical constraints.

In the other cases the volume of the proposed model it is slightly smaller than the two conics, the hyperbolic cosine model and the Fourier series model.

Tabella 4.9 Volumes of the analysed models

Model	Volume [mm^3]
Model A	160.21
Two conics	163.30
Figuring conicoid	159.07
Model B	160.30
Conic patch	165.48
Model C	155.96
Hyperbolic cosine	159.25
Model D	131.99
Fourier series	139.04

Figure 4.3 shows the trends of the radius of curvature along the lens profile of the models. The curves are plotted against the y direction, anterior part of the lens from 0 to R_{eq} and posterior one from R_{eq} to 0.

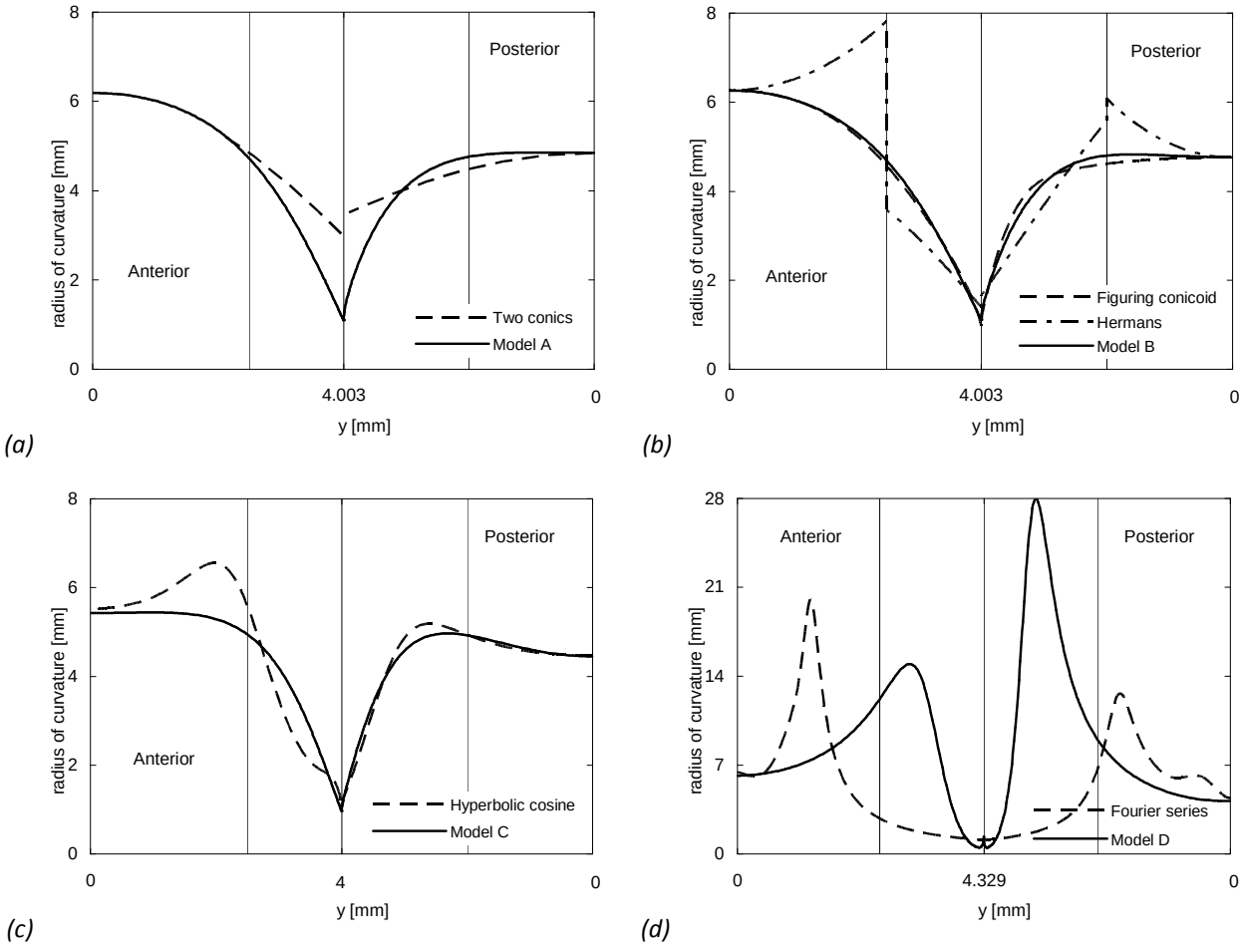

Figura 4.3 Radius of curvature of the proposed model against four models, plotted versus y direction, anterior part of the lens is on the left side from 0 to 4, and posterior one is on the right part from 4 to 0. (a) Proposed Model A against two conic; (b) Proposed Model B against figuring conicoid and conic patch (Hermans) model; (c) Proposed Model C

against hyperbolic cosine (Kasprzak) model; (d) Proposed Model D against 10th–order Fourier series (Urs) model. Vertical lines stand for anterior optic zone, equatorial junction and posterior optic zone from left to right.

In figure 4.3a the radius of curvature of the two conics model is plotted against the proposed Model A. It is possible to see that the first one has a discontinuity radius at the equatorial plane, as expected, while the second one has the same curvature in the junction zone. Both the models have radii very closed in the anterior optical zone, while in the posterior optical zone the proposed model has a radius slightly larger and stationary.

In figure 4.3b are plotted both figuring conicoid and conic patch model against the proposed Model B; as previously said, all this models have the same geometrical constraints and are consequently depicted in the same figure.

The conic patch model radius presents a discontinuity at every patch junction. In particular we can see that the highest jumps occur from the optical zones to the junction zones. Moreover the radius of curvature in the optical zones increases very quickly from the optical axis to the junction zones due to the high negative conic constant value.

Both the figuring conicoid and the proposed model are continuous in curvature and in the optical zones (underlined by vertical lines at 2.5 mm for anterior and 2 mm for posterior part) the radius of curvature is very close with differences less than 3% for anterior optic zone and less than 10% for posterior optic zone; the posterior optic zone has a trend that is flatten then the figuring conicoid.

Hyperbolic cosine model (figure 4.3c) present lower apex vertex curvature then the other models, this result is consistent with one found by Smith et al. In this case, the Model C is really close to the hyperbolic cosine one in the posterior optic zone with a difference lower than 2%.

The 10th–order Fourier series model (figure 4.3d) presents some problem of stability during the circular fitting process. For the other four literature models and the presented model the circular fitting process was applied over a range of 10 points centred on the local point, even with the minimum number of 3 points for the interpolation they already presents no problems, the total number of point per model in this stage of analysis was reduced to 500 just to let the method be faster in calculation without loosing validity.

On the other hands the number of points used during the circular fitting process for the Fourier series was of 100 points over 500 points of the total curve. The value of curvature presented then in figure 4.3d may not be considered then a real local curvature rather an average curvature.

4.2.2. Proposed model against shadow-photogrammetry imaging

The proposed is compared against shadow-photogrammetry imaging provided by R. Urs and F. Manns of the Ophthalmic Biophysics Center, Bascom Palmer Eye Institute, University of Miami Miller School of Medicine, Miami, USA, testing shape, volume and curvature.

The images referred to three lenses relevant to a 20, 42 and 63 year old in vitro lens. Here we give a brief summary of the original technique used by Urs et al. (2009) to acquire lens image.

Lenses were imaged using the technique of shadow-photogrammetry (Augusteyn et al., 2006; Denham et al. 1989; Pflugfelder et al., 1992; Rosen et al., 2006; Urs et al., 2009). The shadow-photogrammetric system consists of a modified optical comparator (BP-30S, Topcon, Tokyo, Japan) with two light sources to enable photography of the crystalline lens in the coronal and sagittal planes. A 20x magnified shadow of the excised lens is projected onto a viewing screen and images are captured by a 4.0 Mp Nikon Coolpix 4500 digital camera (Tokyo, Japan) positioned at a fixed distance from the screen. For scaling purposes a ruler (1376T-25, Keuffel and Esser Co., Hoboken, New Jersey) was concurrently photographed on each image (figure 4.4).

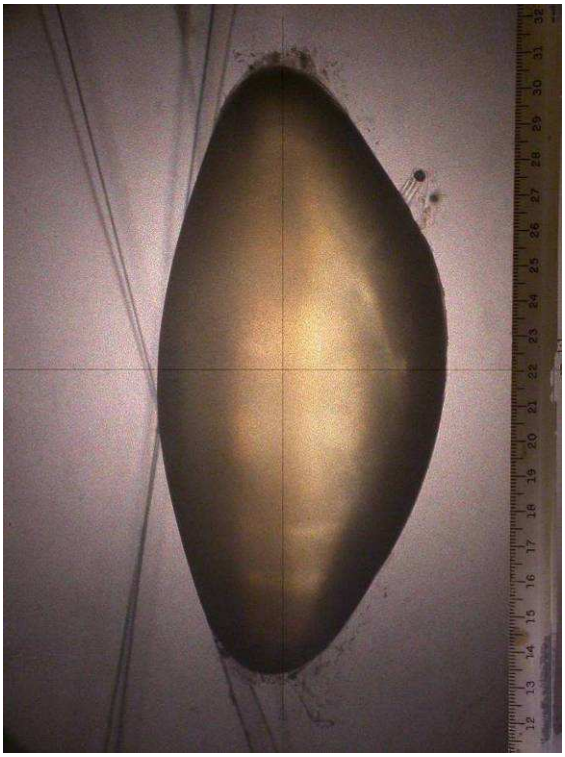

Figura 4.4 Human crystalline lens of 42 year old men acquired by shadow-photogrammetry imaging

The flow chart of figure 4.5 summarises the step by step procedure used for the acquisition and modification of the contour of the lens before the analysis.

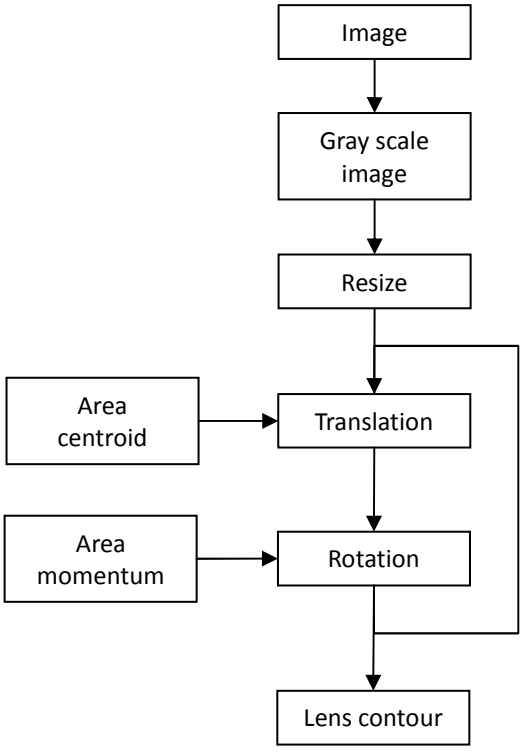

Figura 4.5 Lens contour preparation scheme before the analysis

From the original image given by Urs a gray scale gif image was created with Paint Shop Pro (Jasc Software), the gif image was loaded into Mathcad (Parametric Technology Corporation). The image was then cropped to remove the ruler. To detect the lens contour a Canny filter was used with standard deviation sigma value of 3 and hysteresis thresholds of 5 and 10, to detect a fine contour of the lens. A few false contours that were detected were removed manually. Mathcad output gives pixels position of the contour of the lens.

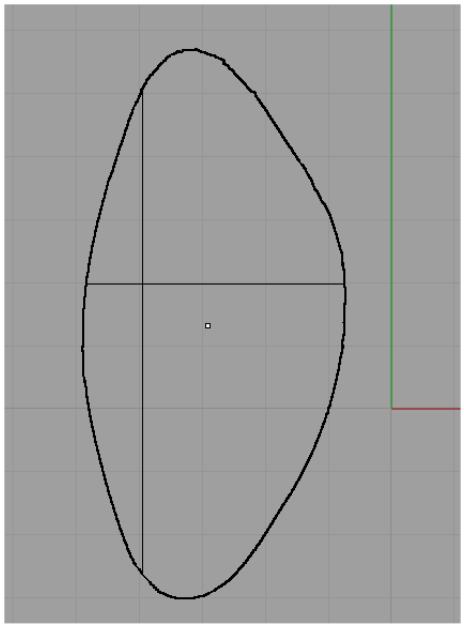

Figura 4.6 Human crystalline lens contour imported into Rhinoceros. It can be seen that the contour is not place in the origin, the point indicate the centre of the lens

Data were loaded into Rhinoceros and resized using the pixel to pixel distance of the ruler (figure 4.5).

An approximate centre for the lens was determined by the internal area centroid built-in function, and the image was corrected for decentration error so that the centre is translated in the origin. Using the built-in area momentum a matrix was created which elements are defined as:

$$M = \begin{bmatrix} M_{zz} & M_{yz} \\ M_{yz} & M_{yy} \end{bmatrix} = \begin{bmatrix} \int z^2 dA & \int yz dA \\ \int yz dA & \int y^2 dA \end{bmatrix} \qquad (4.23)$$

where M_{zz} and M_{yy} are the second momentum of the area respect to z and y, and M_{yz} are the product momentum, and the M matrix represent the plane in respect to the yz plane.

The matrix of the eigenvectors of the momentum matrix is the rotation matrix ROT, so that the product between the non-rotated contour (z, y) and the rotation matrix give the lens contour (x', y'):

$$\begin{bmatrix} z' \\ y' \end{bmatrix} = ROT \cdot \begin{bmatrix} z \\ y \end{bmatrix} \qquad (4.24)$$

The process is repeated until the value of M_{yz} that represent the rotation between the yz-plane and the y'z'-plane is less then 10^{-5}. Remaining decentration errors were finally correct so that the equator stands between peaks to peaks in y direction.

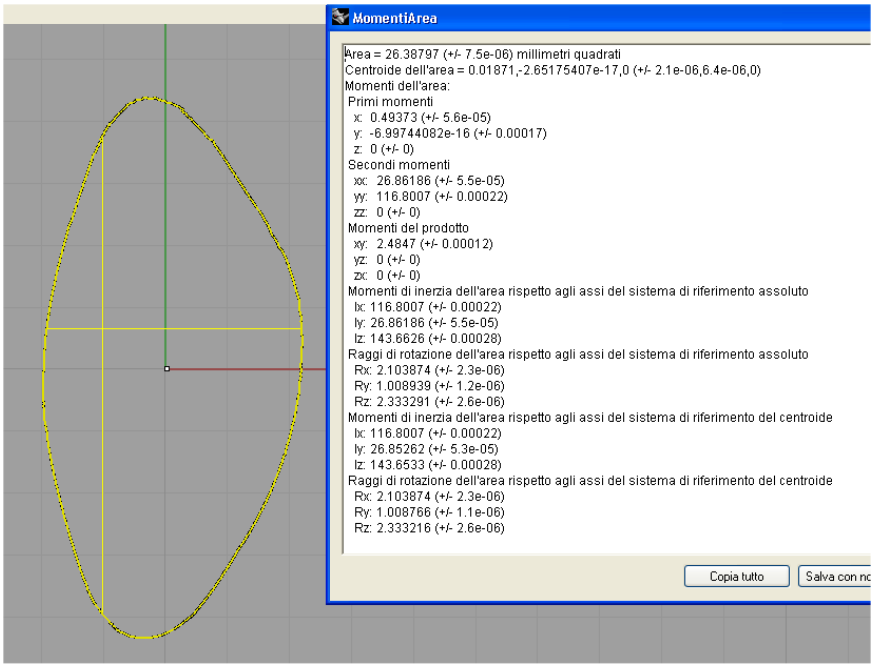

Figura 4.7 Rhinoceros output of area momentum analysis during the rotation process

The process is done for the three shadow-photogrammetry images of 20, 42 and 63 year old human crystalline lens, from the lens image geometrical constraints are calculated directly in the CAD using point to point distances to find anterior, t_a, and posterior, t_p, length and equator radius R_{eq}.

For the optical constraints a fitting process was used. Over a defined diameter a conics was fitted on the lens contour using a least square method. In particular was used the MATLAB built-in function that use the Levenberg-Marquardt algorithm (Levenberg, 1944; Marquardt, 1963; Dennis, 1977; Moré, 1977) which solves nonlinear least squares curve fitting problems of the form

$$\min\left\|f(r,q)\right\|_2^2 = 0 \qquad (4.25)$$

as MATLAB optimization toolbox explains, with this method is possible to evaluate the anterior and posterior radius, R_a and R_p respectively, and asphericity coefficient, q_a and q_p respectively. Data for both geometrical and optical constraints are summarised in table 4.10.

Tabella 4.10 Constraints adopted to define the shape of the lens adopting the proposed model, to compare it with the other models mentioned in the first column (values in mm).

Lens countour	R_a	R_p	q_a	t_a	t_p	t	R_{eq}
20	7.207	– 4.884	– 2.862	1.580	2.465	4.045	4.447
42	8.877	– 5.968	– 1.477	1.908	2.377	4.285	4.662
63	14.015	– 6.327	2.8	1.869	2.646	4.515	5.108

The shape of the proposed model is compared with the 20, 42 and 63 year old lens contour, plotting above the lens profile the magnified normal deviation. To summarize this results it was adopted the merit function proposed in Smith et al., which is the sum of the square error evaluated along the normal to the lens profile of the proposed model.

The merit function was performed in the optical zones, in the junction zones and in all the lens profile. Moreover, maximum and average distances between models are calculated.

A solid of revolution was created and then the volume is assessed. The radius of curvature was

calculated using the method presented in chapter 3 and it is plotted against the radial y–axis.

4.2.2.1. Results

Figure 4.8 shows the results of the normal deviation, with its sign, of the proposed model fitted on different age lens contour, magnification is 20 times. It can be seen that, 20 year old and 42 year old contours are fitted better then 63 year old contour, if we do not consider the red zone in the 20 year old model that should be arise from an error in the Canny filter the maximum deviation is lower 0.06 mm over the two contours.

The 63 year old model presents much more deviations then the other two with a maximum deviation of 0.175 mm. This may arise due to contour that is less clear then the other models, and also the fact that there are imbalances between the superior and inferior parts of the lens. The superior one presents less deviation then the inferior one. Further investigations have shown that the difficult in the contour evaluation with Canny filter may introduce errors during the rotation of the lens, leading to imbalances and fitting errors.

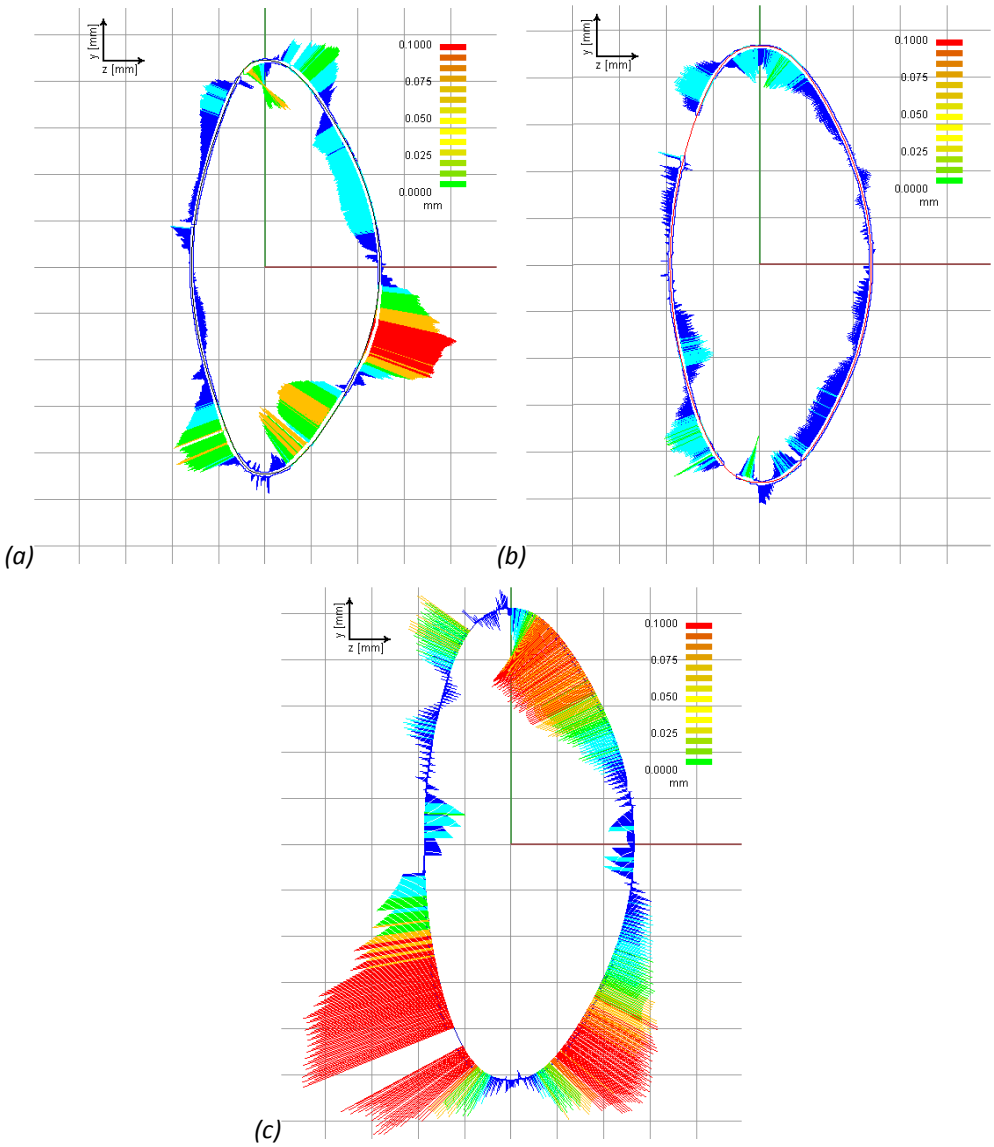

Figura 4.8 Comparison between the shape of the proposed model and different lens contours (a) 20 year old, (b)42 year old, (c) 63 year old. The normal distances between the models, magnified 20 times, are depicted above the profile of the proposed model.

Looking at the anterior (|y|< 2.5 mm) and posterior (|y|< 2 mm) optic zone (the y amplitude is selected following the work of Hermans et al., 2009) we can see that the proposed model is very close to both the 20 and 42 year old with deviations of the order of 10^{-5}, for the 63 year old model the deviation is one order more.

From an optical point of view this means that the proposed model is close to fitting conics in both the anterior and posterior optic zone leading to a situation where there optic difference between the proposed model and the standard conics model is not as high as it will be seen in the next chapter.

In table 4.11 the deviations between the model and the lens contours are quantitatively summarized by the merit function for the whole lens and for its portions, together with the maximum and the average distances. Analysing this results similar conclusion can be drawn:

- the merit function between the proposed model and the 42 year old lens contour is the least in all the profile, and in the different sections except the anterior optic zone,
- the merit function between the proposed model and the 20 year old lens contour is the least in the anterior optic zone,
- the merit function assumes highest values in all the profile and in all the sections between the proposed model and the 63 year old lens contour,
- average and maximum deviations confirm that the proposed model fits better over the 42 year old lens contour, so mid-age lens, then the other extrema age lenses.

Tabella 4.11 Merit Function, maximum and average deviation of the proposed model against the lens contours. In addition to results for the entire lens profile, the values of merit function in anterior optic zone (z<0, y<2.5 mm), posterior optic zone (z>0, y<2 mm), and the two junction zones are shown.

Lens countour	Merit function [mm^2]					Max deviation [mm]	Average deviation [mm]
	Anterior optic zone	Anterior junction zone	Posterior junction zone	Posterior optic zone	All profile		
20	$1.70 \cdot 10^{-5}$	$2.89 \cdot 10^{-4}$	$3.25 \cdot 10^{-4}$	$6.69 \cdot 10^{-4}$	$4.41 \cdot 10^{-4}$	0.092	0.0259
42	$7.44 \cdot 10^{-5}$	$1.33 \cdot 10^{-4}$	$9.20 \cdot 10^{-5}$	$2.00 \cdot 10^{-5}$	$1.16 \cdot 10^{-4}$	0.051	0.0145
63	$5.88 \cdot 10^{-4}$	$3.17 \cdot 10^{-3}$	$5.26 \cdot 10^{-4}$	$8.08 \cdot 10^{-5}$	$1.50 \cdot 10^{-3}$	0.175	0.0475

In table 4.12 are summarised data for the volumes of the lenses. As it is expected the volume grows from the 20 year old lens to the 63 year old lens contour. Comparing the data of table 4.12 against the data of the 7 year old lens models of table 4.9 it can be seen that the 7 year old model presents an average volume of 160 mm^3 that is between the 20 year old and the 42 year old lens contour.

Tabella 4.12 Volumes of the analysed lens contours

Lens countourl	Volume [mm^3]
20	149.44
42	184.75
63	245.36

This should be explained since the original data come from different authors, Jones et al., 2007, for the 7 year old models and Urs et al., 2009, for the lens contours, so that different imaging techniques may introduce some differences in the raw data. Looking at table 4.10 and 4.8 it can be

seen that the major difference is in the thickness of the lens, which for the 7 year old lens does not follow any growth rule. It is known that the thickness of the lens may change due to the process done on the lens after it is taken out from the cadaver, and it is also relied on the time between one step of the process and another one.

Figure 4.9 shows the trends of the radius of curvature along the lens profile of the models. The curves are plotted against the y direction, anterior part of the lens from 0 to R_{eq} and posterior one from R_{eq} to 0.

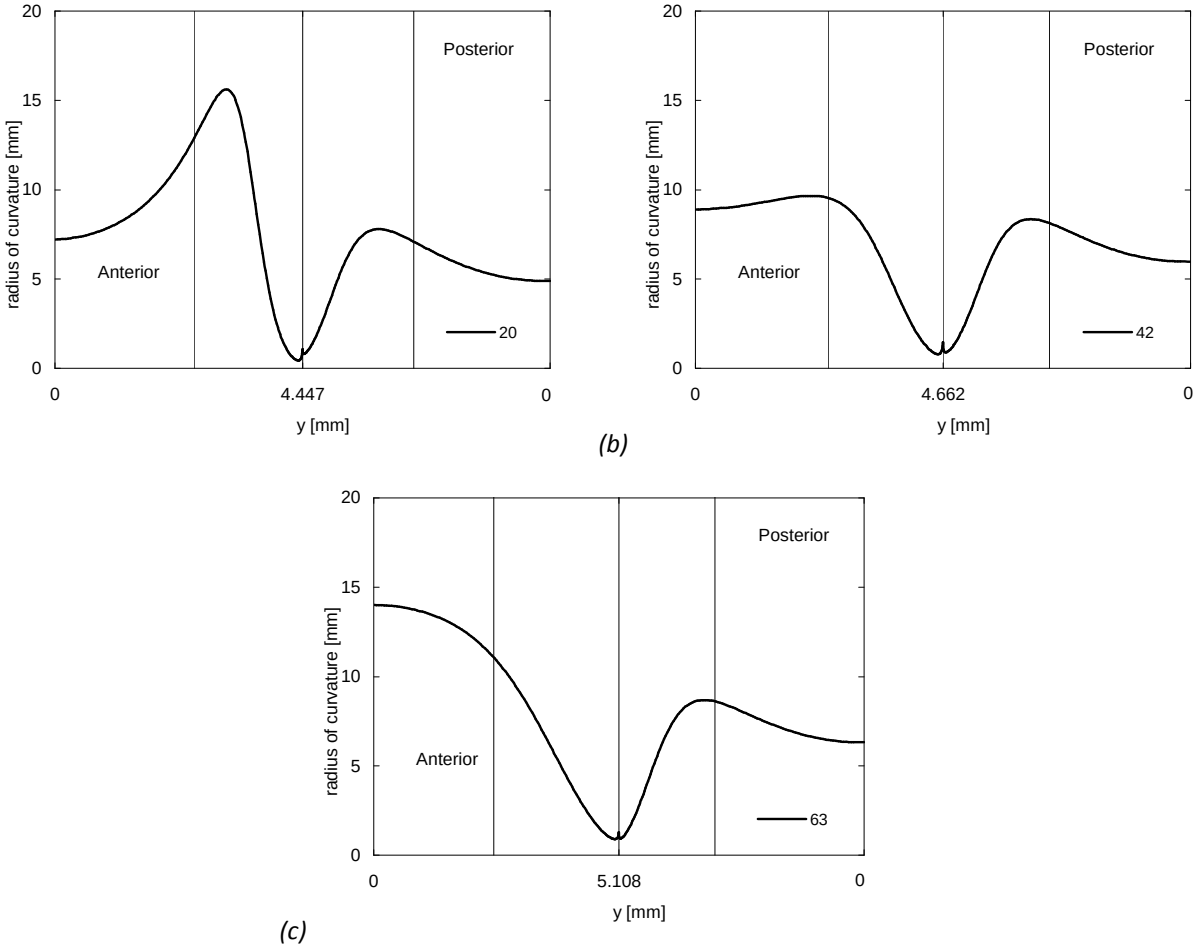

Figura 4.9 Radius of curvature of the proposed model fitted over three lens contours, plotted versus y direction, anterior part of the lens is on the left side from 0 to 4, and posterior one is on the right part from 4 to 0. (a) Proposed 20 year old lens contour; (b) 42 year old lens contour; (c) 63 year old lens contour.

In figure 4.9a the radius of curvature of the 20 year old lens contour is plotted. It is possible to see that the anterior part shown an asphericity value higher then the posterior part, using formula (22) for the posterior part will lead to an asphericity value of $q_p = -1.256$.

In figure 4.9b the 40 year old lens contour radius of curvature is higher both in anterior and posterior part but it can be seen that except for the anterior part the shape of the curvature does not completely change. In fact the anterior asphericity, which drive most the curvature in the optic zones, changes from – 2.862 to – 1.477 but the posterior asphericity does not present a substantial difference, $q_p = -1.402$, the change is about 11%.

According to the literature the anterior and posterior radius of curvature increases also in figure 4.9c that show the radius of curvature of the 63 year old lens contour. The interesting thing is again

the shape of the curvature which from the anterior junction till the posterior optic zone remains as previous cases.

The posterior asphericity in the last case is $q_p = -1.246$ which present a difference of less the 1% with the 20 year old lens. So according to the shape of the three curvatures we can say that the curvature at the equator does not show sensible differences, the same does the asphericity coefficient. Much difference instead arises on the anterior surface. As last data the optical power of the lens of the three ages is provided in table 4.13, this was calculated using 1.42 as lens refraction index and 1.336 as surrounding media index and using formulas provided in paragraph 2.2.10:

Tabella 4.13 Vertex power for the three lens contour

Lens countourl	Power [D]
20	29.42
42	23.94
63	19.49

This data are in agreement with radius founded by Urs et al. (2010) and so to vertex power. From this data the lens paradox that Brown (1974) and Dubbelman and Van der Heijde (2001) found does not arise. With lens paradox we mean that lens radius decreases with age so that the power of the lens increases, against the total power of the eye that decrease, and this is the well known hyperopisation through age. Of course we would like to remind that the set of data presented here is not as extensive as other studies in the literature.

4.3. Discussion

Several simple models such as circular, parabolic or conic sections are usually adopted to describe the surfaces of the human crystalline lens and to study the optical properties of the lens (Smith et al., 2009, Glasser and Campbell, 1999; Atchison, 2006; Dubbelman, 2005).

These models are often adopted when the data are derived by in vivo Scheimpflug imaging in which the equatorial radius cannot be measured. In this models the conic coefficients are strongly related to the geometrical and optical properties, but they not provide a continuous junction between the anterior and the posterior surface of the lens and than they are not qualify for biomechanical simulation.

Vice versa, more complex mathematical models such as augmented conic equation (Pierschionek and Chan, 1989), figuring conicoid (Smith, 2003), generalized conic (Kasprzak and Iskander, 2006), conic patch (Hermans et al., 2006; Hermans et al., 2009), polynomial (Urs et al, 2009), Fourier series (Urs et al., 2010), modulated hyperbolic cosine (Kasprzak, 2000) and other curves which involve polynomial and trigonometric function (Chien et al., 2003), where the coefficients involved are typically derived by fitting techniques, give a continuous junction between the anterior and the posterior surface, but do not provide a geometrical or optical interpretation of the coefficients of the model.

In this chapter it was proposed a continuous curvature lens model in which the coefficients are derived by geometrical and optical constraints. In this way, both the continuity in the junction zone and a geometrical–optical interpretation of the coefficient involved in the model are obtained.

More in details all the coefficients of the mathematical model have been derived by thickness, equatorial radius and curvature radius lens geometrical characteristics, which are strongly linked to the shape and to the optical properties, and is not necessary to perform any further numerical

optimization to find the coefficients. Moreover it is always possible to change the parameters in a fast and intuitive way to change the lens shape.

It is known that these set of parameters change along with age (Dubbelman, 2001; Schachar, 2004; Rosen et al., 2006) so the proposed lens model can be easily applied to age–dependence analysis, as it was shown applying the model to different age lens contour.

Moreover these set of parameters change according to accommodation power and again applying functions that explain these changes (Rosen et al., 2006; Hermans et al., 2009) the model can be easily applied to accommodation analysis.

By MRI imaging data (Jones et al., 2007; Kasthurirangan et al., 2008; Hermans et al. 2009), or shadow photogrammetry (Urs et al., 2009) all the constraints can be directly derived from the image. Another common technique that can be applied to derive the parameters necessary to the proposed model are the Scheimpflug imaging (Dubbelman and Van der Heijde, 2001; Dubbelamn et al., 2002; Rosales et al., 2006; Hermans et al. 2007), in which the equatorial radius and the ratio between anterior and posterior thickness are not given; this parameters can be found in the literature (Rosales et al., 2006).

Both the techniques can be used in vivo measurement, but it must take into account the method selected for the radius of curvature estimation, which are typically derived by fitting schemes that involve different equation and different dimension of the lens profile.

Geometrical behaviours of the model are in good agreement with the other ones described in the literature as can be seen in the results. In particular the merit function MF (Smith et al., 2009) against other models are very little especially in the optic zones of the lens. The merit function in the optic zone against real lens contours is higher, as expected, but the value is comparable with other studies in the literature. The best results for the anterior and posterior optic zone were in the mid-age 42 year old lens contour.

The major differences can be seen in the junction zone, where the proposed model has a smoother curvature radius. Over all the profile the presented model is close to the figuring conicoid model (Smith, 2003) with a MF of $4 \cdot 10^{-5}$ mm^2 and a mean distance less than 5 μm.

Radius of curvature shows a similar trend; these circumstances signify that the model is able to evaluate the optical properties. In particular it has been seen from the lens contour that the posterior radius of curvature, that is the one that drive more the optical properties of the lens remain quite stable over different ages while is the anterior radius of curvature that change much more.

Several studies proposed finite element analysis in order to study the accommodation under ciliary muscle stress (Hermans et al., 2006; Abolmaali and Schachar, 2007). In this case the models adopted must have a continuous shape as the proposed one.

The volume of both the lens and the nucleus is evaluated in the accommodation analysis (Hermans et al., 2006; Hermans et al., 2009). In particular the volume of the presented model is between the figuring conicoid model (Smith et al., 2009) and the Hermans et al. (Hermans et al., 2009) patch model.

The presented model can also be applied to the nucleus shape modeling. Taking data from Hermans et al. (2008) it was found a MF for the whole profile equal to $2.2 \cdot 10^{-4}$ mm^2 and to $2.7 \cdot 10^{-4}$ mm^2 relevant to a lens nucleus respectively of a 11 year old and 29 year old (the shape of the nucleus is described in Hermans et al. (2007)). Consequently this model can be used in the analysis of the growing patterns of nucleus and cortex.

In future improvement of the proposed model, the coefficients will be derived from more imaging data of different age crystalline lenses. Also the internal structure of the lens shall be taken into account for optical analysis such as optical power and spherical aberration. To this aim, interesting GRIN model closed linked to the external shape of the lens is the one proposed by

Navarro et al. (Navarro et al., 2007(a); Navarro et al., 2007(b)), or a shell model by Campbell (2010), or aging GRIN models (Goncharov and Dainty, 2007, Diaz et al., 2008) that can be used to characterised the internal structure of the lens and finally to create a complete eye model as close as possible to the real eye structure.

Chapter 5. Virtual eye: modeling and analysis in a 3D environment

This section describes the construction of a computer model of the human eye in a CAD environment. The purpose of this virtual eye is to analyze and simulate the optical properties of the eye as well as each of its optical elements. The computer technical implementation of the optical components is described. Using measured biometric geometry of human eyes an individual virtual eye can be constructed.

5.1. Modeling environment development

As it has been said we decided to use Rhinoceros as CAD environment to develop the virtual eye model. This ambient is chosen since it is possible to use built-in functions and scripts to create plug-in thought for optical design that are not embedded in any CAD itself. The choice of a CAD is made since this environment is able to work with surface mathematically defined, with clouds of points and with meshes.

This is very important if onethink that the input data from which create a virtual eye may arrive from different sources, such as topography image of the cornea or MRI imaging of the lens, but every input sources can be transformed into a could of points that a CAD can easily manage.

Our work is then to create simple plug-in for a CAD that can be also exported for other CADs, in which the mathematical kernel is the same, and to validate our method with simple eye models and with real eye data.

The simple scheme to create a virtual eye can be seen in the following figure:

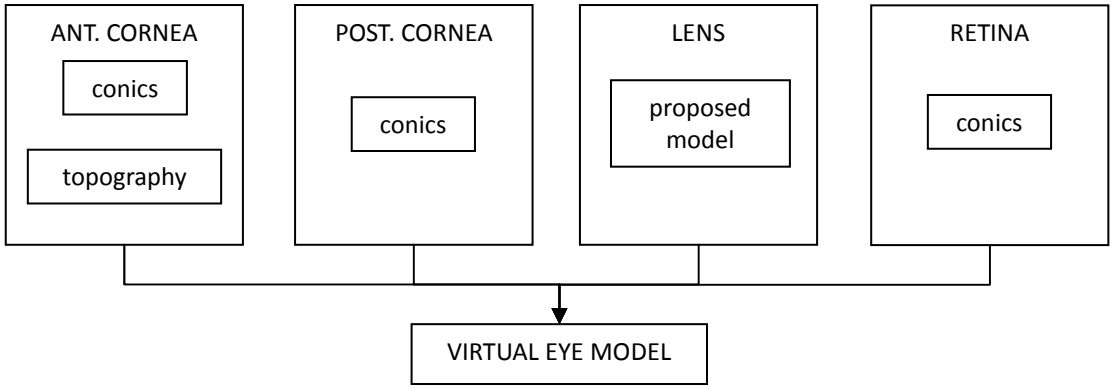

Figura 5.1 Virtual eye model scheme

5.1.1. Anterior cornea

The anterior cornea is the dominant refracting surface of the human eye. For the virtual eye, this surface can either be a theoretical model surface or it can be based on measured patient data, usually from topography data. In both case the value of the index of refraction of the cornea is taken as the accepted value 1.376.

5.1.1.1. Model

The simplest mathematical function used for modelised the anterior cornea surface is the conicoid. In this kind of CAD is possible to define in a 2D plane (e.g. y-z plane) the conicoid curve defined in a script by the equation

$$z = \frac{y^2}{r + \sqrt{r^2 - (1+q)y^2}} \qquad (5.1)$$

in which the radius of curvature r and the asphericity coefficient q can be defined by the user.

Table found in the previous chapter can be used to define the average radius and asphericity parameters, or can be found with a keratometer, an instrument that gives an average value for r by real data. Data from eye models can be also found in the literature and will be used to test the virtual eye in the following parts.

Once a curve in a plane is drown, it is possible to create a cloud of points by letting the curve round across an axis of rotation (z-axis). From the cloud of points in a 3D space is now possible to create surfaces or meshes using built-in functions of the CAD (figure5.2).

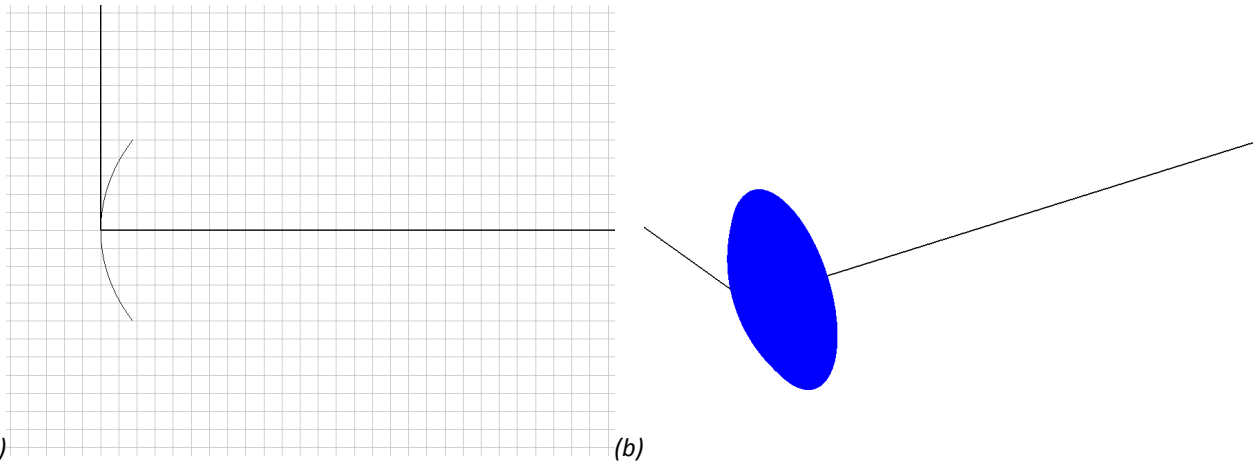

(a) (b)

Figura 5.2 (a) Anterior cornea model in 2D plane, (b) and rendering in 3D after revolution

Since the surface is created by the revolution of a curve it will not have any toricity as the real cornea has, but at the best of our knowledge the majority of eye models found in the literature are rotationally symmetric, so our first step is to let our models be rotationally symmetric as well, so is possible to compare data.

To let the mathematical model introduce toricity is possible to use biconic functions

$$z = \frac{\frac{x^2}{r_x} + \frac{y^2}{r_y}}{1 + \sqrt{1 - \frac{(1+q_x)x^2}{r_x^2} - \frac{(1+q_y)y^2}{r_y^2}}} \qquad (5.2)$$

where r_x and r_y are the radius of curvature in the x (sagittal) and y (tangential) direction, and q_x and

q_y are the asphericity coefficients associated to the radius of curvature. In this case is possible to create a cloud of points directly in the 3D space.

5.1.1.2. Topography

The anterior cornea can be alternatively constructed from measured data from topography measurements. Common to all topography systems using Placido rings is the analysis of the ring positions from the centre of the topography along meridians. In this thesis, data from Optikon Keratron was used (figure 5.3a).

This system uses 256 meridians (1-degree steps) and analyzes 30 respectively 32 ring edges. The raw measurement data of the corneal elevation is thereafter given as values at discrete measurement positions, aligned along meridians and imported into the CAD as shown in figure 5.3b.

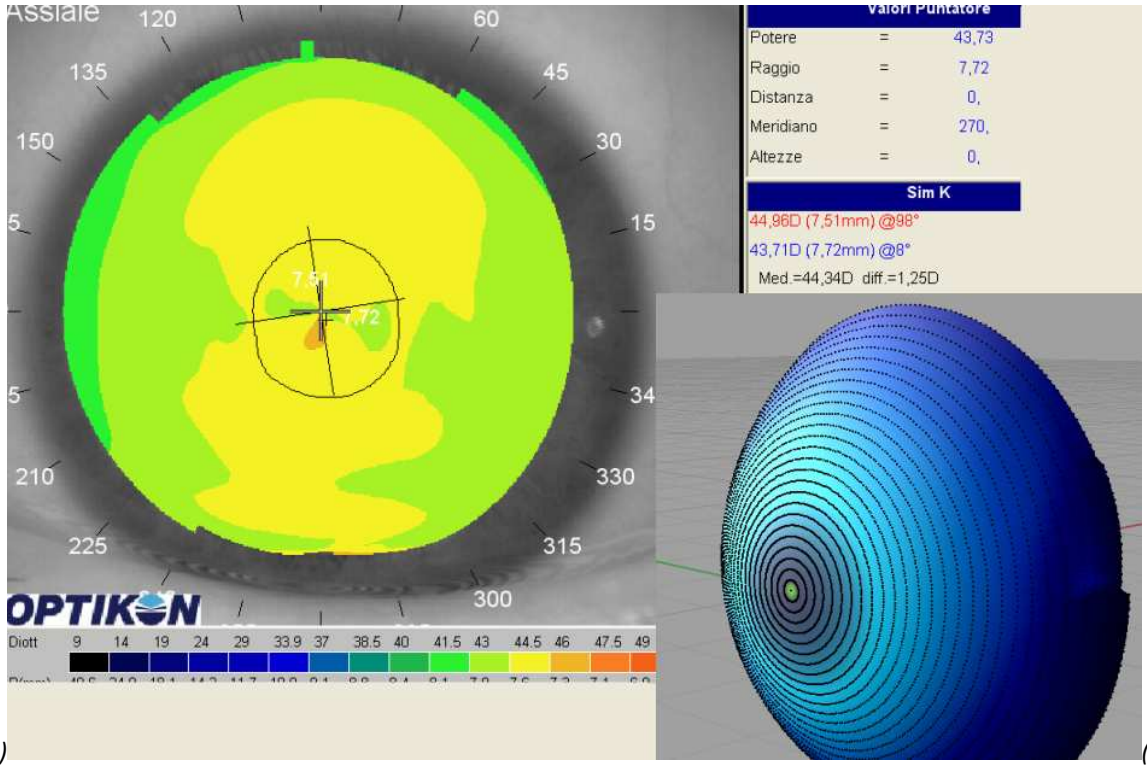

(a) *(b)*

Figura 5.3 (a) Topographer output data and visualization of elevation map in dioptres, (b) import of elevation map into Rhinoceros

For the ray-tracing procedure is needed to interpolate the cloud of point with a surface or a mesh as it is already explained for the layer described by mathematical functions in chapter 3. In figure 5.3.b can be seen not only the cloud of point imported into the CAD but also the mesh (in blue) added to the cloud itself using a Delaunay method.

5.1.2. Posterior cornea

Even if as seen in the previous chapter the posterior cornea has less effect on the overall refraction of the eye it cannot be neglected. In the virtual eye, it is modeled just as the anterior cornea as a conicoid which radius is 1:0.81 of the anterior radius (figure 5.4). If the cornea data are imported by a topographer the posterior cornea radius is taken as a ratio of the mean anterior radius.

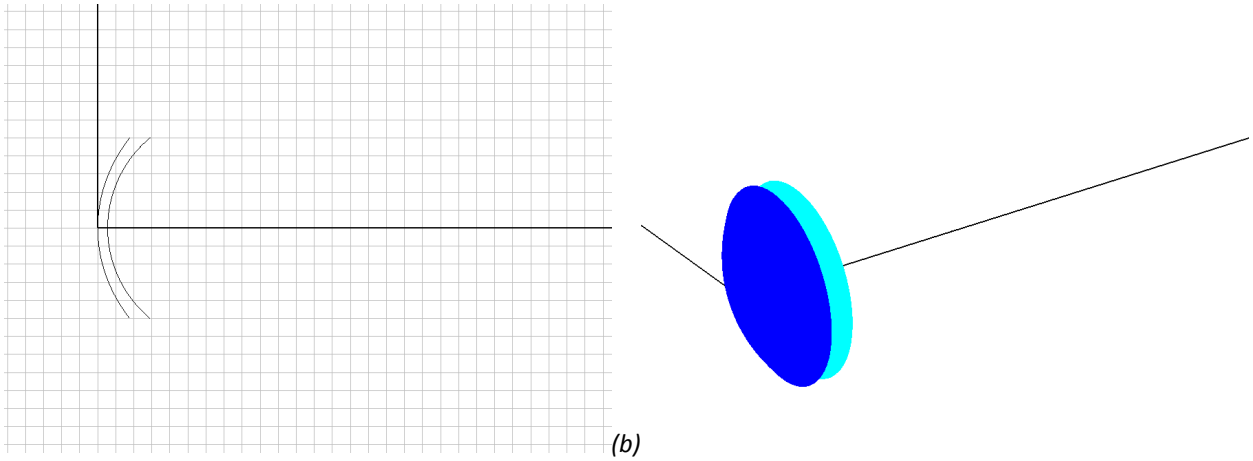

(a) (b)

Figura 5.4 (a) Anterior and posterior cornea model in 2D plane, (b) rendering in 3D after revolution

Asphericity coefficient is taken as a first stage zero and it may be adjusted after the first ray-trace to fit the aberration of the whole eye. The thickness of the cornea is taken 0.55 mm. And the vitreous humor refraction index is taken 1.3374. These data are generally accepted by the scientific community and used also in other eye models.

5.1.3. Lens

For the virtual eye model presented in this thesis the lens is modelised using the proposed model reviewed in chapter 4. To let the virtual eye model to be compared with other eye models the constraints used for assessing the coefficients may change (figure 5.5).

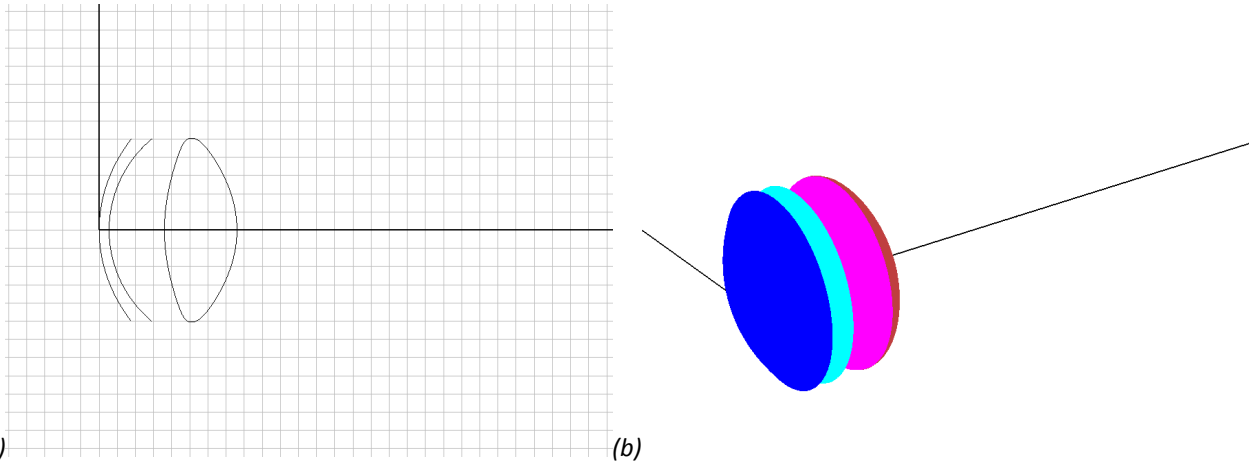

(a) (b)

Figura 5.5 (a) Anterior cornea, posterior cornea and lens model in 2D plane, (b) rendering in 3D after revolution

In any case the anterior and posterior radius, the asphericity coefficient and total thickness of the eye model are taken as input data for the virtual eye model. If the diameter of the lens is available by the eye model it is used as input data. Generally for anterior posterior thickness ratio is taken the value 1:0.7 (Dubbelman et al., 2001), or 1:0.6 (Navarro et al., 1985), even if the first value is preferable. The distance between the posterior apex of the cornea and the anterior apex of the lens is usually taken as 3.05 mm.

It must be taken into account that the lens radius, thickness and diameter may change according to age and accommodation level. Again we refer to the eye model input data to compare the virtual eye with the selected eye model.

If instead real image of the lens are available all the input data are taken from the image itself as explained in the previous chapter.

As for the previous refractive surfaces the model in 2D are then rounded on the z-axis to create the cloud of points and then surface or mesh.

The refraction index of the lens is taken constant at this stage. This is a great simplification for the ray tracing even if is far away from a real model of the eye, but at this stage we think that a further complication of the model due to the GRIN is not necessary since we would like to test the virtual eye model both against simple eye models, the Navarro one especially, which use as well homogeneous refractive index. Future works will add a GRIN model to the presented lens model.

5.1.4. Retina and Sclera

Retina is the imaging surface of the eye. It is modelised as Kooijman (1983), Navarro (1985) and Atchison (2006) model eye as an aspheric surface. Again in the CAD it is defined in a 2D plane (e.g. y-z plane) the conicoid curve defined in a script by the equation 5.1 in which the radius of curvature r is taken as – 12 and the asphericity coefficient q may be changed by the user. We will see in further part of this thesis the effects of q over the imaging spot.

Sclera is the outer part of the eye, it is not a refractive surface so it model does not affect the aim of the present thesis, but it is important if the effects of the outer forces on the eye must be studied. Sclera is taken as a curve offset out of the retina with a distance from the original surface of 0.5 mm as in Norrby (2005).

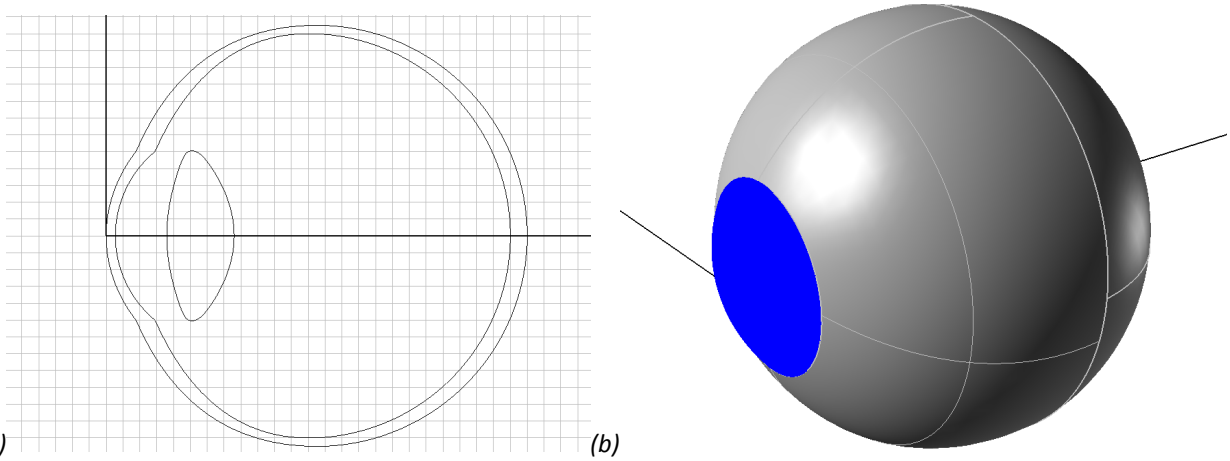

Figura 5.6 (a) Virtual eye model in 2D plane, (b) rendering in 3D after revolution, only the posterior half of the retina is depicted to show the internal parts of the eye.

5.2. Virtual eye model: Navarro et al.

In this section the CAD design of the Navarro et al. (1985) eye model is presented. This is a well known eye model which has important characteristics:

- cornea and retina are modelised as spherical surfaces,
- posterior cornea, anterior and posterior lens surfaces are modelised as aspherical surfaces
- it implement accommodation into the model, even if for the aim of the present thesis the accommodation is taken 0 D, so we consider the relaxed eye,
- the lens is modelised with an homogeneous refraction index,

In further articles (Navarro et al., 2007a; Navarro et al., 2007b) introduce a GRIN model of the

lens index; the aim of this thesis is to analyse first the CAD design of the original model, and test how the substitution of the proposed lens model, and of real corneal topography affect the optical behaviour of the virtual eye. Future works will implement the GRIN model already developed by Navarro et al. into the CAD environment.

Tabella 5.1 Navarro et al. model data used for the modelisation of the virtual eye

Medium / Surface		n @ 589.3 nm	r [mm]	q [mm]	t [mm]
Air		1			
Cornea	Anterior	1.376	7.72	– 0.26	0.55
	Posterior		6.5	0	
Aqueous		1.3374			3.05
Lens	Anterior	1.42	10.2	– 3.1316	4
	Posterior		– 6.0	– 1	
Vitreous		1.336			16.40398
Retina			– 12	0	

Table 5.1 summarises the geometrical and optical data used for the selected eye model. Using the method presented above the figure 5.7 depict the Navarro virtual eye model into the CAD.

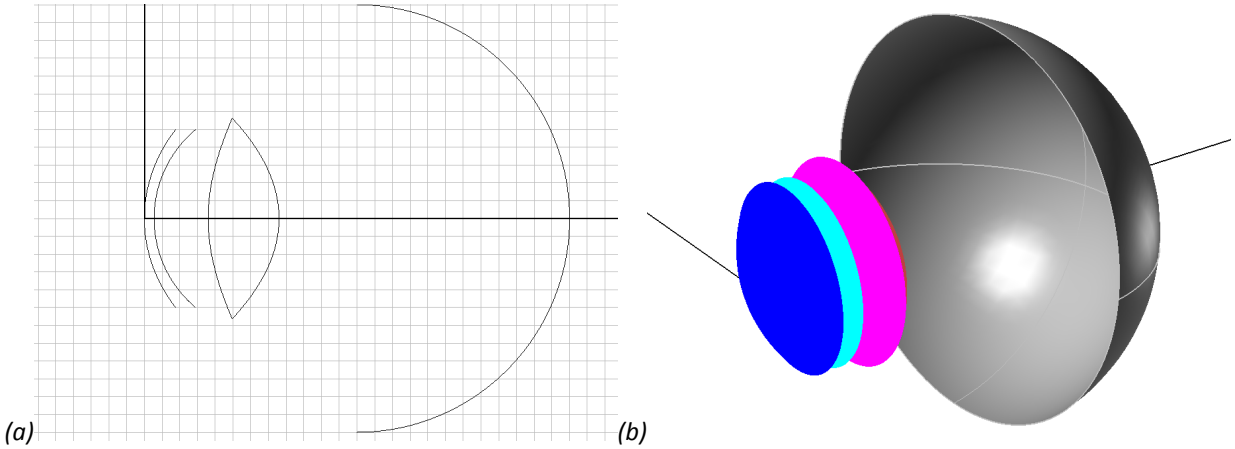

(a) *(b)*

Figura 5.7 (a) Navarro eye model in 2D plane (b) rendering in 3D after revolution, only the posterior half of the retina is depicted to show the internal parts of the eye

As it can be seen in figure 5.7 the model uses two conics surface for the crystalline lens and it was already said in chapter 4 the junction between anterior and posterior part is not smooth.

The total power of the lens is of 60.416 D, with 42.882 D given by the cornea and 21.779 D by the lens.

5.3. Virtual eye model: proposed model lens

The first modification introduced to the original model is to substitute the crystalline lens with the proposed model lens. The constraints used for the assessment of the coefficients are the same

used for the original lens and can be found in table 5.1.

As it can be seen there are two missing data: the ratio for anterior/posterior thickness from which the respective thickness can be found, and the equatorial radius. In following works Navarro et al. suggest for the anterior/posterior ratio a value of 0.6. Even if the works of Dubbelman and Van der Heijde suggest a higher value of 0.7 the first value has been taken, just to follow the original author's work.

For the equatorial radius instead Navarro does not provide any value neither in following works. In figure 8 of Navarro et al. (2007a), here reported in figure 5.8, it can be seen the longitudinal spherical aberration, LSA, for different age of the lens contour, it can be seen the original work line, in dashes, fits the 82 year old line. Using Urs et al. (2010) growing model a value of 5.044 mm is then founded and used for the equatorial radius of the lens.

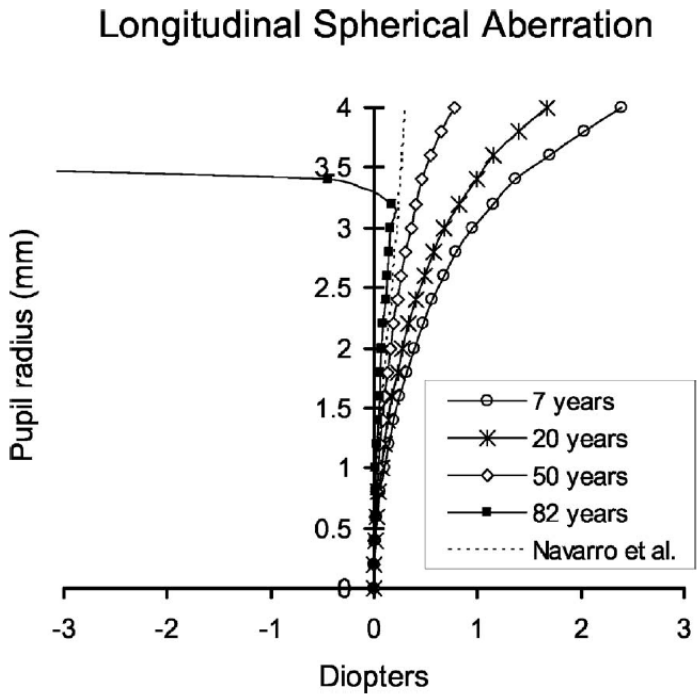

Figura 5.8 Change of the longitudinal LSA with age for Howcroft and Parker conic constants ($q_a = -3.1316$, $q_p = -1$). The dashed curve represents the homogeneous lens model of Navarro et al. There is a clear trend of a monotonic decrease of SA with age (Navarro et al., 2007a)

In figure 5.9 can be seen the Navarro model with the substitution of the crystalline lens with the proposed model one. In particular in figure 5.9a both the lenses are depicted. As it can be seen the proposed model lens fits very well the original one.

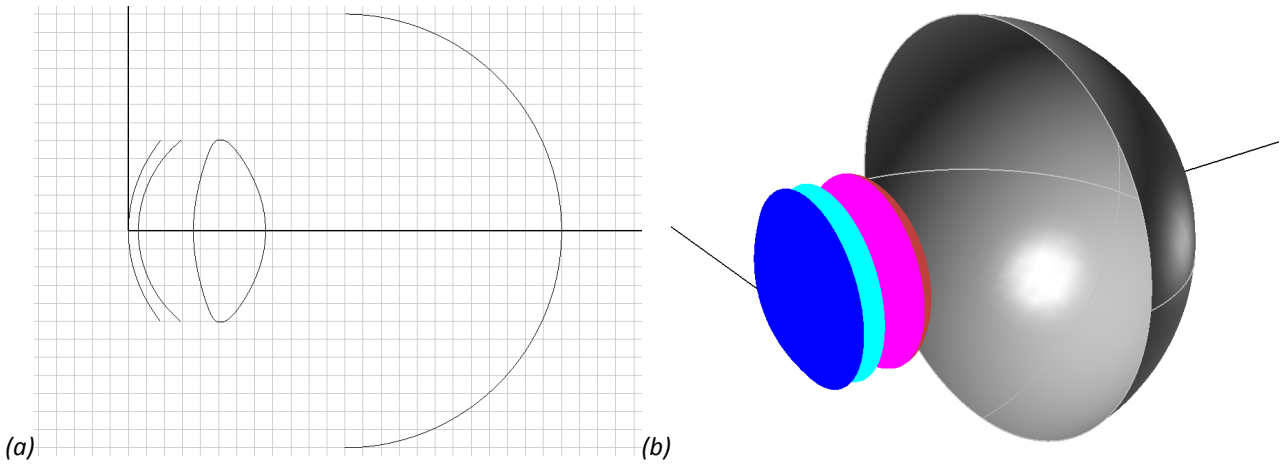

Figura 5.9 (a) Virtual eye model in 2D plane, (b) rendering in 3D after revolution, only the posterior half of the retina is depicted to show the internal parts of the eye

A series of analysis has been developed to test the proposed model against the original one. Since both models are rotationally symmetric some of the analyses are performed only in the tangential y-z plane.

For the 2D surface on-axis spherical aberration is calculated using the ray-trace method explained in chapter 3.

For off-axis analysis using the circular fitting method or the curvature formulas founded in chapter 1 and 4, the tangential radius of curvature of the lens contour was found and compared with the two conics surface radius. Sagittal radius of curvature was found using formulas already provided in chapter 1 and with the Coddington's law astigmatism, tangential and sagittal powers are calculated and compared.

For 3D ray tracing analysis the spot of confusion method explained in chapter 3 was used both on the original model and on the proposed one.

5.3.1. Longitudinal spherical aberration

The longitudinal spherical aberration is an on axis optical analysis realised with ray tracing technique. A pencil of rays parallel to the optical axis (z-axis) is refracted by the different layers of the eye. The interception of these refracted rays with the optical axis gives the position of the object image. The differences between the vertex ray and the other rays are plotted against the (pupil) height (see chapter 3 for more details).

In figure 5.10 the LSA for every different components of the eye, cornea and lens, is plotted. Both the Navarro original lens and the proposed model one are plotted. The indexes of refraction used in the analysis are listed in table 5.1.

As it can be seen the lens presents in both cases a positive LSA against the negative one of the cornea. This means that the distance between the image point and the vertex of the refracted surface tends to reduce for the cornea, and tends to increase for the lens. This different behaviour of the two surfaces is in agreement with data found in the literature (Navarro et al., 1985).

Moreover the combined effects of cornea and lens tends to cancel each other, that is desired effect since if the LSA would be zero all along the pupil radius this means that all the rays will focus in one point, e.g. the fovea.

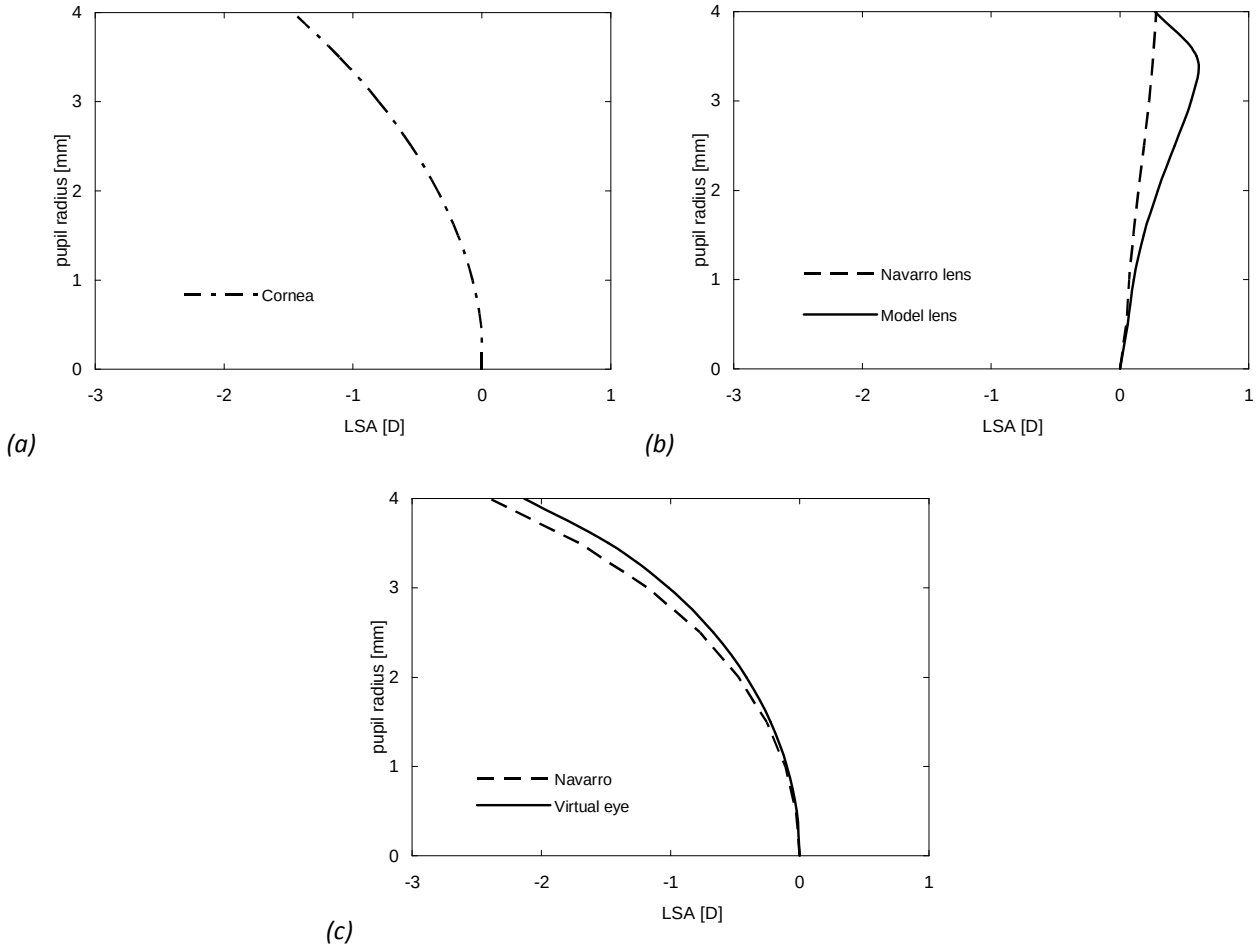

Figura 5.10 (a) Longitudinal spherical aberration, LSA, of the cornea; (b) LSA for Navarro lens model and proposed lens model; (c) LSA for the Navarro eye model virtual eye model

In figure 5.11 is plotted the total eye LSA. Both the original Navarro model and the model with the proposed lens are analysed. Also for the total eye the LSA was calculated into the eye, as it is done for the single elements analysed before. This is was done according to the work of Navarro et al. but differ from other works such as Atchison et al. who usually perform an out of the eye ray trace.

It can be seen how the most spherical aberration is due to the cornea surface since as for the power the abrupt jump in the index of refraction from 1 in air to 1.3374 for the cornea produces the main change in the ray path. For the vertex ray, which it is not refracted, the focal length is equal to the total length of the eye 20.00398 mm, which correspond to 0 D in figure 5.11, and the other data are founded as aberrations (so differences) of length in dioptres.

The virtual eye model with the substitution of the original lens with the proposed model lens will produce a lower LSA then the original Navarro eye model. At 4 mm pupil radius the LSA is equal to – 2.16 D against – 2.40 D for the Navarro model.

5.3.2. Radius of curvature

It was already discussed in chapter 1 the curvature of aspheric surfaces. The results founded in that chapter are used to find the curvature of the anterior and posterior cornea surfaces. In figure 5.10 are reported the tangential curvatures for both the surfaces till a height y of 5 mm.

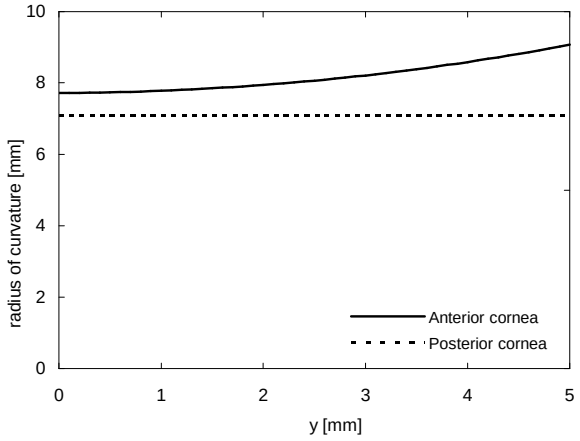

Figura 5.11 Radius of curvature of the anterior and posterior cornea surface plotted versus y direction

As it can be seen the anterior cornea, which have a negative asphericity coefficient, increase the radius of curvature along the y direction, instead as obvious the radius of curvature for the posterior cornea remain the same since the asphericity coefficient equal to zero provide a circle curve.

Using formula 4.8 for the proposed model and 2.5 for the Navarro's two conics model, which lead to the formula already reported in chapter 2 for the radius of curvature of aspheric curves, we are able to find the tangential curvature for the two different lens profiles. The same results may be reached using the circle fitting method if the two models are provided as a series of points. In figure 5.11 are plotted the radius of curvatures of both models.

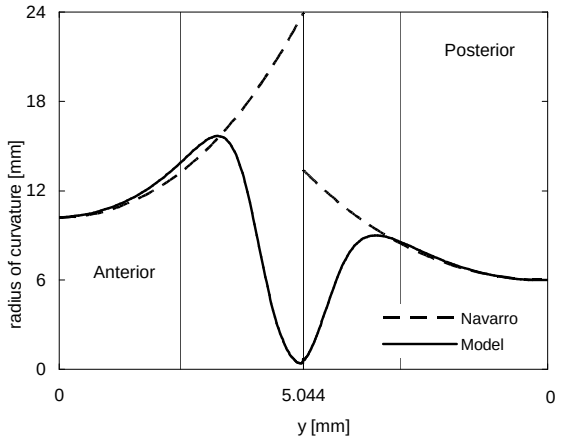

Figura 5.12 Radius of curvature of the proposed model against Navarro model, plotted versus y direction, anterior part of the lens is on the left side from 0 to 4, and posterior one is on the right part from 4 to 0.

From the figure it can be seen that the proposed model fits very well the two conics model, in particular in the anterior optic zone the deviation is of 0.424 μm ($1.80 \cdot 10^{-7}$ mm^2 in terms of the merit function as in the previous chapter) and for the posterior optic zone the deviation is of 0.223 μm ($4.98 \cdot 10^{-8}$ mm^2 in terms of merit function). As it was already seen in the previous chapter, the posterior asphericity, calculated from the lens model of – 1.231, is close to the value of – 1 that is the real value of the conic.

For evaluating the optical characteristics of the virtual eye model, in particular power and

astigmatism, not only the tangential radius of curvature is needed but also the sagittal one.

In the original work of Navarro all the surfaces are conics so, as seen in chapter 2, the sagittal radius of curvature can be found from the tangential one known the vertex radius as in Martin's formula (1961) so that $r_s = \left(r^2 \cdot r_t\right)^{1/3}$ this is not valid for any parametric surface.

The tangential radius of curvature can be derived in the range $0 \leq u \leq \pi$ adopting the equation (2.6) founded in the chapter 2. The circular fitting method, developed and explained in chapter 3, may also be used to find the curvature if the parameter u is discrete and the curve is given as a collection of points. All the radii of curvature, $r_{t,a}(u)$ and $r_{t,p}(u)$ for the anterior and the posterior part, are assumed positive to maintain consistency with the proposed equations.

The method explained in chapter 2 to find the tangential curvature of parametric surface may be also applied to find the sagittal curvature; more details can be found in appendix B. Using this method after some passages the following equation can be found for the tangential and sagittal radius:

$$r_t = \frac{\left[\left[\left(b_0 + b_1u^2 + b_3u^4\right)\sin u - 2\left(b_1u + 2b_3u^3\right)\cos u\right]^2 + a^2\cos^2 u\right]^{3/2}}{a\cdot\left[b_0 + b_1u^2 + b_3u^4 + 2\left(b_1u + 2b_3u^3\right)\cos u\sin u - 2\left(b_1 + 6b_3u^2\right)\cos^2 u\right]} \qquad (5.3a)$$

$$r_s = \frac{a\sin u\cdot\left[\left[\left(b_0 + b_1u^2 + b_3u^4\right)\sin u - 2\left(b_1u + 2b_3u^3\right)\cos u\right]^2 + a^2\cos^2 u\right]^{1/2}}{\left(b_0 + b_1u^2 + b_3u^4\right)\sin u - 2\left(b_1u + 2b_3u^3\right)\cos u} \qquad (5.3b)$$

where the coefficients a and b_i are referred to the anterior part in the range in the range $\pi/2 \leq u \leq \pi$, and to the posterior part in the range $0 \leq u \leq \pi/2$.

If the parameter u is discrete the quadratic fitting method, explained in chapter 3, can be used to find the curvature. Both calculi give the same results.

In figure 5.14 are shown the sagittal and tangential radius for the proposed lens surface.

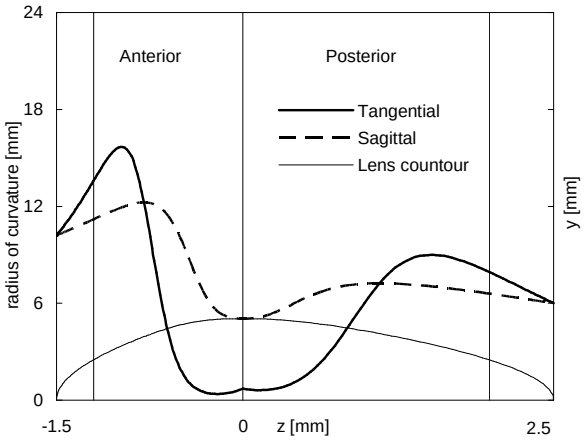

Figura 5.13 Sagittal and tangential radius of curvature plotted against the z axis; anterior part of the lens is on the left side from – 1.5 to – 1.2, and posterior one is on the right part from 2 to 2.5. The lens contour is also plotted

As it can be seen in the optic zone the sagittal radius is lower then the sagittal one and is close to the value founded as it is a conicoid, so using the Martin's formula. This is an expected trend since as seen in chapter 4 the proposed model fits well conics especially in the optic zones.

5.3.3. Power and astigmatism

As seen in chapter 1 for an aspheric surface Coddington's equations can be used to find the sagittal and tangential power of the optic system. From these data can be found the mean power

and astigmatism, which are fundamental for the analysis of ophthalmic surfaces as well of a virtual eye.

For Coddington's equations the incoming and outgoing angles, i and i', are instead found using ray tracing tools developed for CAD as seen in chapter 3. Figure 5.15 shows the results of sagittal and tangential power errors for Navarro eye model and the virtual eye with the proposed lens model used for the crystalline against angles of incident in air.

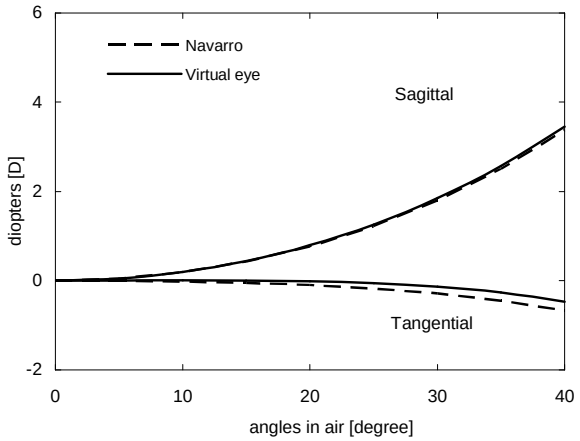

Figura 5.14 Sagittal and tangential power errors of Navarro eye model and the virtual eye model with the proposed lens substitution.

Data are in good agreement with the one presented by Atchison et al. (2000). As it can be seen the sagittal power error is higher for the virtual eye compared with Navarro eye model with a difference at 40° of 0.08 D. The tangential power error instead is lower for the virtual eye compared with Navarro eye model, and at 40° the difference in absolute terms is of 0.20 D. In figure 5.16 the power errors are summarised in a single value the mean power error.

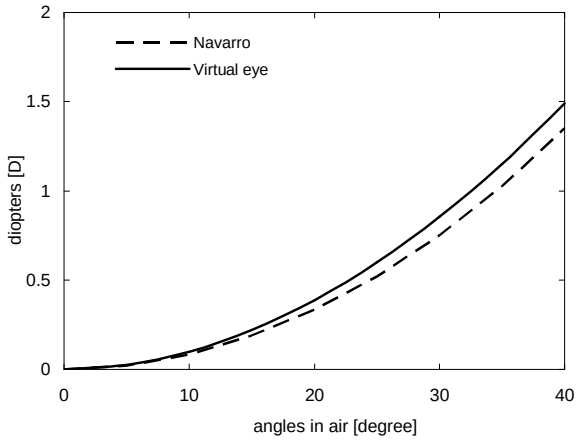

Figura 5.15 Mean power of the Navarro eye model and the virtual model with the proposed lens substitution

The mean power data are in good agreement with the data of Bakaraju et al. (2008) who analyse different eye models, and also the Navarro one, with a Zemax commercial program. The difference between the Navarro model and the virtual eye is of 0.14 D the fact that the virtual eye is close to the Navarro model could be interesting due to the fact that usually with the introduction of a GRIN model the power error tends to decrease and to be more similar to the physiological

values. If the power error is already lower then the GRIN introduced in the model can be of lower values and less important in the model itself. It must be remind already that GRIN models for the crystalline lens are subject of research in the community.

Figure 5.17 presents the astigmatism for the Navarro eye model and the virtual eye model. The plot is in good agreement with data presented by Atshison et al. (2000) and Bakaraju et al. (2008). And moreover they are in good agreement also with mean physiological data of real eyes.

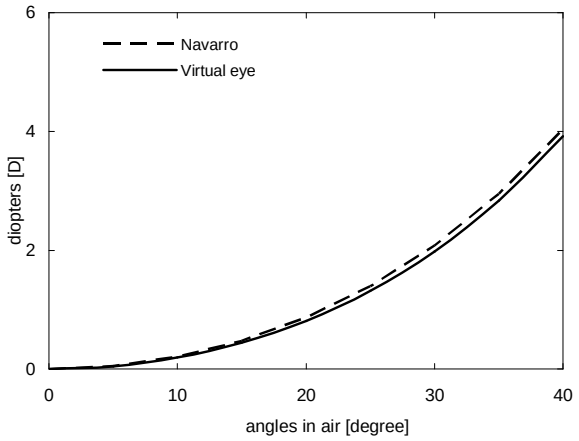

Figura 5.16 Astigmatism of the Navarro eye model and the virtual model with the proposed lens substitution

5.3.4. Spot of confusion

As it has been said in chapter 2 another method to analyse the optical systems, already integrated in the analysis of ophthalmic surfaces by the DAUR-LIN group, is the analysis of the spot of confusion. In the CAD environment using the method developed and explained in chapter 3 it is immediate to evaluate the intersections between the refracted rays and the retina surface.

The basis ray pattern is formed by 4 rings within a diameter of 8 mm with a distance from ring to ring of 1 mm. In every ring the number of rays varies from ring to ring but the distance between ray and ray within the ring is taken constant and equal to 1 mm.

Figure 5.18a represents the ray path into the eye as seen in Rhinoceros. The spots on the different layers are the interception point at which the refraction occurs. The little area on the retina, which is set transparent to better see the ray path, are the interception points that form the spot of confusion. Figure 5.18b presents data for the spot of confusion of the Navarro eye model and the virtual eye model.

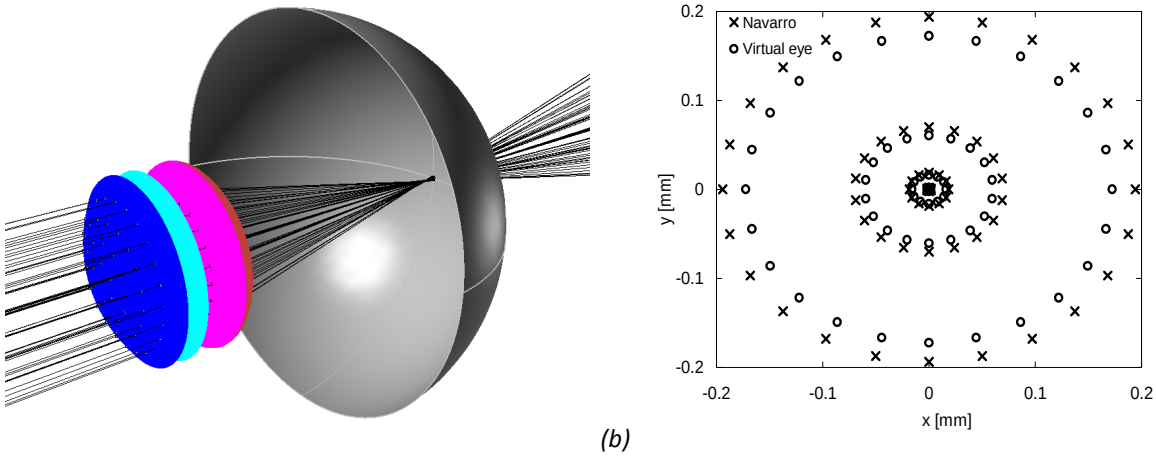

(a) (b)

Figura 5.17 (a) Parallel rays refracted into the virtual eye mode, (b) spot of confusion for the Navarro eye model and the virtual eye model

As it can be seen the spots for the virtual eye model are closer to the centre then the Navarro eye model spots. This means that the aberrations introduced by the virtual eye model, moreover the proposed model lens, are lower then the aberrations of the Navarro eye model. This is a good behaviour of the virtual eye model but it must be taken into account that the aim of the virtual eye model is to reproduce the performance of a real eye so aberrations are wanted in the model.

Tabella 5.2 Centre, standard deviation and area of the spot of confusion for the Navarro eye model and the virtual eye model

Model	Centre [mm]	Standard deviation [mm]	Area [mm^2]
Navarro	(0,0)	0.0786	0.1182
Virtual eye	(0,0)	0.0702	0.0934

Table 5.2 collects the data derived from the spot of confusion. Since both the models are created as rotation symmetry along the z-axis the centre is exactly in the origin of the xy-plane. As it was seen from the figure both standard deviation and area of the virtual eye spot of confusion are lower then the Navarro model.

5.4. Virtual eye model: corneal topography

As it is said in paragraph 5.1 the anterior cornea surface of the virtual eye can be derived from literature data that usually gives the average radius of curvature in one or both sagittal and tangential direction.

Another method to derive anterior cornea data is from commercial topographer. Ing. G. Guerra of Naturalens s.a.s., Padova, Italy, has gently provides us the output data of the Optikon 2000 S.p.A., Roma, Italy, Keratron topographer. The output raw data and the imported data into the CAD can be seen in figure 5.3.

Since the real cornea layer can be modelised as a free form surface, in which as seen in chapter 3 it can be defined a local curvature which required an accurate analysis, at this stage was decided to first analyse the spot of confusion that arise from the ray tracing of the virtual eye model with the substitution of the anterior cornea with the topographer data.

In table 5.3 the data used for the virtual eye are collected. It must be taken into account the topographer give data for the average radius was of 7.72 mm at 8° so the posterior corneal radius was taken as the ratio 1:0.0842 of the anterior radius, as in Navarro model. The lens is modelised with the proposed model, and since both the cornea radii are as Navarro model also the crystalline lens was taken as the same. It must be said that the age of the amethrope of which the topography is referred to was not provided. As well the retina is taken as in the original virtual eye analysed in the previous paragraph.

Tabella 5.3 Virtual eye model data used for the modelisation in the 3D environment

Medium / Surface		n @ 589.3 nm	r [mm]	q [mm]	t [mm]	R_{eq} [mm]
Air		1				
Cornea	Anterior	1.376	Topographer data		0.55	
	Posterior		6.5	0		
Aqueous		1.3374			3.05	
Lens	Anterior	1.42	10.2	– 3.1316	4	5.044
	Posterior		– 6.0	– 1		
Vitreous		1.336			16.40398	
Retina			– 12	0		

In figure 5.19 are depicted the 2D and 3D view of the virtual eye with the topographer corneal data. In particular in figure 5.19a it can be seen the clouds of points taken as raw data from the output of the topographer. In figure 5.19b instead the clouds of points is fitted with a NURBS surface.

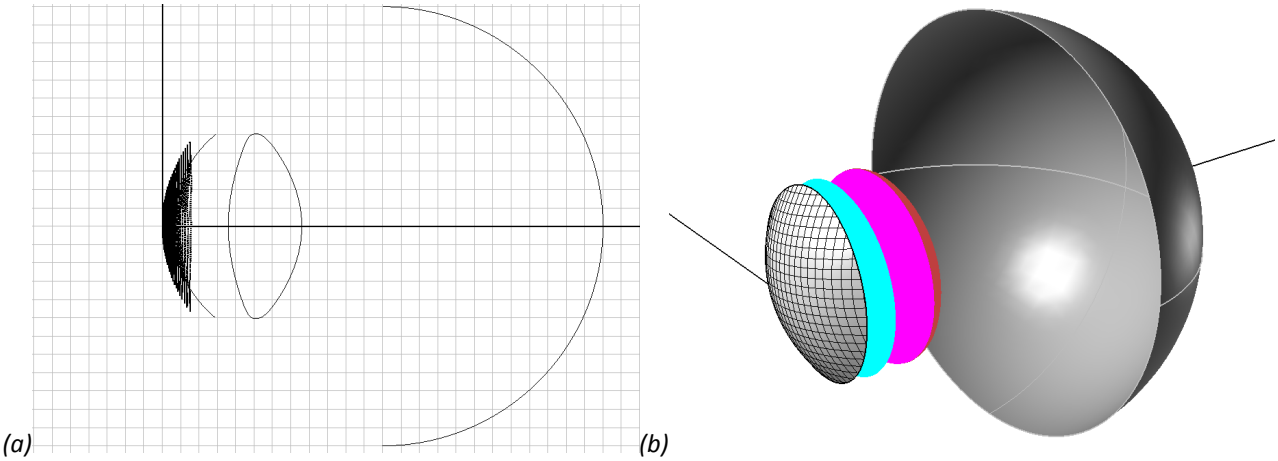

(a) *(b)*

Figura 5.18 (a) Virtual eye model with the substitution of the anterior cornea with cloud of points as taken from the topographer, in 2D plane, (b) rendering in 3D after revolution, only the posterior half of the retina is depicted to show the internal parts of the eye, the anterior cornea was modelised as NURBS surface.

For the NURBS is chosen the patch command of Rhinoceros which need as input data the average distance between points in the cloud of points and the number of subdivision in u and v direction of the parameterization, data used for the creation of the NURBS are reported in table

5.4.

Tabella 5.4 Data used for the NURBS creation

	Point distance [mm]	Subdivision in u	Subdivision in v
NURBS surface	0.31	50	50

The standard deviation of the clouds of points from the NURBS surface is of $8.089 \cdot 10^{-5}$ mm, or $6.543 \cdot 10^{-9}$ mm^2 in terms of merit function. It was chosen the NURBS due to the better results against the mesh during the ray trace, in particular some problems of tolerances arises during the calculus of the interceptions between the ray and the mesh.

Once the anterior cornea surface was substituted with the real cornea data a ray trace was performed. The basis ray pattern is formed by 4 rings within a diameter of 8 mm with a distance from ring to ring of 1 mm. In every ring the number of rays varies from ring to ring but the distance between ray and ray within the ring is taken constant and equal to 1 mm. Interceptions between the refracted rays from the posterior lens surface and the retina surface are calculated. In figure 5.20 the data are plotted in xy-plane forming the spot of confusion at the retina.

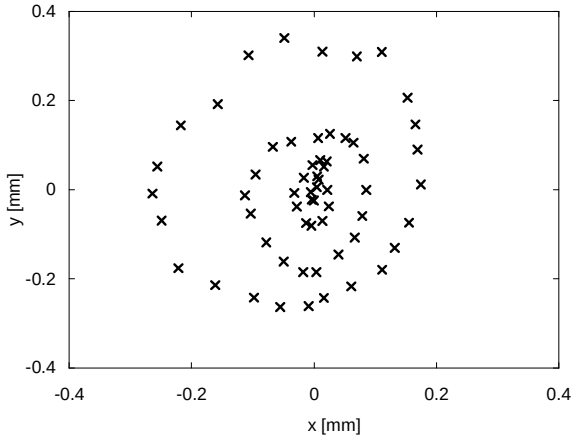

Figura 5.19 Spot of confusion for the virtual eye model with the substitution of anterior cornea with data from topographer

It can be seen that the 4 rings does not maintain their shape with much more distortion as much the ring increase it height value. Table 5.5 summarises the data for the virtual eye with the substitution of the anterior cornea surface.

Tabella 5.5 Centre, standard deviation and area of the spot of confusion for the virtual eye mode with the substitution of anterior cornea with data from topographer

Model	Centre [mm]	Standard deviation [mm]	Area [mm^2]
Topography	(–0.0092,0.0003)	0.1807	0.1834

There is an imbalance in the centration of the rings which centre is no more in the origin but it changes of 0.3 μm in positive y direction and of 9.2 μm in negative x direction.

It is interesting to point out that, if the fovea in the model eye is considered to be on-axis, it seems that the image formed with the real cornea presents a good centration in y direction, on the

other hand the image it is not centred in x direction. This kind of decentration can be explained with fixation imbalances during the topography.

Furthermore the area of the spot of confusion double it size in the virtual eye model from the original one, with a value of 0.0934 mm^2, to 0.1834 mm^2 after the substitution of the anterior corneal surface.

5.5. Discussion

Paraxial eye models (Gullstrand et al., 1909; Le Grand and El hage, 1980; Blaker, 1980; Rabbett and Bennett, 1998) and many finite eye models (Lotmar, 1971; Kooijman, 1983; Navarro et al., 1985; Thibos et al., 1997; Norrby, 2005) are usually defined as conics in the plane and to create the complete model the model is rotated along the z-axis. This permits optical analysis with simple calculus and even if the known toricity of the eye is not taken into account, these eye models are very important for the development of later eye models.

More complex models (Liou and Brennan, 1997; Atchison, 2006; Goncharov, 2007; Navarro, 2007a and 2007b) introduce non rotational surfaces and GRIN lens and are usually analysed in horizontal and vertical plane, which present different optical behaviours.

These eye models use modern imaging techniques, such as Sheimpflug lamp (Dubbelman et al., 2002), video-keratography (Atchison, 2006), magnetic resonance (Jones et al., 2005), shadow photogrammetry (Urs et al., 2009), to collect data for the different layers of the eye.

Such images are not usually integrated into a CAD but are fitted by simple conics curves, and are not used to create 3D image.

In this chapter were presented methods to import, modify and analyse with ray-tracing techniques, the output of such imaging tools into a CAD program.

More in details it were used Rhinoceros programmable scripts to define a plug-in that is able to create a virtual eye model formed with conicoid for anterior and posterior cornea surface and retina, the proposed lens model presented in chapter 4 and then rotated along the optical axis, and is also able to substitute the anterior cornea surface with data coming from topography, but also other surfaces if imaging data are available. Other plug-ins were created to analyse such virtual models and are successfully used to trace rays through the eyes.

At this stage the plug-in is able to trace ray through homogeneous index media so it was decide to compare Navarro et al. (1085) eye model and virtual eye model based on this eye model with the modification of the crystalline lens.

Different ray tracing set up are used for the analysis: rays parallel to the optical axis are traced and on axis interceptions are evaluated to analyse the longitudinal spherical aberration; rays parallel to the optical axis are traced and interception with the retina layer are evaluated to analyse the spot of confusion; and rays at different angles respect to the optical axis are instead traced to evaluate sagittal and tangential power errors with the use of Coddington's equations.

As it was seen in the previous chapter the shape and curvature of the presented lens model is close to the two conics shape of the Navarro et al. eye model, if this is true for the optic zone that for the anterior part of the lens is about 2.5 mm in height and for the posterior part of the lens is 2.0 mm in height, this may not be true out of these zones.

In particular it was analysed the spherical aberration for the two eye models till a radius of 4 mm in height and it was seen that the virtual eye model presents an higher value of LSA for the lens then the original model so that the total LSA of the lens is lower, due to the fact that the lens is able to counter act the effect of negative cornea LSA.

It must be said that both the models are characterised by an homogeneous index of refraction,

this for sure is not consistent with the physiological index distribution of real crystalline lens but it is a well known approach to model eye analysis, and a basis step for future works that will integrate GRIN models (Goncharov and Dainty, 2007; Navarro et al., 2007a and 2007b) into the proposed lens model. It was known that such GRIN models are able to modify the lens LSA making it much more positive especially for high values of incident rays height. This should lead to an overall improvement of the virtual eye model making the total LSA more close to physiological l data.

Another data that is interesting looking at parallel ray trace is the spot of confusion on the retina, since the total LSA is lower for virtual model; also the spot of confusion presents a lower spread for the virtual eye model against Navarro eye model. It must be said that the distance of the image plane (e.g. retina) was fixed as in the original model at 24.00398 mm from the cornea apex.

It must be said that this plane should not necessary be the best plane in which the spot of confusion is the lowest. In the literature retina radius has an accepted value of – 12 mm and the distance from apex and the aspheric coefficient are adjusted along to obtain vertex power, on-axis and off-axis aberrations similar to real eyes.

This is clear looking at the spot of confusion of the virtual eye with the substitution of the anterior cornea surface with data coming from topography. As it can be seen these data presents some imbalances due to a misalignment between the optical axis and the vertex of the real cornea, but since aberrations data are not available it could not be said if these misalignment arise from experimental errors or from a decentration of the real eye axis.

Looking at sagittal and tangential power errors of the virtual eye and of the Navarro et al. eye model it can be seen that the first one introduce lower astigmatism errors and has an highest mean power error then the second one. Astigmatism is close to physiological data.

In both cases the mean power error presents a trend that does not fit physiological data, in particular the real trend present an opposite sign. From the literature data it has been seen that the difference between eye models (Lotmar, 1971; Kooijman, 1983; Navarro et al., 1985; Liou and Brennan, 1997; Atchison, 2006) and real eye data may arise from two main factors.

GRIN lens have the effect to lower the mean power error without lowering the astigmatism so much. Liou and Brennan, and Atchison models that have a GRIN lens models in fact a closer to real data (Bakaraju et al., 2008), then the other models.

As stated in Bakaraju et al. article, probably the main effect that changes the mean power error is the aspheric coefficient of the retina. Atchison model is the only one that in Bakaraju et al. tests implements an aspherical retina and in fact is the only one that is able to lower more then other models the mean power error.

It must be taken into account that the introduction of aspheric coefficient may benefit to the mean power error but could change the astigmatism of the eye, and both data, astigmatism and power, should be considered to let the eye models to be close to real eyes.

Chapter 6. Conclusions

A geometrical model of a human eye is a fundamental instrument for the analysis and evaluation of refraction errors and aberrations, and it may be used for the design of ophthalmic lenses specifically customised for the specific ametropy. Moreover a 3D eye model can be used for didactical purpose.

In this context for the best of our knowledge no commercial CAD is able to modelised and analyse the optical behaviour of a human eye with real geometrical characteristics detected from specific optical tools, e.g. topographer, OCT,MRI, aberrometer.

In this work it has been develop a 3D virtual environment that allow freeform shape modeling and oprical analysis of an individual virtual eye.

Adopting the output data of measurement instruements involved in ocular ametropy analysis, shape modeling techniques have been developed.

After the design of the virtual eye, tools for optical analysis, based on ray tracing, and geometrical analysis, based on curvature evaluation, have been implemented.

Topography data are used as input for the construction of NURBS surface of the anterior cornea. Shadow photogrammetry imaging data are used to develop a lens model based on geometrical and optical constraints. This new model is able to embed age-dependent and accommodation-dependent data for its modelisation.

Proposed model is tested against five literature models. The proposed model is close to the figuring conicoid model both in shape and in curvature and so in opical behaviour. In particular the presented model shows a continuous curvature all over the countour, this feature is important for the modelisation of a lens coherent with physiological data. Moreover a continuous curvature is important also for FEM analysis due to not introduce any unwanted stress in the junction zones.

This model is also analysed against real data from shadow photogrammetry provided by Urs data (Urs et al., 2009). Deviation from the real data has shown a good behaviour of the proposed lens model. In particular the lens model performances are closer to mid-age lens.

Trends of curvature for different ages seem to show a posterior stability about the asphericity coefficient, instead anterior curvature and asphericity tends to vary along the age.

The anterior cornea data and the porposed model are used to develop a virtual eye into a 3D CAD environment. Specific tools for curvature and optical analysis have been developed for the specific CAD Rhinoceros.

Virtual eye performances against Navarro eye model are analysed. In particular longitudinal spherical aberration, spot of confusion on the retina surface, and sagittal and tangential power errors have been tested.

Optical measurement shows that the substitution of the original two aspheric lens model of the Navarro eye with the proposed model increase the performances of the eye. In particular results more close to physiological data about the longitudinal spherical aberration, spot of confusion and astigmatism are founded. Higher mean power errors are founded.

In this work data acquired by different techniques have been integrated in a unique 3D modelisation environtment, allowing optical and and geometrical evaluations. These tools are a fundamental basis point for a better cohoprension of human vision mechanism, in particular accommodation, and for the design of costumised ophthalmic lenses.

It must be said that the proposed model lens is construct with a homogeneus index of refraction. Future works will introduce gradient index models into the lens model, and we think that this will improved the performances of the virtual eye model.

Other future works will improve the tools already created for the CAD environment for optical analysis. In particular off-axis optical analysis will be improved with the introduction of multiple ray-tracing. About the improvement of spot of confusion analysis, a tool for the best image plane founding will be implemented.

Local curvature analysis will be ported from MATLAB to the CAD so that complex surfaces, e.g. progressive lens, can be introduced into the 3D environment.

Future works will include the use of more sophisticated 3D imaging techniques, e.g. 3D MRI, or aberrometry, for a more realistic evaluation of the different surfaces of the eye. In particular ray-tracing will be used for the definition of aberrometry and wave-tracing tools.

The future achievement will be introduce ophthalmic lens design and analysis into CAD and test this kind of lenses with the tools alredy created, and see the performances of designed lenses on the virtual eye.

Appendix A. Surface curvature

A surface can be expressed in parametric form as:

$$S = \begin{bmatrix} x(u) \\ y(v) \\ z(u,v) \end{bmatrix}$$

The first derivative along the parameterization u and v are then:

$$S_u = \begin{bmatrix} x_u \\ 0 \\ z_u \end{bmatrix} \qquad S_v = \begin{bmatrix} 0 \\ y_v \\ z_v \end{bmatrix}$$

and from their product the normal to the surface can be found as:

$$\perp = \frac{S_\rho \times S_\theta}{\left|S_\rho \times S_\theta\right|} = \frac{1}{\sqrt{x_u{}^2 y_v{}^2 + x_u{}^2 z_v{}^2 + y_v{}^2 z_u{}^2}} \cdot \begin{bmatrix} -y_v z_u \\ -x_u z_v \\ x_u y_v \end{bmatrix}.$$

The second partial derivative of the surface S along u and v and cross derivative is then:

$$S_{uu} = \begin{bmatrix} x_{uu} \\ 0 \\ z_{uu} \end{bmatrix} \qquad S_{vv} = \begin{bmatrix} 0 \\ y_{vv} \\ z_{vv} \end{bmatrix} \qquad S_{uv} = S_{vu} = \begin{bmatrix} 0 \\ 0 \\ z_{uv} \end{bmatrix}$$

From the following expression which it the cross product of the first and second fundamental form (see chapter 1) can be found the following expression for the curvature:

$$(EG - F^2) \cdot k^2 - (EN + GL - 2FM) \cdot k + (LN - M^2) = 0$$

which coefficents are expressed by:

$$E = S_u \cdot S_u = x_u{}^2 + z_u{}^2 \qquad G = S_v \cdot S_v = y_v{}^2 + z_v{}^2 \qquad F = S_u \cdot S_v = z_u \cdot z_v$$

$$L = S_{vv} \cdot \perp = \frac{x_u y_v z_{uu} - y_v z_u x_{uu}}{\sqrt{x_u{}^2 y_v{}^2 + x_u{}^2 z_v{}^2 + y_v{}^2 z_u{}^2}}$$

$$N = S_{vv} \cdot \perp = \frac{x_u y_v z_{vv} - x_u z_v y_{vv}}{\sqrt{x_u{}^2 y_v{}^2 + x_u{}^2 z_v{}^2 + y_v{}^2 z_u{}^2}}$$

$$M = S_{uv} \cdot \perp = \frac{x_u y_v z_{uv}}{\sqrt{x_u{}^2 y_v{}^2 + x_u{}^2 z_v{}^2 + y_v{}^2 z_u{}^2}}.$$

Solving the equality will lead to the maximum and minimum curvature.

Appendix B. Revolution surface curvature

A surface of revolution can be expressed in parametric form as S=(u, v, f(u,v)), in particular in cylindrical coordinate it can be written:

$$S = \begin{bmatrix} \rho \cdot \cos\theta \\ \rho \cdot \sin\theta \\ f(\rho,\theta) \end{bmatrix}$$

The first derivative of S along ρ and θ and the normal vector to the surface can be expressed as:

$$S_\rho = \begin{bmatrix} \cos\theta \\ \sin\theta \\ f_\rho \end{bmatrix} \qquad S_\theta = \begin{bmatrix} -\rho \cdot \sin\theta \\ \rho \cdot \cos\theta \\ f_\theta \end{bmatrix} \qquad \perp = \frac{S_\rho \times S_\theta}{\left|S_\rho \times S_\theta\right|} = \frac{1}{\sqrt{\rho^2 f_\rho^2 + f_\theta^2 + \rho^2}} \cdot \begin{bmatrix} f_\theta \sin\theta - \rho f_\rho \cos\theta \\ -f_\theta \cos\theta - \rho f_\rho \sin\theta \\ \rho \end{bmatrix}$$

and the second derivative along ρ, θ and the cross derivative as:

$$S_{\rho\rho} = \begin{bmatrix} 0 \\ 0 \\ f_{\rho\rho} \end{bmatrix} \qquad S_{\theta\theta} = \begin{bmatrix} -\rho \cdot \cos\theta \\ -\rho \cdot \sin\theta \\ f_{\theta\theta} \end{bmatrix} \qquad S_{\rho\theta} = S_{\theta\rho} = \begin{bmatrix} -\sin\theta \\ -\cos\theta \\ f_{\rho\theta} \end{bmatrix}$$

From the following equality:

$$(EG - F^2) \cdot k^2 - (EN + GL - 2FM) \cdot k + (LN - M^2) = 0 \qquad \text{(A.1)}$$

it can be found the coefficents from which the principal curvatures k_1 e k_2 can be found (Mortenson, 2006):

$$E = S_\rho \cdot S_\rho = 1 + f_\rho^2 \qquad G = S_\theta \cdot S_\theta = \rho^2 + f_\theta^2 \qquad F = S_\rho \cdot S_\theta = f_\rho \cdot f_\theta$$

$$L = S_{\rho\rho} \cdot \perp = \frac{\rho \cdot f_{\rho\rho}}{\sqrt{\rho^2 f_\rho^2 + f_\theta^2 + \rho^2}} \qquad N = S_{\theta\theta} \cdot \perp = \frac{\rho^2 \cdot f_\rho + \rho \cdot f_{\theta\theta}}{\sqrt{\rho^2 f_\rho^2 + f_\theta^2 + \rho^2}} \qquad M = S_{\rho\theta} \cdot \perp = \frac{-f_\theta + \rho \cdot f_{\rho\theta}}{\sqrt{\rho^2 f_\rho^2 + f_\theta^2 + \rho^2}}.$$

If we consider a sphero-symmetric geometry, the ray will not change along the angular direction θ so that $f_\theta = f_{\theta\theta} = f_{\rho\theta} = 0$. The coefficients already found will be change as:

$$E = 1 + f_\rho^2 \qquad G = \rho^2 \qquad F = 0$$

$$L = \frac{f_{\rho\rho}}{\sqrt{f_\rho^2 + 1}} \qquad N = \frac{\rho \cdot f_\rho}{\sqrt{f_\rho^2 + 1}} \qquad M = 0.$$

Solving the equalities the maximum and minimum curvature can be found. Moreover the curvature difference A = $k_1 - k_2$ and the mean curvature H = $(k_1 + k_2)/2$ may be defined and in this specific case it will lead to the following expressions:

$$A = \frac{EN - GL}{EG} = \frac{f_\rho^3 + f_\rho - \rho f_{\rho\rho}}{\rho\left(f_\rho^2 + 1\right)^{3/2}} \qquad H = \frac{EN + GL}{2 \cdot EG} = \frac{f_\rho^3 + f_\rho + \rho f_{\rho\rho}}{2\rho\left(f_\rho^2 + 1\right)^{3/2}}$$

in which can be recognised the principal curvatures k_1 and k_2 :

$$k_1 = \frac{f_\rho}{\rho\left(f_\rho^2+1\right)^{1/2}} \qquad k_2 = \frac{f_{\rho\rho}}{\left(f_\rho^2+1\right)^{3/2}}.$$

In a revolution surface we know that the inverse of curvature k_1 is also known as sagittal radius, and the inverse of curvature k_2 is known as tangential radius, so we can write:

$$r_s = \frac{\rho\left(f_\rho^2+1\right)^{1/2}}{f_\rho} \qquad r_t = \frac{\left(f_\rho^2+1\right)^{3/2}}{f_{\rho\rho}}.$$

To verufy the previous formulas we will report the curvature for a spherical surface parameterised as:

$$S = \begin{bmatrix} \rho\cdot\cos\theta \\ \rho\cdot\sin\theta \\ r-\sqrt{r^2-\rho^2} \end{bmatrix}$$

as it can be seen $f(\rho,\theta)=f(\rho)$ and so the revolution surface curvature formuals may be used. The first and the second derivative of the function are:

$$f_\rho = \frac{\rho}{\left(r^2-\rho^2\right)^{1/2}} \qquad f_{\rho\rho} = \frac{r^2}{\left(r^2-\rho^2\right)^{3/2}}$$

from which we can find the princial curvautures k1 and k2, the difference of curvature A and the mean curvature H that will result as the well known sphere ones:

$$k_1 = \frac{1}{r} \qquad k_1 = \frac{1}{r} \qquad A = 0 \qquad H = \frac{1}{r}.$$

The above formulas are commonly used in optics but some substitution are needed to make them in their commonly notation. If ρ = y and f(ρ) = f(y) = z so that the meridional section of the surface S stands on the y-z plane where z-axis is usually called optical axis. And then f_ρ become dz/dy we can then write:

$$r_s = \frac{y\left(1+\left(\frac{dz}{dy}\right)^2\right)^{1/2}}{\frac{dz}{dy}} \qquad r_t = \frac{\left(1+\left(\frac{dz}{dy}\right)^2\right)^{3/2}}{\frac{d^2z}{dy^2}}$$

that are the well known formulas used for conics. If instead both z and y are function of a parameter u so that

$$y = y(u) \qquad z = z(u)$$

then the radii of curvature become:

$$r_s = \frac{y\left((z_u)^2+(y_u)^2\right)^{1/2}}{z_u} \qquad r_t = \frac{\left((z_u)^2+(z_u)^2\right)^{3/2}}{z_u y_{uu} - z_{uu} y_u}$$

where z_u and z_{uu} stant for the first and second derivative of z along u; similarly for y.

Appendix C. Methods for measuring the human eye

C.1. Keratometry

Keratometry is a basic method to measure the curvature of the central anterior corneal surface. Devices are called keratometers, or sometimes ophthalmometers. There are two basic types of keratometers: the instrument based on Helmholtz method and the one according to Javal-Schiotz method. Helmholtz built his laboratory device in 1854 and included a doubling device to eliminate eye movements (Helmholtz, Gullstrand et al. 1909); this device uses two adjustable prisms to measure two axes perpendicular to each other (one position device). Javal and Schiotz modified Helmholtz instrument in 1881 and built a device for clinical use (Javal and Schiotz 1881) that uses only one prism (two position device). Since then, the keratometer became the most popular instrument for measuring corneal curvature. Since it is important for the device to stay in focus when measuring, often the Scheiner principle is used to guarantee a focused image. A popular commercial version of the keratometer according to Helmholtz principle was built by Bausch & Lomb, Inc. (USA); a popular version of the Javal-Schiotz is the keratometer of Haag-Streit AG (Switzerland). In 1950 Hans Littmann developed a keratometer based on Helmholtz design that was produced by Carl Zeiss AG (Germany).

C.2. Topography

Videotopography systems are capable of measuring the complete anterior corneal surface and therefore overcome the limitation of keratometers measuring only the central corneal curvature. This method is also known as keratoscopy or videokeratography.

The principle they use is named after the Portuguese ophthalmologist Antonio Placido, who in 1880 studied the shape of the cornea by observing the reflections of a disk containing concentric black and white rings, now called Placido's disk (Duke-Elder and Abrams 1970). In 1896, Gullstrand built the first photokeratoscope by incorporating a Placido disk into his ophthalmometer. He was able to manually determine the corneal curvature by analyzing the photographs of the cornea (Gullstrand 1966).

In the 1970s and 1980s the first photokeratoscopes were developed for clinical use. Early systems used Polaroid cameras and images had to be hand-digitized. But with the propagation of personal computers systems soon became more automated by using cameras attached to computers that automatically analyzed the images.

Since the 1990s computerized videotopography systems from a number of suppliers were commercially available and Placido-videotopography came into widespread clinical use.

C.3. Ultrasound pachimetry

Ultrasound A-Scan echo-impulse technique, US, has been first used to measure the human eye in 1956 (Mundt and Hughes 1956), and has been steadily improved and is a common measuring method today. Sonic waves are sent into the eye; the echo from the structures of interest is recorded and from the time the echo took the geometric length is calculated. This technique is capable of measuring the axial length as well as other intraocular distances, as the anterior chamber depth, ACD, or lens thickness.

Two methods are distinguished. Using the applanation method, AUS, there has to be a direct contact of the transducer to the cornea. In this case, the cornea actually is indented and therefore the eye is slightly shortened (which is operator dependent). This is avoided with the water-immersion technique, IUS. Here the eye does not come into direct contact with the transducer, instead uses a coupling fluid in between preventing compression. IUS is therefore more accurate than AUS, but slightly more complicated in application because the patient has to be in horizontal position and some coupling device is needed (Kiss, Findl et al. 2002a).

C.4. Partial Coherence Interferometry

In 2000 the lOLMaster (Carl Zeiss Meditec AG, Germany) was introduced. This device measures three quantities: the anterior chamber depth, corneal curvature and axial length.

The anterior chamber depth is determined as the distance between the optical sections of the crystalline lens and the cornea produced by lateral slit illumination. The corneal curvature is determined with conventional keratometry.

The axial length is measured with partial coherence inteferometry, PCI. This is a non-contact optical biometry method that is principally used by optical coherence tomography, OCT, too. The velocity of light is too high for direct measurement of echo delay times as done for example with ultrasound. Therefore the effect of interference of coherent light is used instead. A diode laser of 780 nm delivers a beam of light of short coherence length. This beam is split into two beams in a Michelson interferometer. The interference of the reference beam and the beam reflected by the cornea and the retina is detected by a photodetector. The signals are recorded as a function of the position of a mirror. This mirror position determines the axial length as the distance from the cornea to the retinal pigment epithelium (Kiss, Findl et al. 2002a; Kiss, Findl et al. 2002b). The results of the axial length measurement are recalculated with a statistical calibration function to be comparable to ultrasonic immersion measurements.

C.5. Wavefront-Analyzing Instruments

The two most widely used techniques for objectively measuring the wavefront aberrations of human eyes are instruments based on Hartmann-Shack sensor and instruments based on Tscherning aberroscopy.

The Hartmann-Shack sensor that is widely used in the field of astronomy and adaptive optics has been initially used to measure aberrations of the human eye by Liang et al. (Liang, Grimm et al. 1994). A point source is generated on the retina. The light that emerges from this point source travels through the optical components and leaves through the pupil. In some distance a Hartmann-Shack sensor is positioned that consists of an array of small lenses. Each lenslet focuses its part of the wavefront to a spot in its focal plane. From the position of each spot the

corresponding local slope of the wavefront can be calculated. Recorded with a charge-coupled device, CCD, matrix the whole wavefront can be calculated.

In 1894 Tscherning studied the monochromatic aberrations of the human eye (Tscherning 1894). In 2000 an instrument for automatic wavefront analyzing based on Tscherning's aberroscope was introduced (Mrochen, Kaemmerer et al. 2000a). The device uses a collimated laser beam that illuminates a mask with regular matrix pin holes. This mask produces thin parallel rays that are sent through the eye and strikes the retina. The resulting retinal spot pattern is distorted according to the optical errors of the eye. With a CCD camera this spot pattern is recorded and the deviations of the spots from their ideal positions are evaluated to calculate the optical aberrations. A compact review about wavefront-analyzing instruments is given by Applegate et al. (Applegate, Thibos et al. 2001).

C.6. Purkinje imaging

Purkinje imaging has been one of the most popular methods to perform phakometry. Purkinje images, first described by Purkinje in 1832, are reflections from the ocular surfaces. The radii of curvature of the different ocular components (acting as mirrors) are estimated from the relative height of images of the light source. The brightest reflection (first Purkinje image, PI) comes from the anterior corneal surface and can be used to estimate the corneal radius of curvature, as it is done in keratometry. The third (PIII) and fourth Purkinje images (PIV), from the anterior and posterior surface of the crystalline lens, are used for phakometry. Two algorithms have been proposed to estimate the radii of curvature from the relative heights of PIII and PIV: the equivalent mirror (EM) theorem method, based on the replacement of the different ocular surfaces by a single mirror (Smith and Garner, 1996), and the merit function (MF), based on a recursive method (Barry et al., 2001; Garner, 1997).

C.7. Slit lamp and Scheimpflug photography

This is an imaging technique that provides an assessment of the anterior segment of the eye in a sagittal plane. The principle of the technique is that the film (or CCD) plane, lens plane (used for focusing) and subject plane (plane of focus) are tilted in such a way that all three planes intersect along a straight line. In this condition a subject will be completely in focus. The technique can be used to detect and monitor opacities in the media of the anterior segment (e.g. in the lens), to document these changes and to carry out biometric evaluation (e.g. depth of the anterior chamber, lens thickness measurement).

The Schiempflug photography system was further developed by Hayashi in 1998. It is based on the use of the EAS-1000 anterior eye segment analysis system (Nidet, Gamagori, Japan) equipped with area densitometry to measure the scattering light intensity. This principle is applied to obtain a cross sectional image of the anterior segment. An alignment system is coupled with a television monitor and the slit image of the best quality is transferred to the online image analysis computer. The computer uses area densitometry to measure the scattering light intensity, which is deemed equal to the opacification density. Usually a central 3 mm portion till a peripheral 7 mm zone is investigated. The measurement method is easy to perform and can be done within a few minutes for each eye. Furthermore, the principal mechanism depends on back scattered and not forward scattered light. The system may be limited for research purposes in terms of flexibility.

Dubbelman, van der Heijde and their group have done an extensive use of Scheimpflug

photography (Dubbelman and van der Heijde 2001; Dubbelman, 2001; Dubbleman, 2002). They point out difficulties of the technique such as the necessary use of ray-trace correction of the images, and use it extensively to analyse all ocular surfaces. Their results are both age-dependent and accommodation-dependent and for that they are used as experimental data for the set up of the last schematic eyes (Norrby, 2005; Atchison 2006).

C.8. Magnetic Resonance Imaging

Magnetic resonance imaging (MRI), or nuclear magnetic resonance imaging (NMRI), is primarily a noninvasive medical imaging technique used in radiology to visualize detailed internal structure and limited function of the body. MRI provides much greater contrast between the different soft tissues of the body than computed tomography (CT) does, making it especially useful in neurological (brain), musculoskeletal, cardiovascular, and oncological (cancer) imaging.

Unlike CT, MRI uses no ionizing radiation. Rather, it uses a powerful magnetic field to align the nuclear magnetization of (usually) hydrogen atoms in water in the body. Radio frequency (RF) fields are used to systematically alter the alignment of this magnetization. This causes the hydrogen nuclei to produce a rotating magnetic field detectable by the scanner. This signal can be manipulated by additional magnetic fields to build up enough information to construct an image of the body.

Magnetic resonance imaging is a relatively new technology. The first MR image was published in 1973 and the first cross-sectional image of a living mouse was published in January 1974. The first studies performed on humans were published in 1977. By comparison, the first human X-ray image was taken in 1895.

Magnetic resonance imaging is a development of nuclear magnetic resonance. Originally, the technique was referred to as nuclear magnetic resonance imaging (NMRI). However, because the word nuclear was associated in the public mind with ionizing radiation exposure, it is generally now referred to simply as MRI. Scientists still use the term NMRI when discussing non-medical devices operating on the same principles. The term magnetic resonance tomography (MRT) is also sometimes used.

C.9. Shadow-photogrammetry

The shadow-photogrammetric system consists of a modified optical comparator (BP-305, Topcon, Tokyo. Japan) with two light sources to enable photography of the crystalline lens in the coronal and sagittal planes. The immersion cell described in Rosen et al. (2006) was modified by replacing the lens-holding ring with a supporting mesh made of 10-0 nylon sutures. This enabled the entire posterior surface of the lens to be available for contour detection. A 4Mp Nikon Coolpix 4500 digital camera (Tokyo, Japan) positioned at a fixed distance from the screen was used to capture the coronal and sagittal views of the lens. A ruler (l376T-25, Keuffel and Esser Co,, Hoboken, New jersey) was also photographed on each image for scaling purposes.

The images were pre-processed with Canvas 9.0 (ACD Systems of America, Miami, FL). They were scaled against the ruler included in the image and were adjusted for magnification (20x) of the comparator.

Appendix D. Quadratic fitting and evaluation of optical properties

This is the MATLAB code for the quadrating fitting method and the evaluation of optical properties:

MAIN:

```
clear all
close all
clc
warning('off');

Nome_input=input('Nome del file da elaborare = ','s');
Nome_output=input('Nome del file di output = ','s');
fid=fopen([Nome_input '.txt'],'r');
S = fscanf(fid,'%e %e %e',[3 inf])';
fclose(fid);
RI=input('Raggio intorno = ');

tic
%punto di partenza
Lista=S;
[n,p]=size(S);
U=S(1,1);
W=S(1,2);
Z=S(1,3);
N=[0 0 0];
R1=intorno(U,W,Z,S,RI);
[R,O,norm]=rotazione(U,W,Z,R1,N);
[k1,k2,lbd1,lbd2]=curvatura(R,O);
for h=1:n
   if S(h,1)==U && S(h,2)==W && S(h,3)==Z
      S(h,4)=norm(1);
      S(h,5)=norm(2);
      S(h,6)=norm(3);
      S(h,7)=k1;
      S(h,8)=k2;
      S(h,9)=lbd1;
      S(h,10)=lbd2;
   end
end
[PV,Lista]=primivicini([U W Z],Lista,RI);

%punti successivi
while length(PV)~=0
   [npv,ppv]=size(PV);
   for h=1:npv
```

```
      N=[];
      U=PV(h,1);
      W=PV(h,2);
      Z=PV(h,3);
      R1=intorno(U,W,Z,S,RI);
      N(:,1)=R1(:,4);
      N(:,2)=R1(:,5);
      N(:,3)=R1(:,6);
      [R,O,norm]=rotazione(U,W,Z,R1,N);
      [k1,k2,lbd1,lbd2]=curvatura(R,O);
      for j=1:n
         if S(j,1)==U && S(j,2)==W && S(j,3)==Z
            S(j,4)=norm(1);
            S(j,5)=norm(2);
            S(j,6)=norm(3);
            S(j,7)=k1;
            S(j,8)=k2;
            S(j,9)=lbd1;
            S(j,10)=lbd2;
         end
      end
   end
   [PV,Lista]=primivicini(PV,Lista,RI);
end

%punti rimasti
[nl,pl]=size(Lista);
for h=1:nl
   N=[];
   U=Lista(h,1);
   W=Lista(h,2);
   Z=Lista(h,3);
   R1=intorno(U,W,Z,S,RI);
   N(:,1)=R1(:,4);
   N(:,2)=R1(:,5);
   N(:,3)=R1(:,6);
   [R,O,norm]=rotazione(U,W,Z,R1,N);
   [k1,k2,lbd1,lbd2]=curvatura(R,O);
   for j=1:n
      if S(j,1)==U && S(j,2)==W && S(j,3)==Z
         S(j,4)=norm(1);
         S(j,5)=norm(2);
         S(j,6)=norm(3);
         S(j,7)=k1;
         S(j,8)=k2;
         S(j,9)=lbd1;
         S(j,10)=lbd2;
      end
   end
end

X=S(:,1);
Y=S(:,2);
Z=S(:,3);
N1=S(:,4);
N2=S(:,5);
N3=S(:,6);
```

```
K1=S(:,7);
K2=S(:,8);
LBD1=S(:;9);
LBD2=S(:;10);
G=K1.*K2;
Ro=sqrt(X.^2+Y.^2);
RR=260-2*Ro;
H=1000*(1.5-1)*(abs(K1)+abs(K2))./2;
A=1000*(1.5-1)*abs(K1-K2);
B=[X Y Z K1 LBD1 K2 LBD2 H A];
B=sortrows(B,4);
toc

fod=fopen([Nome_output '.txt'],'w');
for h=1:n
   fprintf(fod,'%6.4f\t %6.4f\t %6.4f\t %6.12f\t %6.12f\t %6.12f\t %6.12f\t \n',B(h,:));
end
fclose(fod);
```

INTORNO:

```
function [S1] = intorno(U,W,Z,S,RI)
indice=[];
S1=[];

%calcolo della distanza
Distanza=(S(:,1)-U).^2+(S(:,2)-W).^2+(S(:,3)-Z).^2;

%scan della matrice e output
indice=find(Distanza<(RI^2));
if length(indice)<7
   S1=[];
else
S1=S(indice,:);
end
```

ROTAZIONE:

```
function [R,O,norm] = rotazione(U,W,Z,R1,N)
R1=R1(:,1:3);
[n,p]=size(R1);
[nn,pp]=size(N);
R=[];
O=[];
Rnorm=[];
for k=1:n;
   B(k)=1;
end

%inizializzazione del vettore primi vicini, punti di origine, intorno
%normale
R1=[R1 B'];
O1=[U W Z 1];
Rnorm=normale(U,W,Z,R1,2);
%Rnorm=intorno(U,W,Z,R1,1);

%calcolo del piano
R_dist(1,1)=sum((Rnorm(:,1)-U).^2);
R_dist(1,2)=sum((Rnorm(:,1)-U).*(Rnorm(:,2)-W));
```

```
R_dist(1,3)=sum((Rnorm(:,1)-U).*(Rnorm(:,3)-Z));
R_dist(2,1)=R_dist(1,2);
R_dist(2,2)=sum((Rnorm(:,2)-W).^2);
R_dist(2,3)=sum((Rnorm(:,2)-W).*(Rnorm(:,3)-Z));
R_dist(3,1)=R_dist(1,3);
R_dist(3,2)=R_dist(2,3);
R_dist(3,3)=sum((Rnorm(:,3)-Z).^2);

%autovettori del piano (v1, v2, n, traslazione)
[EV,ev]=eig(R_dist);
ev1(1)=ev(1,1);
ev1(2)=ev(2,2);
ev1(3)=ev(3,3);
[C1,I]=max(ev1);
[E1,K]=min(ev1);
EV1(:,1)=[EV(:,I);0];
EV1(:,2)=[EV(:,6-I-K);0];
EV1(:,3)=[EV(:,K);0];
EV1(:,4)=[U W Z 1]';

% confronto delle normali
norm=EV1(1:3,3)';
s=0;
for i=1:nn
   s=s+sign(dot(norm,N(i,:)));
end
if s<0
   EV1(:,3)=-EV1(:,3);
   norm=EV1(1:3,3)';
end

%rototraslazione
R=(inv(EV1)*R1')';
O=inv(EV1)*O1';
```

NORMALE:

```
function [S1] = normale(U,W,Z,S,RN)
S1=[];
S=S(:,1:3);

Distanza=(S(:,1)-U).^2+(S(:,2)-W).^2+(S(:,3)-Z).^2;
B=[S Distanza];
B=sortrows(B,4);
i=0;
j=1;

while i<=RN
   if round(1000*B(j+1,4))==round(1000*B(j,4))
      i=i;
      j=j+1;
   else
      i=i+1;
      j=j+1;
   end
end

S1=B(1:j-1,1:3);
```

CURVATURA:

```
function [k1,k2,lbd1,lbd2] = curvatura(R,O)

%matrice M di minimizzazione dei quadrati
M(1,1)=sum(R(:,1).^4);
M(1,2)=sum((R(:,1).^2).*(R(:,2).^2));
M(1,3)=sum((R(:,1).^3).*R(:,2));
M(1,4)=sum(R(:,1).^3);
M(1,5)=sum((R(:,1).^2).*R(:,2));
M(1,6)=sum(R(:,1).^2);
M(2,1)=M(1,2);
M(2,2)=sum(R(:,2).^4);
M(2,3)=sum((R(:,2).^3).*R(:,1));
M(2,4)=sum((R(:,2).^2).*R(:,1));
M(2,5)=sum(R(:,2).^3);
M(2,6)=sum(R(:,2).^2);
M(3,1)=M(1,3);
M(3,2)=M(2,3);
M(3,3)=sum((R(:,1).^2).*(R(:,2).^2));
M(3,4)=sum((R(:,1).^2).*R(:,2));
M(3,5)=sum((R(:,2).^2).*R(:,1));
M(3,6)=sum(R(:,1).*R(:,2));
M(4,1)=M(1,4);
M(4,2)=M(2,4);
M(4,3)=M(3,4);
M(4,4)=sum(R(:,1).^2);
M(4,5)=sum(R(:,1).*R(:,2));
M(4,6)=sum(R(:,1));
M(5,1)=M(1,5);
M(5,2)=M(2,5);
M(5,3)=M(3,5);
M(5,4)=M(4,5);
M(5,5)=sum(R(:,2).^2);
M(5,6)=sum(R(:,2));
M(6,1)=M(1,6);
M(6,2)=M(2,6);
M(6,3)=M(3,6);
M(6,4)=M(4,6);
M(6,5)=M(5,6);
M(6,6)=length(R);

%vettore del termine noto
V(1)=sum((R(:,1).^2).*R(:,3));
V(2)=sum((R(:,2).^2).*R(:,3));
V(3)=sum(R(:,1).*R(:,2).*R(:,3));
V(4)=sum(R(:,1).*R(:,3));
V(5)=sum(R(:,2).*R(:,3));
V(6)=sum(R(:,3));

%vettore dei coefficenti
coef=inv(M)*V';
a=coef(1);
b=coef(2);
c=coef(3);
d=coef(4);
e=coef(5);
```

```
f=coef(6);

%calcolo delle I e II forma canonica
dP_dU=[1 0 2*a*O(1)+c*O(2)+d];
dP_dW=[0 1 2*b*O(2)+c*O(1)+e];
d2P_dW2=[0 0 2*b];
d2P_dU2=[0 0 2*a];
d2P_dUdW=[0 0 c];
normale=cross(dP_dU,dP_dW);
nn=normale/norm(normale);
E=dot(dP_dU,dP_dU);
F=dot(dP_dU,dP_dW);
G=dot(dP_dW,dP_dW);
L=dot(d2P_dU2,nn);
M=dot(d2P_dUdW,nn);
N=dot(d2P_dW2,nn);

%curavtura massima e minima
k1=((E*N+G*L-2*F*M)+sqrt((E*N+G*L-2*F*M)^2-4*(E*G-F^2)*(L*N-M^2)))/(2*(E*G-F^2));
k2=((E*N+G*L-2*F*M)-sqrt((E*N+G*L-2*F*M)^2-4*(E*G-F^2)*(L*N-M^2)))/(2*(E*G-F^2));

%direzione principale 1
lbd1=((G*L-E*N)+sqrt((G*L-E*N)^2-4*(F*N-G*M)*(E*M-F*L)))/(2*(F*N-G*M));
d_x1=lbd1/(sqrt((lbd1)^2+1));
d_y1=1/(sqrt((lbd1)^2+1));

%direzione principale 2
lbd2=((G*L-E*N)-sqrt((G*L-E*N)^2-4*(F*N-G*M)*(E*M-F*L)))/(2*(F*N-G*M));
d_x2=lbd2/(sqrt((lbd2)^2+1));
d_y2=1/(sqrt((lbd2)^2+1));
```

PRIMIVICINI:

```
function [S2,S] = primivicini(S1,S,RI)
indice=[];
S2=[];
[n,p]=size(S);
[n1,p1]=size(S1);

%cancellazione dalla Lista degli ex-primi vicini
for i=1:n1
   for j=1:n
      if S(j,1)==S1(i,1) && S(j,2)==S1(i,2) && S(j,3)==S1(i,3)
         S(j,1)=NaN;
         S(j,2)=NaN;
         S(j,3)=NaN;
      end
   end
end

%calcolo dei primi vicini e cancellazione dalla Lista
for i=1:n1
   PV=intorno(S1(i,1),S1(i,2),S1(i,3),S,RI);
   S2=[S2; PV];
   [npv,ppv]=size(PV);
   for k=1:npv
      for j=1:n
```

```
        if S(j,1)==PV(k,1) && S(j,2)==PV(k,2) && S(j,3)==PV(k,3)
           S(j,1)=NaN;
           S(j,2)=NaN;
           S(j,3)=NaN;
        end
      end
   end
end


%ordinamento dei primi vicini e della Lista lungo x
S2=sortrows(S2);
S=sortrows(S);
n=sum(~isnan(S(:,1)));
S=S(1:n,:);
```

Appendix E. Ray tracing

This is the Rhinoceros script for the ray tracing from a surface:

```
Option Explicit

Call math_ray()

Sub math_ray()
  Dim M, i, j
  Dim st : st = 0.5
  Dim Num : Num = 4/st
  ReDim arrLine(Num)
  Dim arrSurf, strSurf
  Dim updates

''Superfici di Refrazione''''''''''''''''''''''''''''''''''''''''''''''''''''''''''''''''

  arrSurf = Rhino.GetObjects("Pick some curves", 4)
  If IsArray(arrSurf) Then
    M = 0
    For Each strSurf In arrSurf
      M = M + 1
      'Rhino.Print "Object identifier: " & strSurf
    Next
    ReDim n(M), items(M), values(M)
    For i = 0 To M
      items(i) = "n" & i
      values(i) = CStr(1)
    Next
  End If

''InputBox''''''''''''''''''''''''''''''''''''''''''''''''''''''''''''''''''''''''''''''''

  updates = Rhino.PropertyListBox(items, values, "Specify refraction index", "Ray")
  For i = 0 To M
    n(i) = CDbl(updates(i))
  Next

''Calcolo Refrazione''''''''''''''''''''''''''''''''''''''''''''''''''''''''''''''''''''''
  Dim Pt0, Pt1, Pt2, PtX, PtY
  Dim arrNormal, arrTangent, Rt
  Dim vctIncident, vctNormal, vctRefract
  Dim alfa, beta
  Dim Line, Line0, CCI

  'Inizializzazione
  Pt0 = Array(0,0,0)
```

```
  PtX = Array(100,0,0)
  PtY = Array(-100,0,0)
  Line0 = Rhino.AddLine(Ptx, PtY)

  For i = 0  To 2*Num
    'Linea dall'infinito parallela
    Pt1 = Array(-100,0,(i-Num)*St)
    Pt2 = Array(100,0,(i-Num)*St)
    Line  = Rhino.AddLine(Pt1, Pt2)
    'arrLine(i) = Line

    For j = 0 To M-1

    For j = 0 To M-1
      'Intersezione superfici di rifrazione
      CCI = Rhino.CurveCurveIntersection(arrSurf(j), Line)
      Rhino.DeleteObject(Line)
      Line = Rhino.AddLine(Pt1, CCI(0,1))

      'Normale
      arrTangent = Rhino.CurveTangent(arrSurf(j), CCI(0,5))
      arrNormal  = Rhino.CurveCurvature(arrSurf(j),CCI(0,5))(4)

      'Vettore incidente e normale
      vctIncident = Rhino.VectorUnitize(Rhino.VectorCreate(CCI(0,1),Pt1))
      vctNormal   = Rhino.VectorUnitize(Rhino.VectorCreate(arrNormal,Pt0))

      'Refrazione
      alfa = Rhino.VectorDotProduct (vctNormal,Rhino.VectorScale(vctIncident,-1))
      beta = Sqr(1-(n(j)/n(j+1))^2*(1-alfa^2))
      vctRefract = Rhino.VectorAdd(Rhino.VectorScale(vctIncident,n(j)/n(j+1)),
                                                          Rhino.VectorScale(vctNormal,(n(j)/n(j+1))*alfa-Sgn(alfa)*beta))

     'Raggio rifratto
      Line = Rhino.MoveObject(Rhino.ExtendCurveLength(Rhino.AddLine(Pt0,vctRefract), 0, 1, 500),Pt0,CCI(0,1))

      'Dati nuova superficie
      Pt1  = CCI(0,1)

    Next

  Next

  Rhino.DeleteObject(Line0)

End Sub
```

Reference

Abolmaali, A., Schachar, R.A., Le, T., 2007. Sensitivity study of human crystalline lens. Comput. Meth. Progr. Bio. 85 (1), 77–90.

Alonso, J., Alda, J., 2003. Ophthalmic Optics. Encyclopedia of Optical Engineering, Marcel Dekker, Inc

Angel, E., 1990. Computer graphics. Addison-Wesley Publishing Company.

Atchison, D.A., 1992. Spectacle lens design: a review. Optical Society of America 31 (19), 3579-3585.

Atchison, D.A., 2006. Optical Models for Human Myopic Eyes. Vision Research 46, 2236-2250.

Atchison, D.A., Smith, G., 2000. Optics of the Human Eye. Butterworth-Heinemann, Australia.

Bakaraju, R.C., Ehrmann, K., Papas, E., Ho, A., 2008. Finite schematic eye models and their accuracy to in-vivo data. Vision Research 48, 1681–1694.

Bennett, R.B., Rabbetts, R.B., 1984. Bennett & Rabbetts' Clinical Visual Optics. Butterworth-Heinemann, Australia.

Campbell, C.E., 2010. Nested shell optical model of the lens of the human eye. J. Opt. Soc. Am. A. 27, 2432-2441.

Chen, X., Schmitt, F., 1992. Intrinsic Surface Properties from Surface Triangulation. The Second European Conference on Computer Vision, 739-743.

Chien, M.C., Tseng, H., Schachar, R.A., 2003. A mathematical expression for the human crystalline lens. Compr. Ther. 29 (4), 245–258.

Concheri, G., Savio, G., Meneghello, R., 2006. Curvature estimation for optical analysis. Proceedings of the 6th Euspen International Conference, 87-90.

De Antonia, L., 2004. Caratterizzazione micro- e macro-geometrica nel processo produttivo di stampi per lenti oftalmiche. DAUR - Laboratorio di Disegno e Metodi dell'Ingegneria Industriale - Università degli Studi di Padova, A.A. 2003-2004.

de Castro, A., Ortiz, S., Gambra, E., Siedlecki, D., Marcos, S., 2010. Three-dimensional reconstruction of the crystalline lens gradient index distribution from OCT imaging. Opt. Express.

18, 21905-21917.

Dennis, J.E., 1977. Nonlinear Least-Squares. State of the Art in Numerical Analysis, ed. D. Jacobs, Academic Press, 269–312.

Desbrun, M., Meyer, M., Alliez, P., 2002. Intrinsic parameterizations of Surface Meshes. Computer Graphics Forum 21 (3), 209-218.

Díaz, J.A., Pizarro, C., Arasa, J., 2008. Single dispersive gradient-index profile for the aging human lens. J. Opt. Soc. Am. A. 25, 250-261.

Do Carmo, M., 1976. Differential Geometry of Curves and Surfaces. Prentice-Hall, NJ. Douros, I., Buxton, B., 2002. Three-Dimensional Surface Curvature Estimation Using Quadric Surfaces Patches. Scanning 2002 Proceeding.

Drasdo, N., Fowler, G.W., 1974. Non-linear Projection of the Retinal Image in a Wide-angle Schematic Eye. British Journal of Ophtalmology 58, 709-714.

Dubbelman, M., Van der Heijde, G.L., 2001. The shape of the aging human lens: curvature, equivalent refractive index and the lens paradox. Vision Research 41, 1867-1877.

Dubbelman, M., Van der Heijde, G.L., Weeber, H.A., 2001. The thickness of the aging human lens obtained from corrected Scheimpflug images. Optometry and Vision Science 78, 411-416.

Dubbelman, M., van der Heijde, G.L., Weeber, H.A., 2005. Change in shape of the aging human crystalline lens with accommodation. Vision Res. 45 (1), 117–132.

Dubbelman, M., Weeber, H.A., Van der Heijde, G.L., Volker–Dieben, H.J., 2002. Radius and asphericity of the posterior corneal surface determined by corrected Scheimpflug photography. Acta Ophthalmologica 70, 255–261.

Dunne, M.C.M., Royston, J.M., Barnes, D.A., 1992. Normal variation of the posterior corneal surface. Acta Ophthalmologica 70, 255-261.

Dyn, N., Hormann, K., Kim, S. J., Levin, D., 2001. Optimizing 3D Triangulations Using Discrete Curvature Analysis. Mathematical Methods for Curves and Surfaces, 135-146.

Einighammer, J., 2009. The Indiviual Virtual Eye. University of Tubingen.

Escudero-Sanz, I., Navarro, R., 1999. Off-axis Aberrations of a Wide-angle Schematic Eye Model. Journal of the Optical Society of America A. 16, 1881-1891.

Fincham, E.F., 1937. The mechanism of accommodation. Brit. J. Ophthalmol. 8, 5–80.

Floater, M. S., 1997. Parametrization and smooth approximation of surface triangulation. Computer Aided Geometric Design 14, 231-250.

Gatzke, T. D., Grimm, C. M., 2003. Assessing Curvature Metrics on Triangular Meshes. Tecnical

Report, Washington University, St. Louis Missouri.

Gatzke, T.D., Grimm, C. M., 2006. Estimating Curvature on Triangular Meshes. International Journal of Shapes Modeling 12 (1), 1-23.

Glasser, A., Campbell, M.C., 1999. Biometric, optical and physical changes in the isolated human crystalline lens with age in relation with presbyopia. Vision Res. 39 (11), 1991–2015.

Glasser, A., Campbell, M.C., 1999. Biometric, optical and physical changes in the isolated human crystalline lens with age in relation with presbyopia. Vision Research 39 (11), 1991-2015.

Goldfeather, J., Interrante, V., 2004. A Novel Cubic-Order Algorithm for Approximating Principal Direction Vectors. ACM Trans. Graph. 23, 45-63.

Goldman, R., 2005. Curvature formulas for implicit curves and surfaces. Computer Aided Geometric Design 22 (7), 632-658.

Goncharov, A.V., Dainty, C., 2007. Wide-field schematic eye models with gradient-index lens. J. Opt. Soc. Am. A. 24, 2157-2174.

Goncharov, A.V., Dainty, C., 2007. Wide-field schematic eye models with gradient-index lens. Journal of the Optical Society of America A 24 (8), 2157-2174.

Goncharov, A.V., Nowakowski, M., Sheehan, M.T., Dainty, C., 2008. Reconstruction of the optical system of the human eye with reverse ray-tracing. Optics Express 16 (3), 1692-1703.

Guirao, A., Redondo, M., Artal, P., 2000. Optical aberration of the human cornea as a funciont of age. Optical Society of America 17 (10), 1697-1702.

Guo, H.Q., Wang, Z., Zhao, Q., Quan, W., Wang, Y., 2005. Individual Eye Model Based on Wavefront Aberration. Optik 116, 80-85.

Hameiri, E., Shimshoni, I., 2003. Estimating the Principal Curvatures and the Darboux Frame from Real 3D Range Data. IEEE Transactions on Systems, Man and Cybernetics, Part B 33 (4), 626-637.

Hamman B., 1993. Curvature Approximation for Triangulated Surfaces. Computing Supplements 8, 139-153.

Hermans, E., Dubbelman, M., van der Heijde, G.L., Heethaar, R.M., 2008. Change in the accommodative force on the lens of the human eye with age. Vision Res. 48, 119–126.

Hermans, E., Dubbleman, M., van der Heijde, R., Heethaar, R.M., 2007. The shape of the human lens nucleus with accommodation. J. Vision 7 (10), 1–10.

Hermans, E., Pouwels, P.J., Dubbelman, M., Kuijer, J.P.A., van der Heijde, R.G.L., Heethaar, R.M., 2009. Constant volume of the human lens and decrease in surface area of the capsular bag during accommodation: an MRI and Scheimpflug study. Invest. Ophth. Vis. Sci. 50 (1), 281–289.

Hermans, E.A., Dubbleman, M., van der Heijde, G.L., Heethaar, R.M., 2006. Estimating the external force acting on the human eye lens during accommodation by finite element modelling. Vision Res. 46 (21), 3642–3650.

Howcroft, M.J., Parker, J.A., 1977. Aspheric curvature for the human lens. Vision Research 17. 1217-1223.

ISO 10322-1:2006 Ophthalmic optics – Semi-finished spectacle lens blanks – Part 1: Specifications for single-vision and multifocal lens blanks.

ISO 10322-2:2006 Ophthalmic optics – Semi-finished spectacle lens blanks – Part 2: Specifications for progressive power lens blanks.

ISO 13666:1998 Ophthalmic optics – Spectacle lenses – Vocabulary.

ISO 3:1973 Preferred numbers – Series of preferred numbers.

ISO/IEC Guide 98-3:2008 Uncertainty of measurement – Part 3: Guide to the expression of uncertainty in measurement (GUM:1995).

Jalie, M., 1977. The Principles of ophthalmic lenses. The Association of Dispensing Opticians, London.

Jones, C.E., Atchison, D.A., Meder, R., Pope, J.M., 2005. Refractive index distribution and optical properties of the isolated human lens measured using magnetic resonance imaging (MRI). Vision Res. 45 (18), 2352–2366.

Jones, C.E., Atchison, D.A., Pope, J.M., 2007. Changes in lens dimension and refractive index with age and accommodation. Optometry and Vision Science 84 (10) 990-995.

Jones, C.E., Atchison, D.A., Pope, J.M., 2007. Changes in lens dimension and refractive index with age and accommodation. Optometry Vision Sci. 84 (10), 990–995.

Kasprzak, H.T., 2000. New approximation for the whole profile of the human crystalline lens. Ophthal. Physl Opt. 20 (1), 31–43.

Kasprzak, H.T., Iskander, D.R., 2006. Approximating ocular surfaces by generalised conic curves. Ophthal. Physl Opt. 26, 602–609.

Kasthurirangan, S., Markwell, E., Atchison, D.A., Pope, J.M., 2008. In vivo study of changes in refractive index distribution in the human crystalline lens with age and accommodation. Investigative Ophthalmology & Visual Science 49 (6), 2531-2540.

Kim, S. J., Kim, C. H., Levin, D., 2001. Surface Simplification Using Discrete Curvature Norm. The Third Israle-Korea Bineational Conference on Geometric Modeling and Computer Graphics, Seul, Korea.

Krsek, P., Lukács, C., Martin, R.R., 1998. Algorithms for Computing Curvatures from Range Data.

The Mathematics of Surfaces 8, 1-16.

Lam, A.K.C., Douthwaite, W.A., 1999. The ageing effect on the central posterior corneal radius. Ophthalmic and Physiological Optics 20 (1), 63-69.

Le, T., 2005. Non-linear finite element model analysis of human accomodation lens. University of Texas, Arlington.

Levenberg, K., 1944. A Method for the Solution of Certain Problems in Least-Squares. Quarterly Applied Math. 2, 164–168.

Liou, H.L., Brennan, N.A., 1996. The Prediction of Shperical Aberration with Schematic Eyes. Ophthalmic and Physiological Optics 16 (4), 348-354.

Liou, H.L., Brennan, N.A., 1997. Anatomically Accurate, Finite Model Eye for Optical Modeling. Journal of the Optical Society of America A 14 (8), 1684-1695.

Liu, Y.J., Wang, Z.Q., Song, L.P., Mu, G.G., 2005. An Anatomcally Accurate Eye Model with a Shell-structure Lens. Optik 116, 241-246.

Liu, Z., Wang, B., Xub, X., Wang, C., 2006. A study for accommodating the human crystalline lens by finite element simulation. Computerized Medical Imaging and Graphics, 30, 371–376.

Loos, J., Greiner, G., Seidel, H. P., 1998. A variational approach to progressive lens design. Computer Aided Design 30 (8), 595-602.

Magid, E., Soldea, O., Rivlin, E., 2007. A Comparison of Gaussian and Mean Curvature Estimation Methods on Triangular Meshes of Range Image Data. Computer Vision and Image Understanding 107, 139-159.

Manns, F., Fernandez, V., Zipper, S., Sandadi, S., Hamaoui., M., Ho., A., 2004. Radius of curvature and asphericity of the anterior and posterior surface of human cadaver lenses. Exp. Eye Res. 78, 39–51.

Manns, F., Fernandez, V., Zipper, S., Sandadi, S., Hamaoui., M., Ho., A., 2004. Radius of curvature and asphericity of the anterior and posterior surface of human cadaver lenses. Experimental Eye Research 78, 39-51.

Marquardt, D., 1963. An Algorithm for Least-Squares Estimation of Nonlinear Parameters. SIAM Journal Applied Math. 11, 431–441.

Martin, R. R., 1998. Estimation of Principal Curvatures from Range Data. International Journal of Shape Modeling 4, 521-543.

McIvor, A. M., Valkenburg, R. J., 1997. A comparison of Local Surface Geometry Estimation Methods. Machine Vision and Application 10, 17-26.

Meek, D. S., Walton, D. J., 2000. On Surface Normal and Gaussian Curvature Approximations

Given Data Sampled from a Smooth Surface. Computer Aided Geometric Design 17 (6), 521-543.

Meneghello, R., Concheri, G., Savio, G., 2005. Curvature error estimation in ground and polished surfaces of glass moulds. Congreso Internactional XVII INGEGRAF XV ADM ACTAS DEL CONGRESO, Sevila, 270-271

Meneghello, R., Concheri, G., Savio, G., Comelli, D., 2006. Surface and geometry error modeling in brittle mode grinding of ophthalmic lenses moulds. International Journal of Machine Tools and Manufacture 46 (12-13), 1662-1670.

Moré, J.J., 1977. The Levenberg-Marquardt Algorithm: Implementation and Theory. Lecture Notes in Mathematics 630, 105–116.

Mortenson, M. E., 2006. Geometric Modeling Third Edition. Industrial Press Inc. New York. Naik, S.M. , Jain, R.C., 1998. Spline-Based Surface Fitting on Range Images for CAD Applications. Conference on Computer Vision and Pattern Recognition 249-253.

Nakao, S., Ono, T., Nagata, R., Iwata, K., 1969. The distribution of refractive index in the human crystalline lens. Japan Journal of Clinical Ophthalmology 23, 903-906.

Navarro, R., Palos, F., González, L., 2007(a). Adaptive model of the gradient index of the human lens. I. Formulation and model of aging ex vivo lenses. J. Opt. Soc. Am. A. 24, 2175-2185.

Navarro, R., Palos, F., González, L., 2007(b). Adaptive model of the gradient index of the human lens. II. Optics of the accommodating aging lens. J. Opt. Soc. Am. A. 24, 2911-2920.

Navarro, R., Santamaría, J., Bescós, J., 1985. Accomodation-dependent Model of the Human Eye with Aspherics. Journal of the Optical Society of America A 2 (8), 1273-1281.

Norrby, S., 2005. The Dubbelman eye model analysed by ray tracing through aspheric surfaces. Ophthal. Physl Opt. 25, 153–161.

Norrby, S., 2005. The Dubbelman eye model analysed by ray tracing through aspheric surfaces. Ophthalmic and Physiological Optics 25, 153-161.

Page, D. L., Sun, Y., Paik, J., Abidi, M. A., 2002. Normal Vector Voting: Crease Detection and Curvature Estimation on Large, Noisy Meshes. Graphical Models 64, 199-229.

Pierscionek, B., Chan, D.Y.C., 1989. Refractive Index Gradient of Human Lenses. Optometry and Vision Science 66 (12), 822-829.

Pierscionek, B.K., 1996. Refractive index contours in the human lens. Experimental Eye Research 64, 887-893.

Pierscionek, B.K., Augusteyn, R.C., 1991. Shapes and dimensions of in vitro human lenses. Clinical and Experimental Optometry 74, 223-227.

Polthier, K., Schmies, M., 2006. Straightest Geodesics on Polyhedral Surfaces. International

Conference on Computer Graphics and Interactive Techniques, 30-38.

Pomerantzeff, O., Pankratov, M., Wang, G., Dufault, P., 1984. Wide-Angle Optical Model of the Eye, American Journal of Optometry & Physiological Optics 61 (3), 166-176.

Popiolek-Masajada, A., Kasprzak, H.T., 1999. A new schematic eye model incorporating accommodation. Optometry and Vision Science 76 (10), 720-727.

Popiolek-Masajada, A., Kasprzak, H.T., 2002. Model of the optical system of the human eye during accomodation. Ophthalmic and Physiological Optics 22, 201-208.

Razdan, A., Bae, M., 2005. Curvature Estimation Scheme for Triangle Meshes Using Biquadratic Bézier Patches. Computer Aided Design 37 (14), 1481-1491

Rosales, P., Dubbelman, M., Marcos, S., van der Heijde, R., 2006. Crystalline lens radii of curvature from Purkinje and Scheimpflug imaging. Journal of Vision 6, 1057-1067

Rosen, A.M., Denham, D.B., Fernandez, V., Borja, D., Ho, A., Manns, F., 2006. In vitro dimensions and curvatures of human lenses. Vision Research 46, 1002-1009.

Savio, G., 2008. Strumenti e metodi per lo sviluppo prodotto di lenti oftalmiche. Università degli Studi di Bologna - Dottorato di ricerca in Disegno e metodi dell'ingegneria industriale XX Ciclo

Schachar, R.A., Abolmaali, A., Le, T., 2006. Insights into the age-related decline in the amplitude of accommodation of the human lens using a non-linear finite-element model. Br J Ophthalmol 90, 1304–1309.

Schachar, R.A., 2004. Central surface curvatures of post–mortem extracted intact human crystalline lenses: Implications for understanding the mechanism of accommodation. Ophthalmology 111 (9), 1699–1704.

Schachar,R.A., Pierscionek, B., Abolmaali, A., Le, T., 2007. The relationship between accommodative amplitude and the ratio of central lens thickness to its equatorial diameter in vertebrate eyes. Br J Ophthalmol 91, 812–817.

Sharma, A., Vizia Kumar, D., Ghatak A.K., 1982. Tracing rays through graded-index media: a new method. Applied Optics 21 (6), 984-987.

Sheffer, A., de Sturler, E., 2001. Parameterization of Faceted Surfaces for Meshing using Angle-Based Flattening. Engineering with Computers 17, 326-337

Sheffer, A., de Sturler, E., 2002. Smoothing an Overlay Grid to Minimize Linear Distortion in Texture Mapping. ACM Transaction on Graphic 21 (4), 874-890.

Siedlecki, D., Kasprzak, H., Pierscionek, B.K., 2004. Schematic Eye With a Gradient-index Lens and Aspheric Surfaces. Optics Letters 29 (11) 1197-1199.

Smith, G., 2003. The optical properties of the crystalline lens and their significance. Clin. Exp.

Optom. 86 (1), 3–18.

Smith, G., Atchison, D.A., Iskander, D.R., Jones, C.E., Pope, J.M., 2009. Mathematical models for describing the shape of the in vitro unstretched human crystalline lens. Vision Res. 49, 2442–2452.

Smith, G., Pierscionek, B.K., Atchison, D.A., 1991. The optical modelling of the human lens. Ophthal. Physl Opt. 11, 359–370.

Stokely, E. M., Wu, S.Y., 1992. Surface Parameterization and Curvature Measurement of Arbitrary 3D-Objects: Five Practical Methods. IEEE Transaction on Pattern Analysis and Machine Intelligence 14 (8) 833-840.

Stoker, J.J., 1969. Differential Geometry. Wiley, New York. Struik, D., 1961. Lectures on Classical Differential Geometry. Addison-Wesley Series in Mathematics.

Surazhsky, T., Magid, E., Soldea, O., Elber, G., Rivlin, E., 2003. A comparison of Gaussian and Mean Curvatures Triangular Meshes. Robotics and Automation ICRA '03 International Conference 1, 1021-1026.

Tan, B., 2008. Optical Modeling of Schematic Eyes and Opthalmic Applications. Univeristy of Tennessee, Noxville.

Tang, C. K., Medioni, G., 2002. Curvature-Augmented Tensor Voting for Shape Inference from noisy 3D Data. IEEE Transactions on Pattern Analysis and Machine Intelligence 24 (6), 858-864.

Taubin, G., 1995. Estimation the Tensor of Curvature of a Surface from a Polyhedral Approximation. The Fifth International Conference on Computer Vision, 902-907.

Thibos, L.N., Ye, M., Zang, X., Bradley, A., 1997. Spherical Aberration of the Reduced Schematic Eye with Elliptical Refracting Surface. Optometry and Vision Science 74 (7), 548-556.

Tong, W. S., Tang, C. K., 2005. Robust Estimation of Adaptive Tensors of Curvature by Tensor Voting. IEEE Transactions on Pattern Analysis and Machine Intelligence 27 (3), 434-449.

Urs, R., Ho, A., Manns, F., Parel, J., 2010. Age–dependent Fourier model of the shape of the isolated ex vivo human crystalline lens. Vision Res. 50, 1041–1047.

Urs, R., Manns, F., Ho, A., Borja, D., Amelinckx, A., Smith, J., 2009. Shape of the isolated ex–vivo human crystalline lens. Vision Res. 49(1), 74–83.

Wang, J., Gulliver, R., Santosa, F., 2003. Analysis of a variational approach to the progressive lens designs. SIAM Journal on Applied Mathematics 64 (1), 277-296.

Wang, J., Santosa, F., 2004. A numerical method for progressive lens design. Mathematical Models and Methods in Applied Science 14 (4) 619-640.

Wang, Y., Thibos, L.N., 1997. Oblique (Off-axis) Astigmatism of the Reduced Schematic Eye with Elliptical Refracting Surface. Optometry and Vision Science 74 (7), 557-562.

Wang, Y., Wang, Z.Q., Guo, H.Q., Wang, Y., Zuo, T., 2007. Wavefront Aberrations in the Accomodated Human Eye Based on Individual Eye Model. Optik 118, 271-277.

Watanable,K., Belyaev, A. G., 2001. Detection of Salient Curvature Features on Polygonal Surfaces. Computer Graphics Forum 20 (3), 385-392.

Wei, X., Thibos, L., 2008. Modeling the eye's optical system by ocular wavefront tomography. Opt. Express. 16, 20490-20502.